

MHD SHOCK PRODUCTION AND CURRENT SHEET
DIFFUSION

Thesis by
Alan L. Hoffman

In Partial Fulfillment of the Requirements
For the Degree of
Doctor of Philosophy

California Institute of Technology
Pasadena, California

1967

(Submitted April 28, 1967)

ACKNOWLEDGMENTS

The author wishes to express his appreciation to Professor H. W. Liepmann, his advisor, who furnished continuing advice and encouragement throughout the period the research was carried out. In addition, the help of Professor G. B. Whitham in obtaining a physical insight into the problem is gratefully acknowledged. The assistance of his wife Bonnie in correcting the manuscript and Mrs. Geraldine Krentler, who typed the manuscript is deeply appreciated. Sincere thanks are also due to J. A. Smith for his constructive criticism of the original manuscript and his aid in bringing the manuscript to its final, more comprehensible form. The author is indebted to the National Science Foundation for its financial assistance, and also to the Office of Naval Research which supported the experiments.

ABSTRACT

Current sheets in inverse pinch MHD shock tubes exhibit the strange property of forming shocks in the very rear of the sheet when accelerating heavy gases. When accelerating light gases, shocks are formed further to the front in the sheet, but in no case do the shocks separate from the driving current sheet. This "piston dragging shock" effect is explained on the basis of a single-fluid model with variable conductivity. Shocks are shown to always form within current sheets which move at supersonic speeds with respect to the driven gas. The relevant parameters for determining the shock position are the Mach number and the magnetic Reynolds number. Large magnetic Reynolds numbers and small Mach numbers enhance forward shock formation. These conditions are obtained in light gases with high speeds of sound. Similarity methods are developed to estimate gas conductivities, electron temperatures, and degrees of ionization for the experiments which are conducted. In hydrogen typical electron temperatures of 4 eV are produced by the ohmic heating, but twice this value is shown necessary to achieve separation at the current sheet speeds of 2-3 cm/ μ sec used. Higher current sheet speeds produce shocks in the rear of the current sheet where separation can never occur. The correct method of procedure and the relevant design parameters to achieve

separation are given. The success of single-fluid methods in explaining plasma phenomena is especially notable, and these methods can be extended to other similar problems. Based on these methods, multiple-fluid and microscopic effects are easily detectable and can be accounted for.

TABLE OF CONTENTS

PART	TITLE	PAGE
	Acknowledgments	ii
	Abstract	iii
	Table of Contents	v
	List of Figures	vii
	List of Tables	x
I.	Introduction	1
II.	Qualitative Behavior of Diffusive Force Fields Used to Accelerate Gases	
	2.1 Equations of Motion With a Source Term	8
	2.2 $\gamma = 3$ Approximation	12
	2.3 Solution for a Concentrated Force	17
III.	Effects of Current Sheet Diffusion	
	3.1 Induction Equations With a Magnetic Field	21
	3.2 Similarity Solution for Finite Conductivity in Cylindrical Geometry	28
	3.3 Numerical Results	38
IV.	Experiments	
	4.1 Description of Apparatus	43
	4.2 Preionization Survey	46
	4.3 Axial Magnetic Fields	51
	4.4 Numerical Techniques - Estimation of Conductivity and Degree of Ionization	55
	4.5 Argon	64
	4.6 Helium	72

TABLE OF CONTENTS (cont.)

PART	TITLE	PAGE
	4.7 Hydrogen	78
V.	Interpretation and Atomic Quantities	
	5.1 Electron Collisions and Electron Temperature	85
	5.2 Ion and Neutral Collision Cross Sections	90
VI.	Summary and Conclusions	94
Appendices		
A.	Full Delta Function Force Solution	100
B.	Concentrated Force Program	104
C.	Cylindrical Similarity Solution Program	105
	References	110
	Tables	112
	Figures	117

LIST OF FIGURES

1. Characteristic diagrams for a fluid driven by a distributed force located in the shaded region. The resultant shocks are shown by a heavy line.
2. Disturbance profiles corresponding to the characteristic diagrams for large times. The steady flow regions are indicated.
3. Force diagram for the normalized shock velocity as a function of the normalized piston force for a piston which is moving at Mach 10 with respect to the gas upstream of the shock.
4. One dimensional simplified model of a current sheet with field and flow quantities indicated in both laboratory and current sheet coordinates.

$$E_y = E'_y + UB_z.$$
5. Current and density distributions in an inverse pinch as obtained from a conical solution, as a function of time $t^* = Ut/r = l/\eta$. Small Mach number.
6. Current and density distributions in an inverse pinch as obtained from a conical solution, as a function of time $t^* = Ut/r = l/\eta$. Large Mach number.
7. Inverse pinch geometry including circuit parameters.
8. Similarity solution showing the relationships between J , \dot{B}_θ , and B .
9. Shock and current sheet trajectories for preionized hydrogen.
10. Shock and current sheet trajectories for argon.
500 μ Hg 10 KV.
11. Shock and current sheet trajectories for preionized argon. 500 μ Hg 10 KV.
12. Shock and current sheet trajectories for argon.
125 μ Hg 10 KV.
13. Shock and current sheet trajectories for preionized argon. 125 μ Hg 10 KV.
14. Shock, current sheet, and \dot{B}_z profiles for argon.

LIST OF FIGURES (cont.)

15. Actual oscilloscope traces for argon at 175μ and $8\frac{1}{2}$ KV. Time scale $1 \mu\text{sec/div}$. Upper trace B_{θ} , 1 v/div . Lower trace pressure, $.5 \text{ v/div}$.
16. Shock and current sheet trajectories for argon. $100 \mu \text{ Hg}$ 7 KV.
17. Shock and current sheet trajectories for argon. $100 \mu \text{ Hg}$ $8\frac{1}{2}$ KV.
18. Shock and current sheet trajectories for argon. $100 \mu \text{ Hg}$ 10 KV.
19. Shock and current sheet trajectories for argon. $170 \mu \text{ Hg}$ 10 KV.
20. Shock and current sheet trajectories for argon. $170 \mu \text{ Hg}$ 12 KV.
21. Shock and current sheet trajectories for argon. $170 \mu \text{ Hg}$ 14 KV.
22. Shock and current sheet trajectories for argon. $400 \mu \text{ Hg}$ 14 KV.
23. Shock and current sheet trajectories for helium.
24. Current sheet trajectories for low density helium.
25. Actual oscilloscope traces for hydrogen at 700μ , and 6 KV. Time scale, $1 \mu\text{sec/div}$. Upper trace B_{θ} , 1 v/div . Lower trace pressure, $.2 \text{ v/div}$.
26. Shock and current sheet trajectories for hydrogen. $700 \mu \text{ Hg}$ 6 KV.
27. Shock and current sheet trajectories for hydrogen. $700 \mu \text{ Hg}$ $7\frac{1}{2}$ KV.
28. Shock and current sheet trajectories for hydrogen. $700 \mu \text{ Hg}$ 9 KV.
29. Shock and current sheet trajectories for hydrogen. $700 \mu \text{ Hg}$ $10\frac{1}{2}$ KV.
30. Shock and current sheet trajectories for hydrogen. $700 \mu \text{ Hg}$ 12 KV.

LIST OF FIGURES (cont.)

31. Shock and current sheet trajectories for hydrogen.
290 μ Hg 9 KV.
32. Current sheet trajectories for low density hydrogen.
33. Shock and current sheet trajectories in hydrogen with the main capacitor bank charged to $7\frac{1}{2}$ KV and fired 1.4 μ sec after the preionization bank which is charged to 6 KV.
34. Electron neutral collision cross sections as a function of electron energy.

LIST OF TABLES

- Table 1. Summary of eleven computer runs for the conical solution to an inverse pinch under various operating conditions. Notation is shown in figure 5.
- Table 2. Argon Experimental Data
- Table 3. Hydrogen Experimental Data
- Table 4. Equilibrium Conditions Behind a Shock in Hydrogen
- Table 5. Ion and Neutral Collision Cross Sections

I. INTRODUCTION

In recent years the use of body forces to produce and control the motion of fluids has received great attention. The most useful body force is of course the $\underline{J \times B}$ force produced by discharging a current through a conducting fluid in the presence of a perpendicular magnetic field. For fluids such as liquid metals the problems are well formulated, though by no means easily solved, to the extent that classical fluid mechanics techniques may be employed. The additional complications caused by the body force and the equations governing its behavior form the field of Magnetohydrodynamics, which, as the name implies, is standard hydrodynamics in the presence of magnetic fields' which influence the fluid flow.

The high temperatures necessary to produce conductivity in compressible fluids, such as gases, unfortunately produce additional effects, and the formulation of a particular problem now becomes as difficult, and certainly as important, as the actual solution of the problem. The gas, which is now properly called a plasma, consists not of one fluid, but of at least three; electrons, ions, and neutrals, and the propriety of even calling each individual component a fluid is in doubt. The treatment of a plasma on a microscopic scale is exceedingly difficult; it is at least an order of magnitude more so than the corresponding

kinetic theory approach to rarefied, low temperature gas flows. The importance of correctly formulating the problem becomes evident when one considers the significant simplifications that can be achieved if the plasma can in any way be considered a fluid, even a multi-component one, and the powerful techniques of fluid mechanics be brought to bear. It is the purpose of this paper to investigate a field of research that has suffered from both a lack of formulation as a problem treatable by macroscopic fluid equations, and a lack of understanding of the correct macroscopic behavior. The demonstration of the ability to extend fluid mechanics to new regions of interest, and to explain new phenomena, is perhaps more important than the actual elucidation of this particular problem.

The problem to be investigated is that of accelerating plasmas through the use of large arc discharges which are acted upon by their own magnetic fields. The geometries are many, and vary according to the purposes of the acceleration, which are threefold; propulsion, fusion, and shock production. The first two do not depend explicitly on the plasma being a fluid. The third, however, is dependent on the appropriateness of a fluid description since a conventional shock wave is of necessity a fluid phenomenon involving the hyperbolic nature of the macroscopic fluid equations of motion. MHD shock tubes, as these shock producing accelerators are called, depend for their success

on the effectiveness of the arc discharge, or current sheet, on acting as a solid piston and sweeping up all the gas in its path, as does a conventional shock tube piston. If the current sheet does act as an impermeable piston, then it would be expected, by analogy to the standard shock tube, that a shock would be driven out in front of it, and the normal shock tube relations would apply. However, it has been found that in all cases where a shock does form, it does so within the current sheet and never separates from it. This is so even though, based on the macroscopic equations of motion, the current sheet should be thin compared to the distance a shock would be expected to separate from a conventional solid piston. Because of this, and in spite of the fact that a shock did form, experimenters were quick to claim that the fluid equations did not apply, and the microscopic behavior must be held accountable. This microscopic behavior, involving particle orbits and endothermic collisions, is important and will be considered in a later chapter, but it can only be investigated sensibly once the gross behavior of the various devices has been established. This is also true for the propulsion applications, and to some extent may even apply to the fusion devices. For the MHD shock tubes, the microscopic behavior will be considered as a perturbation, albeit an important one, on the correct macroscopic behavior, which will thus be discussed first.

MHD accelerators must be distinguished from the older arc heating devices, such as the "T" tube, which employ an ohmic heating energy source and are sometimes aided by a \underline{JxB} driving force provided by a backstrap. The newer parallel plate, coaxial (MAST), and inverse pinch shock tubes make use of a \underline{JxB} source term as the primary driving mechanism. In fact, in these newer devices the ohmic heating, which acts directly on the electrons, has so little effect on the acceleration or heating of the heavy particles, that it can be neglected. This is due to the large mass difference between the electrons and the ions or neutrals which precludes energy transfer to the heavier particles in the typically short operating times in these devices. Since the electrons carry the current, the force acts directly on them, but the short Debye length effectively couples them to the ions in transferring momentum. The ions, in turn, are coupled to any neutrals present through either a large elastic or charge exchange cross section. These assumptions will be used as a first approximation to justify the use of a macroscopic treatment of the plasma flow and shock formation phenomenon, but later, deviations from these conditions will be considered.

Previous fluid models for MHD shock tubes have been of two types; the detailed shock solution, and the simplified combined shock and piston solution. The first type treats

only the shock itself, assuming either a single-fluid model with given finite conductivities such as Marshall's (Ref. 1) or more complicated multi-fluid behavior with chemical reactions typified by Gross' work (Ref. 2). The second type is the snowplow, or infinite conductivity similarity solution of Greifinger and Cole (Ref. 3) which treats the problem as a whole. However, this method still does nothing to elucidate the interaction between the driving force and the resultant shock, since the driving force field is assumed to be infinitely thin. Since this force field shock interaction is the primary characteristic of all MHD shock tubes, it must be accounted for in any macroscopic first approximation of the flow problem. The pattern to be followed in this paper will be a series of refinements on the simplest model one can construct which still exhibits the gross behavior observed in experiments. The more advanced refinements will depend on the experimental results themselves for evaluating the microscopic influences which are too complicated to estimate by theoretical methods alone. The validity of the original assumptions can then be evaluated to determine the consistency of the method.

In order to investigate the details of the shock formation problem, a simple, one dimensional, stable, and repeatable experiment is desired. The inverse pinch geometry, first conceived by Liepmann and Vlases (Ref. 4), satisfies all these requirements and offers great advantages

over the pinch, parallel plate, and coaxial geometries for this particular problem. It has the further advantage of yielding a similarity solution with a constant speed shock and piston for a linearly rising discharge current, which can easily be produced experimentally. The so-called snow-plow speed derived from a simple momentum balance, assuming all the gas to be swept into a thin sheet, will be the characteristic velocity of the problem. Initial experiments in the inverse pinch yielded the somewhat startling result that a shock was always located within the current sheet, and for heavy gases was in fact located in the very rear-most portion of the sheet. This would correspond to a piston dragging a shock behind it, and for this reason simple fluid mechanical arguments were considered inadequate to explain the action of the device. Exotic models such as a current carrying electron sheet dragging an ion sheet were proposed, but were quickly ruled out from energy considerations. More plausible arguments considering ion slip (Ref. 6) were proposed to deal with the growth of the current sheet, but they could in no way account for the observed shock formation phenomena.

Current sheet growth will be considered here from gross conductivity arguments, and the relevant atomic cross sections for both conductivity and ion slip will be discussed in the section dealing with atomic parameters. The most significant observation as to the position of the

shock within the current sheet will be treated purely from fluid mechanical arguments, which will be shown adequate to explain the observed phenomena. These arguments will also both qualitatively and quantitatively account for the strange dependence of the shock position on the atomic mass of the driven gas (Refs. 6, 12).

II. QUALITATIVE BEHAVIOR OF DIFFUSIVE FORCE FIELDS USED TO ACCELERATE GASES

2.1 Equations of Motion With a Source Term

The simplest model for gas acceleration by \underline{JxB} body forces must at least account for two things; the distributed nature of the force field and its permeability. To obtain an intuitive feeling for the possible phenomena, an ideal, inviscid, and non-heat conducting fluid will be considered subject to a momentum source term in its equations of motion. All shock producing devices require some such source term to produce gradients in the flow variables, which will steepen into a narrow region of high gradients due to the hyperbolic nature of the equations. The classical shock tube piston can be thought of as either a step function source of mass or a delta function of applied force. Exploding wires, lasers, and MHD accelerators make use of mass, energy, and momentum respectively as the primary source terms to produce shock waves. The momentum source term considered in this simple case will be one dimensional, and of constant but arbitrary shape. References will be made to the \underline{JxB} body force in a conducting plasma, but the following discussion applies equally well to any possible body force in an ideal fluid. Section III will take into account the behavior of the specific \underline{JxB} force of final interest. It is the use of the momentum source term alone that retains the most essential

nature of the problem, and which will allow analytic solutions to be derived to help visualize the shock tube behavior.

For the case of a force field traveling through the fluid at some constant speed U , the mass and momentum equations are simple to write. However, care must be taken in writing the energy equation to make it consistent with the assumption of ohmic heating having no effect on the heavy particles (or gross fluid). Ignoring viscosity and thermal conductivity, the equations of motion can be written as follows:

$$\frac{\partial \rho}{\partial t} + u \frac{\partial \rho}{\partial x} + \rho \frac{\partial u}{\partial x} = 0$$

$$\rho \frac{\partial u}{\partial t} + \rho u \frac{\partial u}{\partial x} + \frac{\partial p}{\partial x} = f(x - Ut)$$

$$\rho \frac{\partial}{\partial t} (e + \frac{1}{2}u^2) + \rho u \frac{\partial}{\partial x} (e + \frac{1}{2}u^2) + \frac{\partial}{\partial x} (pu) = uf(x - Ut) + q$$

with standard notation. The total rate of work done by the external force field is $Uf(x - Ut)$, of which $uf(x - Ut)$ goes directly into accelerating the fluid. The remainder, $(U - u)f(x - Ut)$ is an effective friction due to the force field moving faster than the fluid. This may, or may not be accounted for in the heat input term q , depending on whether the heat of friction is or is not transferred to the fluid. For the case of a JxB force caused by a moving current sheet, the friction term is due to the finite conductivity

which allows the current to diffuse through the gas. It is shown in section III that this friction is just the ohmic dissipation and should be ignored in the flow equations for the heavy particles. In that case the electrons act as a separate heat absorbing medium. In this general discussion the heat of friction is also assumed not to go into the fluid under consideration and q is set equal to zero. Thus, the energy equation reduces to the simple form:

$$\frac{\partial s}{\partial t} + u \frac{\partial s}{\partial x} = 0$$

where s is the entropy. As long as no shock is formed the entropy remains constant.

Using the fact that the entropy is constant to relate the density ρ to the sound speed a , and transferring to a moving frame $X = x - Ut$, $u' = U - u$, the mass and momentum equations become:

$$\left(\frac{2}{\gamma-1}\right) \left\{ \frac{\partial a}{\partial t} - u' \frac{\partial a}{\partial X} \right\} - a \frac{\partial u'}{\partial X} = 0$$

$$\frac{\partial u'}{\partial t} - u' \frac{\partial u'}{\partial X} - \left(\frac{2}{\gamma-1}\right) a \frac{\partial a}{\partial X} = - \frac{f(X)}{\rho} = - h(X)$$

with the arbitrary force applied so that it is proportional to ρ . Written in characteristic form with $\phi = -u' + a$, $\psi = -u' - a$, the equations are as follows:

$$\left(\frac{\partial}{\partial t} + \phi \frac{\partial}{\partial X}\right) \{ (\gamma+1) \phi + (3-\gamma) \psi \} = 2(\gamma-1)h(X) \quad (1)$$

$$\left(\frac{\partial}{\partial t} + \psi \frac{\partial}{\partial X}\right) \{(\gamma-3)\varphi + (\gamma+1)\psi\} = 2(\gamma-1)h(X) \quad . \quad (2)$$

The initial value problem is the important case to consider where $\varphi = \varphi_0$, $\psi = \psi_0$ at $t = 0$ for all X . However, it is useful to look first for steady solutions since the initial value problem will contain regions of steady flow. Steady solutions can only be written implicitly, and are most easily expressed in the physical variables u' and a . Calling $n = 2/(\gamma - 1)$, the steady solutions are:

$$u' a^n = u'_{\infty} a'_{\infty}^n \quad (3)$$

$$\frac{1}{2}(u'^2 + na^2) = \frac{1}{2}(u'_{\infty}{}^2 + na_{\infty}{}^2) - \int_X^{\infty} h(z) dz \quad . \quad (4)$$

These two equations, plus the standard shock jump conditions give a full description of the flow in regions where transients from the initial starting process are not important. To treat the transients, which include the phenomenon of shock formation, the full time dependent equations (1) and (2) must be used with a numerical scheme employed to integrate along both sets of characteristics φ and ψ . However, this scheme can be greatly simplified by choosing a fictitious gas with a specific heat ratio $\gamma = 3$. While no gas of interest is of this type, the value of γ does not alter the general behavior, which is all that is of interest in this first approximation.

2.2 $\gamma = 3$ Approximation

For a gas with $\gamma = 3$ the characteristic equations uncouple and only (1) is necessary to describe the flow in terms of φ , although (2) is of course necessary to obtain the physical quantities u' and a . Equation (1) can now be written:

$$\frac{\partial \varphi}{\partial t} + \varphi \frac{\partial \varphi}{\partial X} = h(X) \quad (5)$$

and the corresponding steady solution is seen to have two branches:

$$\varphi = \pm \sqrt{\varphi_{\infty}^2 - 2 \int_X^{\infty} h(z) dz} \quad \text{for } \varphi_{\infty} \begin{matrix} > 0 \\ < 0 \end{matrix} \quad (6)$$

where φ_{∞} is the value of φ at $X = \infty$. It is immediately obvious that there is a critical total force $H = \int_{-\infty}^{\infty} h(X) dX$ and that the equation will have different solutions depending on whether H is greater or less than $\frac{1}{2}\varphi_{\infty}^2$. In the X, t coordinates the fluid velocity is u' , ($\varphi = a - u'$), so that the flow is supersonic for $\varphi < 0$ and subsonic for $\varphi > 0$. For supersonic flow and H less than $\frac{1}{2}\varphi_{\infty}^2$ equation (6) must apply, since the effects of the transients are swept downstream. For subsonic flow or H large this is no longer the case and the effects of transients must be considered.

There are thus three cases of interest for the initial value problem with $\varphi_0 = a_0 - U$: 1) $\varphi_0 > 0$; 2) $\varphi_0 < 0$, $H > \frac{1}{2}\varphi_0^2$; 3) $\varphi_0 < 0$, $H < \frac{1}{2}\varphi_0^2$. The characteristic equation

(5) can be written as:

$$\frac{d\varphi}{d\tau} = h(X) \quad \text{along} \quad \frac{dX}{dt} = \varphi \quad (7)$$

and the characteristic diagrams for these cases are drawn in figure 1 for a finite force region (shown shaded). The shapes of the resultant disturbances are shown in figure 2 for some reasonably large time. The subsonic case ($\varphi_0 > 0$) is the one which would be intuitively expected with the force field causing a disturbance in front of it which immediately steepens into a shock. However, when the force field is moving at a supersonic speed ($\varphi_0 < 0$), the shock, if one occurs at all, is formed within the force field and its position depends on both the size of the force field and the initial slope of the characteristics (value of φ_0). In fact, for the weak field of case 3, it is seen that the solution consists only of an expansion and compression region, without a shock ever being formed. It is a notable result that the compression region doesn't steepen, as it would be expected to when dissipative mechanisms are not included. The steady solutions are applicable in these regions, which always include the region of applied force. Shock speeds can be simply derived from the physical equations written in conservation form outside the applied force region and the problem is thus essentially solved for any given $h(X)$.

Although the characteristic diagrams were drawn for $\gamma = 3$, this special choice in no way alters the behavior of the solutions. The decoupling of the characteristic equations does not influence the function of the characteristics in carrying information, but it does allow one set to be drawn independent of the other. This should not be confused with a simple wave solution where only one set of characteristics carries information. The approximation $\gamma = 3$ can even be justified in certain cases for real gases where one set of characteristics is less influenced by the applied forces than the other (Ref. 5).

One important result to notice which is independent of γ is the position of the expansion wave for case 2. The rearmost characteristic remaining in the region of applied force must be vertical, as long as it is out of the influence of the expansion in the ψ characteristics. This condition will be discussed fully in the following subsection. When it is satisfied, the characteristic direction φ , which doesn't contain γ , must be zero at the rear of the force field. This corresponds to the Chapman-Jouget condition of the flow being just sonic behind an explosively produced shock wave, and is necessary to solve for the complete flow field in the limiting condition of a concentrated force.

The large force supersonic case (case 2) is the one of primary interest for most true MHD accelerators, although case 3 may have some application to MAST type devices where

it is doubtful if a true shock is ever formed. In the inverse pinch experiments described in section 4, the shock position was accurately defined by the use of a piezo-electric pressure probe. (A shock always formed when the neutral-neutral mean free path was small compared to the current sheet dimensions.) From the simple model presented here, the important parameters governing the shock formation position can be ascertained. Normalizing the force, and the velocities,

$$\bar{h} = \frac{h}{U^2}, \quad \bar{\varphi} = \frac{\varphi}{U}, \quad \varphi_0 = -\left(1 - \frac{a_0}{U}\right).$$

The condition that $\bar{\varphi} = 0$ at X_s , the shock formation position, can be written:

$$\int_{X_s}^{\infty} \bar{h}(x) dx = \frac{1}{2} \bar{\varphi}_0^2 = \frac{1}{2} \left(1 - \frac{1}{M_F}\right)^2 \quad (8)$$

where $M_F = U/a_0$ is the force field Mach number. As M_F increases, X_s decreases, and the shock will form further to the rear in the current sheet. This explains the strange behavior described in the introduction where heavy gases yield shocks in the rear of the driving piston (current sheet). The phenomenon is due solely to the large Mach numbers produced when driving heavy gases at high speeds. The problem can be related to that of supersonic choking where it will take longer to choke highly supersonic flows

down to sonic velocities. This can also be seen from case 2 of figure 1 where the initially more horizontal characteristics ($\bar{\varphi}_0 \rightarrow 1, M_F \rightarrow \infty$) take longer to be turned around. A second important parameter is obviously the value of H and also the distribution and width of the force field $h(X)$. In the more detailed numerical solutions, the piston will be assumed impermeable and H will be well defined, but the width will be arbitrary and will be characterized by the magnetic Reynolds number which governs the diffusion of the current sheet. The actual dependence on the Mach number will also become more pronounced. Before going into this next level of approximation, one more important solution, that for a concentrated force, can be worked out from the simple force field model which is done in the following subsection.

2.3 Solution for a Concentrated Force

In the limit of delta function applied forces, the previous problem can be extended to gases with arbitrary γ and the restriction of a mass dependent body force can be lifted. Of course, no information can be obtained as to shock formation position within the force field. The upper limit on the applied force is just the piston pressure in an ordinary shock tube in which all the driven gas is accelerated to the piston or force field velocity. Forces less than this value must correspond to leakage through the force field. A good analogy for this case is that of moving a screen through a gas. Again, the difference in screen and gas velocities constitutes an effective friction, but to be consistent, this heat addition must be ignored since only the electrons are affected. In fact, solving the problem with and without heat addition leads to approximately the same results, except that the gas in the expansion wave behind the piston is hotter when the friction term is included. Physically, these leaky piston solutions correspond to cases where all the gas has not been fully swept up, and there is evidence of this expansion wave in the inverse pinch experiments.

The previous discussions have not explained the fact that the shock, once formed, is not observed to separate from the current sheet. For the conventional shock tube with a solid piston the shock separation is obviously due

to the mass accumulation behind the shock, but in front of the piston. Two criteria can influence the tendency of a shock to separate from a diffuse, non-solid piston. They are mass accumulation ahead of the shock, and leakage through the piston, both effects being impossible for a solid piston. The first of these will be investigated in conjunction with the discussion on current sheet spreading in section III but the second effect can be dealt with in the present discussion. The rate of separation depends on the amount of leakage, and hence on the size of the total force. Only the physically important supersonic case (case 2) with shock formation will be considered and it is therefore of interest to determine the minimum total force necessary to form a shock (related to the old condition $H > \frac{1}{2}\varphi_0^2$).

When the minimum force F (where $f(x - Ut) = F\delta(x - Ut)$) is exceeded, the solution will consist of an ordinary shock moving faster than the force field, a uniform region between the two, and an expansion region behind the force field. The jump conditions across the force are derived from the mass, momentum, and energy equations written in conservation form. Calling $\bar{u} = u/U$, $\bar{\rho} = \rho/\rho_0$, $\bar{p} = p/\rho_0 U^2$, $\bar{F} = F/\rho_0 U^2$, the jump conditions are written:

$$[\bar{\rho}] - [\bar{\rho} \bar{u}] = 0$$

$$[\bar{\rho}u] - [\bar{\rho} \bar{u}^2 + \bar{p}] = \bar{F}$$

$$[\bar{\rho}s] - [\bar{\rho} \bar{u}s] = 0 \quad .$$

In force fixed coordinates, $\bar{u}' = 1 - \bar{u}$, the equations become:

$$[\bar{\rho} \bar{u}'] = 0$$

$$[\bar{\rho} \bar{u}' + \bar{p}] = \bar{F}$$

$$[s] = 0 \quad \text{or} \quad \left[\frac{\bar{p}}{\bar{\rho}^\gamma} \right] = 0 \quad .$$

In finding the solution, a shock velocity V is chosen such that $U \leq V \leq \left\{ \frac{\gamma+1}{4} + \sqrt{\left(\frac{\gamma+1}{4}\right)^2 + \frac{1}{2}} \right\} U$, and the value of \bar{F} needed to produce it is determined. The maximum value of V corresponds to a solid piston with no leakage and the corresponding maximum force F will be just the non-dimensional piston pressure for an ideal shock tube. For a given force field Mach number and a given shock velocity the conditions behind the shock are known. However, there are only three jump conditions to solve for $\bar{\rho}$, \bar{u}' , and \bar{p} behind the force field, plus the force \bar{F} . One additional condition is required, which in an ordinary shock tube is provided by matching to the downstream expansion wave in the driver gas. Here, the correct condition, for the case when the force field is moving faster than the escape speed of $\frac{2}{\gamma-1} a_0$, is that $\phi = u + a - U = 0$ behind the force field. This "escape speed" criterion is derived in appendix A where

the full solution behind the force field is found. For the previous $\gamma = 3$ approximation, the escape speed is just a_0 , and all supersonic force fields move faster than this speed, so its effect is never noticed as a lower limit on the simple solution.

The condition behind the force can be written:

$$\bar{\phi}_{\text{rear}} = \bar{u} + \bar{a} - 1 = 0 .$$

Since $\bar{a} = a/U$ can be related to the other variables, the problem is completely determined. A simple program, shown in appendix B, gives a plot of \bar{F} as a function of the shock speed $\bar{V} = V/U$ for a given γ and $M_F = U/a_0$. M_F is denoted by RMO in the program and KK is a control. The results are shown in figure 3 for $M_F = 10$. Making M_F larger alters the results only slightly. Also included is the case where energy instead of entropy is conserved across the force to illustrate the lack of influence on the gross behavior. It is obvious from the solution shown in figure 3 that unless the force is quite small, leakage alone cannot account for the fact that the shock does not separate from the current sheet.

III. CURRENT SHEET DIFFUSION

3.1 Induction Equation With a Magnetic Field

The previous section has proceeded as far as possible based on a model with an arbitrary and non-spreading force field. Even with this model, a more detailed knowledge of the force field is required to determine the shock formation position as defined by equation (8). Also, to account for the lack of separation, some knowledge of the force field growth is required since it has been shown that leakage, alone, cannot account for this failure to separate. Using the single-fluid model, a form of the induction equation must be included if one wishes to investigate the spreading of the current sheet in MHD shock tubes. However, due to the large magnetic fields which are present, the electron cyclotron frequency will be larger than the electron collision frequency, and it is not immediately obvious what effect the conductivity of the gas will have on the current diffusion. For this reason a brief derivation of the induction equation will be presented at this time, along with a derivation of the relationship between ohmic heating and force field friction.

Figure 4 is a one dimensional model of the current sheet with the quantities of interest defined. Considering the current sheet from the steady coordinates, the inertia terms in the electron momentum equation are negligible and

the field forces must just balance the collision losses.

Therefore,

$$n_e e [\underline{E}' - \underline{u}' \times \underline{B}] - [\underline{J} \times \underline{B} - \nabla p_e] = \underline{P}_{ei} + \underline{P}_{en} \quad (9)$$

where n_e is the electron number density, p_e is the electron pressure, and \underline{P}_{ei} and \underline{P}_{en} are the momentum loss terms for collisions with ions and neutrals. When the ion and neutral velocities are small compared to the electron velocity, \underline{v}_e , in the current carrying direction, the collision terms can be written:

$$\underline{P}_{ei} = -n_e \nu_{ei} m_e \underline{v}_e$$

$$\underline{P}_{en} = -n_e \nu_{en} m_e \underline{v}_e$$

ν_{ei} and ν_{en} are the respective collision frequencies for the electron collisions with ions and neutrals. Calling $\nu_T = \nu_{ei} + \nu_{en}$ and defining an electrical resistivity,

$$\eta_T = \frac{m_e \nu_T}{n_e e^2} \quad (10)$$

and calling the current $\underline{J} = -n_e e \underline{v}_e$, equation (9) can be written:

$$\eta_T \underline{J} = [\underline{E}' - \underline{u}' \times \underline{B}] - \frac{1}{n_e e} [\underline{J} \times \underline{B} - \nabla p_e] \quad (11)$$

Calling $\underline{B} = B \hat{k}$, where \hat{k} is a unit vector in the z direction, and defining a cyclotron frequency $\omega_c = \frac{eB}{m_e}$, equation (11)

takes the form:

$$\underline{J} + \frac{\omega}{v_T} \underline{J} \times \hat{k} = \frac{1}{\eta_T} \underline{E}'_T \equiv \frac{1}{\eta_T} [\underline{E}' - \underline{u}' \times \underline{B} + \frac{1}{n_e e} \nabla p_e]. \quad (12)$$

This somewhat arbitrary notation can be used to define a tensor conductivity so that:

$$\underline{J} = \underline{\underline{\sigma}} \cdot \underline{E}'_T \quad . \quad (13)$$

Calling $\Omega = \frac{\omega}{v_T}$, $\underline{\underline{\sigma}}$ takes the form:

$$\underline{\underline{\sigma}} = \frac{1}{\eta_T(1+\Omega^2)} \left\{ \begin{array}{ccc} 1 & -\Omega & 0 \\ \Omega & 1 & 0 \\ 0 & 0 & 1 + \Omega^2 \end{array} \right\} . \quad (14)$$

This description is useful when computing field quantities but is extremely confusing when discussing dissipative mechanisms such as ohmic heating and diffusion since the increased resistivity $\eta_T \Omega^2$ due to the cyclotron frequency is not dissipative. In deriving the induction equation, equation (11) will be used rather than equations (13) and (14).

In laboratory coordinates \underline{B} remains unchanged and $\underline{E} = \underline{E}' - \underline{u} \times \underline{B}$. Assuming that there is no charge separation so that \underline{J} remains in the y direction, equation (11) becomes

$$\eta_T \underline{J} = \underline{E} + \underline{u} \times \underline{B} - \frac{1}{n_e e} [\underline{J} \times \underline{B} - \nabla p_e] \quad . \quad (15)$$

Using Maxwell's equations,

$$\nabla \times \underline{E} = - \frac{\partial \underline{B}}{\partial t} \quad \text{and} \quad \nabla \times \underline{B} = \mu_0 \underline{J} \quad ,$$

ignoring smaller terms, and taking the curl of equation (15),

$$\frac{\partial \underline{B}}{\partial t} - \nabla \times (\underline{u} \times \underline{B}) = \nabla \times \left\{ \frac{\eta_T}{\mu_0} \nabla \times \underline{B} \right\} + \nabla \times \left\{ \frac{1}{n_e e} (\underline{J} \times \underline{B} - \nabla p_e) \right\} \quad . \quad (16)$$

For the one dimensional problem with the directions defined in figure 4, and variation only in the x direction equation (16) takes the scalar form:

$$\frac{\partial B}{\partial t} + \frac{\partial}{\partial x} (uB) = \frac{\partial}{\partial x} \left(\frac{\eta_T}{\mu_0} \frac{\partial B}{\partial x} \right) \quad . \quad (17)$$

It is important to notice that for the case when $J_x = 0$ the last term in equation (16), which greatly affects the conductivity as defined by equation (13), has no effect on the diffusion of the current sheet. In fact Schluter shows in general (Ref. 21) that this is true for a fully ionized gas where $\underline{J} \times \underline{B}$ can be written as the gradient of the total pressure. This can also be extended to partially ionized gases where the heavy particles are accelerated by gradients in pressure and electric potential which are balanced by the $\underline{J} \times \underline{B}$ forces (irrotational flow).

It was mentioned previously that the heat input term q in the equations of motion for a current sheet force field is exactly the ohmic dissipation. This is easily seen for

the current sheet in figure 4. The total energy added to the steady flow is just $\underline{J} \cdot \underline{E}'$. Using equation (11):

$$\begin{aligned} \underline{J} \cdot \underline{E}' &= \underline{J} \cdot \left\{ \eta_T \underline{J} + \underline{u}' \times \underline{B} + \frac{1}{n_e e} [\underline{J} \times \underline{B} - \nabla p_e] \right\} \\ &= \eta_T J^2 - u' JB \end{aligned}$$

since $\underline{J} \times \underline{B}$ and ∇p_e are perpendicular to \underline{J} . Thus again, the non-dissipative part of the resistivity has no effect. For a conducting fluid $\underline{E}' \approx 0$ and the ohmic heating $\eta_T J^2$ is approximately equal to the friction term $u' JB$. For an infinitely conducting fluid, $\eta_T = 0$, there can be no relative velocity u' between the fluid and field. For the unsteady case:

$$\underline{J} \cdot \underline{E} = \eta_T J^2 + uJB \approx UJB \quad . \quad (18)$$

$\eta_T J^2$ is exactly the friction heat input term q which was ignored in section II.

Some use can be made of the tensor equation (13).

Since $J_x = 0$:

$$0 = \frac{1}{\eta_T} \frac{1}{1+\Omega^2} [E_{Tx} - \Omega E'_{Ty}]$$

$$J_y = \frac{1}{\eta_T (1+\Omega^2)} [\Omega E_{Tx} + E'_{Ty}] \quad .$$

Thus:

$$E_{Tx} = \Omega E'_{Ty}$$

$$J_y = \frac{1}{\eta_T \Omega} E_{Tx} = en_e \frac{E_{Tx}}{B} = \frac{1}{\eta_T} E'_{Ty} \quad (20)$$

It is seen that the Hall parameter Ω creates a strong electric field E_x and that the electron current is due to ExB drift. Equation (20) can be used to calculate the electron number density n_e . Sorrell (Ref. 6) essentially makes use of this equation to calculate the degree of ionization, although his reasoning is more physical. If the electrons carry the current J_y , then a force $J_y B$ will be exerted on them. This force will be transferred to the ions through the electric field E_x . Therefore $\int J_y B dx = \int n_i e E_x dx$ across the current sheet where n_i is the ion concentration and equal to n_e . Since the ions must eventually accelerate all the gas by collisions, the above equation can be written in terms of the voltage V_x across the sheet,

$$\tilde{F}n = n_i e V_x,$$

or calling $\alpha = n_i/n$ for constant α ,

$$\alpha = \frac{\tilde{F}}{eV_x} \quad (21)$$

where \tilde{F} is the total energy per particle which is known

from gross momentum balance for any experiment. Sorrell uses equation (21) to great advantage to calculate average degrees of ionization and confirms these measurements with Stark broadening data where possible. His results will be used in section IV to confirm some of the methods developed there to estimate electron temperatures and degrees of ionization.

3.2 Similarity Solution for Finite Conductivity in Cylindrical Geometry

The induction equation (17) along with the fluid equations of motion previously used in section II form the second level of approximation to be investigated. The most critical additional parameter introduced is the electrical conductivity $\sigma = \frac{1}{\eta_T}$ which governs the thickness of the current sheet. The two other plasma transport parameters, the viscosity and the thermal conductivity, are ignored, so that the mathematical model describes a force field of finite dimension, but an infinitely thin shock discontinuity. In effect, this allows the flow variables ρ , u , and p to have discontinuities, but requires the magnetic field B to be continuous. The shock will be ordinary in the gas dynamic sense, and not a so-called MHD shock. The flow equations thus exhibit local hyperbolic properties, but become basically parabolic due to the diffusion equation for B . For this reason unusual properties must be expected, such as the compression upstream of the shock mentioned in section II.

The level of sophistication of this model depends essentially on the method of describing the conductivity σ . The most usual method is to set σ equal to some function of the temperature. However, in these short duration devices the electron temperature, which is the factor that determines the electrical conductivity, bears no relationship to the

heavy particle gas temperature given by the flow equations. There is not enough time for the electrons to equilibrate with the heavy species. The electron temperature is then only a function of the ohmic heating, the ionization losses, radiation, and many other effects that are too complicated to treat theoretically. The method to be followed here is to assume conductivity distributions and then use the experimental results to estimate the accuracy of the assumptions. It is found that the general behavior of MHD shock producing devices is not too dependent on the exact conductivity distribution chosen, but rather on the average of the distribution. In some cases, where the shock itself influences the conductivity, the deviation from the theoretical model is obvious and the effect of the shock on the conductivity can be determined. Thus, this simple model even serves as a powerful tool in investigating effects that would seem to limit its validity. Its main significance is that it gives one a standard with which to compare experimental results, that has so far been lacking in problems such as these. The importance of this cannot be over-emphasized, the model is not meant to be an exact solution of the true physical case, but rather it is meant to establish a viewpoint from which to interpret the experiments. It is a good approximation for many flows, and is also extremely useful, perhaps even more so, for flows where at some point the basic assumptions break down.

In order to compare the theoretical results with the geometry of the inverse pinch (Fig. 7), the equations of motion are written below in cylindrical coordinates. The mass, momentum, induction, and entropy equations are:

$$\begin{aligned} \frac{\partial \rho}{\partial t} + \frac{1}{r} \frac{\partial}{\partial r} (r \rho u) &= 0 \\ \frac{\partial u}{\partial t} + u \frac{\partial u}{\partial r} + \frac{B}{\rho \mu_0 r} \frac{\partial}{\partial r} (r B) + \frac{1}{\rho} \frac{\partial p}{\partial r} &= 0 \\ \frac{\partial B}{\partial t} + \frac{\partial}{\partial r} (u B) - \frac{\partial}{\partial r} \left\{ \frac{1}{\mu_0 \sigma} \frac{1}{r} \frac{\partial}{\partial r} (r B) \right\} &= 0, \\ \frac{\partial}{\partial t} \left(\frac{p}{\rho \gamma} \right) + u \frac{\partial}{\partial r} \left(\frac{p}{\rho \gamma} \right) &= 0 \end{aligned} \tag{22}$$

where B is the value of the magnetic field in the θ direction. Except for the cylindrical geometry and the coupled diffusion equation for the momentum source term, the equations are identical to the ones used in the general analysis of section I. Even for a specified σ , equations (22) are extremely difficult to solve since they contain hyperbolic characteristics, but are essentially parabolic. The problem can be simplified by looking for similarity solutions. Greifinger and Cole (Ref. 3) have done this for essentially the same equations with $\sigma = \infty$. Assuming infinite conductivity, however, removes all diffusion effects, and for a similarity solution to apply, requires the current sheet to be infinitely thin. Thus the problem is the same as for an ordinary solid piston. In their case, they have

included an axial magnetic field which remains proportional to the density and doesn't complicate the problem. With $\sigma = \infty$, equations (22) yield similarity solutions in any variable $\xi \propto r/t^{n'}$, n' being determined by the boundary conditions. For a finite conductivity, similarity can also be achieved for any n' , but choosing n' will determine the radial or time dependence of σ . The most natural choice for the conductivity would be $\sigma = \text{const.}$, which can be fitted into a similarity solution only for $n' = \frac{1}{2}$. (This is due to the parabolic diffusion of the current sheet $\Delta r \propto \sqrt{t}$.) However, this type of similarity corresponds to a constant driving current, for, choosing B in the form $B = \sqrt{\rho_0 \mu_0} \frac{r}{t} B(\xi)$ and looking at the solution for a fixed large time behind the current sheet, B must approach a $1/r$ dependence. Hence $B \rightarrow \frac{r}{t} \frac{1}{\xi^2} \propto \frac{1}{r}$. All inverse pinches use a sinusoidal driving current provided by a simple capacitor discharge into an inductive circuit. This can be approximated by a linear current for the initial phase and requires a $\xi \propto r/t$ dependence, yielding $B \rightarrow \frac{r}{t} \frac{1}{\xi^2} \propto \frac{t}{r}$ behind the current sheet. The constant current solution is less interesting from a practical viewpoint since the resultant shock waves would propagate at non-constant speeds. However, to fit a similarity solution to the realistic, linearly increasing driving current, a $\sigma \propto 1/r$ dependence is required.

A conductivity dependence proportional to $1/r$ yields

a linearly expanding current sheet due to the constantly expanding diffusive length scale proportional to $1/\sigma$. This linear spreading is observed experimentally, and can be accounted for by two factors. (1) If the current sheet originally forms with a finite width, the parabolic spreading may not be distinguishable from a linear growth over the length scales involved. Even if the breakdown region is narrow, the spreading at large radii will still appear linear over small distances. (2) The conductivity depends on the electron temperature, which, in turn, depends on the ohmic heating. As the current sheet diffuses, the current density decreases and the ohmic heating is reduced, yielding an approximate $1/r$ dependence in the conductivity. This can also be thought of as a decrease of the directed electron velocity necessary to carry the decreasing current density J , likewise yielding a $1/r$ dependence in the conductivity. Obviously the first factor is important, but an observation of the experimental current sheet growth, as seen in figures 14, 24, and 31, shows that the linearity cannot be fully accounted for by this inability to distinguish a parabolic growth rate from a linear one. Therefore, the $\sigma \propto 1/r$ relation has merit other than just making the calculations possible. It cannot hold near the center of the device but, of course, the central region is not well defined experimentally. A full discussion of the importance of the various approximations will be postponed until

section IV where the similarity solutions to be developed here will be used to interpret the experimental results and to estimate the conductivity. The extreme usefulness of the similarity description will then become evident. Suffice it to say here, that it is a good approximation for at least portions of the flow field, and will give quantitative results as to shock formation position, but care must be exercised in interpreting these results.

Choosing $\sigma = \frac{\sigma_0 r_0}{r}$ and a similarity variable $\eta = \frac{r}{Ut}$ where U is some characteristic speed related to the force field speed used earlier, equations (22) can be written in the following simplified form:

$$\begin{aligned} (-\bar{u}_\eta) &= \frac{1}{1-s} \left\{ \frac{\beta}{\eta^2 \Phi} j - s \frac{\bar{u}}{\eta} \right\} \\ (-\bar{\rho}_\eta) &= \frac{\bar{\rho}^2}{\Phi \eta} \left\{ (-\bar{u}_\eta) - \frac{\bar{u}}{\eta} \right\} \\ (-j_\eta) &= \eta R_m \left\{ \frac{\Phi}{\bar{\rho}} (-\beta_\eta) - \frac{\beta}{\eta} (-\bar{u}_\eta) \right\} \end{aligned} \tag{23}$$

$$p \propto \rho^\gamma .$$

The normalized variables used are:

$$\bar{\rho} = \rho/\rho_0, \quad \bar{u} = u/U, \quad \beta = B/U\sqrt{\rho_0\mu_0}, \quad j = \eta(-\beta_\eta) - \beta .$$

Also, $R_m = \mu_0 \sigma_0 r_0 U$ is assumed constant, but the equations can be modified to let it vary with η ($\sigma_0 = \sigma_0(\eta)$). The new variables introduced are:

$$\phi(\eta) = \bar{\rho} \left(1 - \frac{\eta}{\bar{\rho}}\right) \quad (24)$$

$$S = K \frac{\bar{\rho}^{-\gamma+1}}{\eta^{2\phi} 2} \quad K = \frac{\gamma p_0}{\rho_0 U^2} = \frac{1}{M_F^2} \quad (25)$$

which have a special significance. Greifinger and Cole expressed their simplified version of equations (22) in terms of a stream function Ψ defined by $\frac{\partial \Psi}{\partial r} = (\rho/\rho_0)r$, $\frac{\partial \Psi}{\partial t} = -(\rho/\rho_0)ur$, and a variable $\phi = 2\Psi/r^2$ which they showed to be equal to the expression in equation (24). Then,

$$\phi = \frac{\int_0^r 2\pi r' \rho dr'}{\rho_0 \pi r^2} = \frac{\int_0^\eta 2\pi \eta' \bar{\rho} d\eta'}{\pi \eta^2} \quad (26)$$

is the ratio of the mass between η (or r) and the center, divided by the mass originally there. Thus $\phi(\infty) = 1$ and $\phi(\eta_c) = 0$, where η_c is the contact surface between gas and vacuum at which $\bar{u} = \eta_c$. S is the converted pressure term whose magnitude depends on the parameter K , which is given by the initial conditions. Calling "a" the sound speed $\sqrt{\gamma p/\rho}$, S can be shown by simple substitution to be the inverse of the local Mach number squared:

$$S = a^2 / \left(\frac{r}{t} - u\right)^2 .$$

Thus the characteristic Mach number M_F is again found to be important, and the additional parameter governing the current sheet width is the magnetic Reynolds number as

might have been expected. The exact Mach number dependence will be seen from numerical calculations, but its qualitative effect can easily be determined. Equations (23) are singular at $S = 1$, as should be expected when the incoming flow is decelerated to sonic velocity in current sheet fixed coordinates. Allowance must be made for a discontinuity, which dictates that a shock must be present. For a large value of K (small M_F), S will approach unity quickly and the shock will be located at the front of the current sheet. Again, this is the same supersonic choking noticed in the force field model.

The only difficulty in numerically integrating equations (23) is knowing how to start. Greifinger and Cole expressed their equations in terms of the independent variable ξ , put in a shock at $\xi = 1$, and started integrating at the known conditions behind the shock. In the present case the shock position is unknown and must be found by an iterative procedure. In terms of ξ , the equations exhibit a saddle point behavior at $\xi = 1$, and it is impossible to start the integration procedure there. However, in terms of η , a linearized solution $(-\beta_\eta) = \frac{A}{\eta} e^{-R_m \eta}$ is applicable when $\eta \rightarrow \infty$, and the integration can proceed from this initial path. A governs the magnitude of the drive current and will be related to it through the actual solution. A computer program, shown in appendix C, performs the desired integration for a given A , K , and R_m . (A is

denoted by RKAPPA, K/γ by CO, and R_m by RMOLD in the program.) It searches for a shock position as the singularity $S = 1$ is approached, the exact shock position being determined by requiring that the pressure be zero at $\phi = 0$, since for finite conductivity there can be no jump in the magnetic field to support any pressure at the rear of the current sheet. The shock jump conditions are standard, with energy rather than entropy conserved. Neither the current nor the magnetic field can jump across the shock. A jump in conductivity is allowed for by setting $R_m = RMNEW$ behind the shock, but in all the runs made here RMNEW was set equal to RMOLD. The conductivity σ_0 was, however, set proportional to the electron temperature to the three-halves power behind the shock, and the electron temperature was assumed to behave adiabatically. This is not a good assumption, but it had little effect on the solution and was necessary in some cases to assure convergence of the iterative procedure and to insure that the current went to zero when the density did. The lack of influence on the solution demonstrates the weak dependence on the exact form of σ .

Solutions were obtained for various combinations of R_m and K , to cover the experimental region of interest in the inverse pinch. Initial values of A were chosen to place the current sheet near $\eta = 1$ for purposes of comparison. Since $R_m = \mu_0 \sigma_0 r_0 U$, each solution corresponds to

many different combinations of $(\sigma_o r_o)U$. Choosing to think of U as fixed, varying R_m corresponds to varying the conductivity. If the conductivity is assumed fixed, then varying R_m corresponds to varying the characteristic current sheet speed, and hence $K = a_o^2/U^2$ must be changed if the same initial condition a_o is desired. Equating the magnetic field at the contact surface (denoted by a subscript c) to the driving current, $I = I_o \omega t$, necessary to produce it, the experimental condition corresponding to A is arrived at.

$$B_c = \frac{\mu_o I_o \omega t}{2\pi r_c} = \frac{\mu_o I_o \omega}{2\pi U \eta_c}$$

$$u_o = \frac{U}{2^{1/4}} \sqrt{\eta_c \beta_c} \quad (27)$$

$$u_o = \left\{ \frac{\mu_o I_o^2 \omega^2}{8\pi^2 \rho_o} \right\}^{1/4}$$

u_o is the snowplow speed first suggested by Rosenbluth, which is derived from a momentum balance assuming that all the mass is swept into a thin sheet. It is the third numerical parameter desired rather than A . The experimental conditions $(\sigma_o r_o)$, a_o , and u_o are thus determined from R_m , K , and equation (27) where η_c and β_c are given by the numerical solution, which acts as the relationship between A and u_o . The specific heat ratio is also supplied and was taken as 1.67.

2.3 Numerical Results

Table 1 contains a summary of the computer solutions with the notation indicated in figure 5. Figures 5 and 6 are typical results for large and small Mach numbers. M_s is the effective Mach number of the shock with respect to the gas immediately ahead of it. It is always lower than the Mach number with respect to the initial conditions since the gas is heated and accelerated before the shock reaches it, thus raising the sound speed and lowering the relative velocity. For completeness, the ratio u_o/U is also given. This ratio has been kept as close to unity as possible in order to give U some physical meaning, since U is used to define the parameters R_m and K and the similarity variable $\eta = r/Ut$. Instead of listing K , which was supplied to the computer, the Mach number M_o , based on u_o is shown in table 1.

$$M_o = \frac{u_o}{U} \frac{1}{\sqrt{K}} = \frac{u_o}{a_o} .$$

The magnetic Reynolds number R_m is left in terms of U . For an example of the quantities involved, consider $R_m = 4$ and $U = 2$ cm/ μ sec; it is found that the corresponding $(\sigma_o r_o)$ is 16,000 with r_o expressed in centimeters and σ_o in mhos/meter. If the conductivity is dominated by Coulomb collisions, this corresponds to an electron temperature of approximately 2.9 ev at $r_o = 1$ cm. However, it is

difficult to interpret $\sigma_o r_o$ for cases where the current sheet does not originate in a thin sheet. Later, in section IV, where some experiments from the inverse pinch are described, an initially thick current sheet is accounted for by defining an effective origin at some $-R_o$.

The values of R_m used in the numerical solution were chosen to yield current sheets of approximately the same dimensions as observed experimentally. From table 1 it is seen that the effect of the initial Mach number becomes less important as the current sheet is made thinner (increasing R_m). For the wider current sheets the value of M_o is very critical in determining the shock position. For large Mach numbers the shock is located in the very rear of the current sheet ($\eta_s \approx \eta_c$); while for small Mach numbers, the shock is located near the peak current ($\eta_s \approx \eta_p$). As the current sheet is made thinner, the variation of shock position with Mach number becomes less smooth. For the case $R_m = 6$ the shock was located at the current peak for all Mach numbers investigated. However, for the case $M_o = 69.5$, it was found that a second solution (not tabulated) developed with the shock located in the rear. This does not mean the solution is non-unique, because the two solutions corresponded to slightly different boundary conditions. If the Mach number is increased it is expected that this rearward solution would predominate. This discontinuous nature of the solution has been observed as an instability in the

actual experiments as will be shown. A reasonable explanation for this is that the dimensions of the current sheet have been reduced to the ideal separation distance between a shock and a solid piston which means that shocks are more difficult to form in the rear of the current sheet, unless large compression ratios are obtained.

For the range of interest, increasing R_m does not cause the shock to move past the current peak. This is partially due to the incorrect conductivity distribution $\sigma_0(\eta)$ assumed behind the shock. If a better approximation were used the current peak would be located further to the rear. It is noticed, however, that the relative position of the shock with respect to the total current sheet width does move forward. This result is relatively independent of the exact current distribution and is assumed to be correct. The actual total width of the current sheet does not decrease proportionately as R_m is increased. This is due to the fact that behind the shock the current is moving with the fluid, but in front of it, the current sheet must diffuse against the fluid velocity. Thus, the rate of diffusion appears much greater behind the shock, and these expansion regions will be wider than the corresponding regions ahead of the shock. For this reason R_m must be increased to very large values before the limiting case of a separated shock can be achieved. Unfortunately, increasing R_m by increasing the current sheet velocity also increases M_0 and the shock

tends to form further back. Methods of counteracting this effect will be discussed in section VI.

From the above discussion it becomes obvious why all previous attempts to produce separated shocks have failed. It is difficult to achieve electron temperatures much above 5 ev, which would increase the conductivity of the gas. Also, attempts to produce thin current sheets by driving them at high velocities are partially self-defeating because of the high Mach numbers produced, with the result that the shock forms more toward the rear. These numerical results are applicable even where the $\sigma \propto 1/r$ dependence is not strictly obeyed. In fact, they set an upper limit of performance up to the point r_0 for flows where the conductivity is a constant σ_0 , since the spreading in that case would be greater than in the higher conductivities of the conical case. The only effective method of destroying the similarity effects with respect to the current sheet diffusion is to have the shock itself influence the conductivity. If Coulomb collisions are dominant, it can only do this by raising the electron temperature above a few electron volts, which would necessitate very high Mach number shocks. Of course, the shocks would then be formed in the rear, and the deviation from similarity in the narrow region behind the shock would have little effect. For low degrees of ionization, collisions with neutrals might be important and the shock could have some effect in increasing the ioniza-

tion or the dissociation of diatomic gases, thus changing the electron-neutral collision contribution to the conductivity. All this will become clearer in the next section when applied to the experiments performed.

The main value of this model in providing a point of view from which to evaluate the experiments must again be stressed. All deviations from single-fluid behavior will be discussed based on this conical model, and the model will be extended as far as possible to cope with these deviations.

IV. EXPERIMENTS

4.1 Description of Apparatus

All the experiments were run in an inverse pinch of the standard design originally developed by Liepmann and Vlases (Ref. 7). The actual construction was governed by the desire to locate the device between the poles of a large electromagnet with 12 inch diameter pole pieces placed 4 inches apart. The inverse pinch is shown in figure 7 along with the circuit parameters. Provision has been made for preionization through the use of the smaller 28 μf capacitor bank which can be charged to a high voltage. Switching is performed by a thyrotron-ignatron combination described elsewhere (Ref. 8). The small gap distance between the electrodes of the inverse pinch was necessitated by the thickness of the glass plates necessary to support the pressure difference over the 10 inch diameter. The use of glass electrodes eliminated electrode (Ref. 6) effects, and since boundary layer effects were negligible, the current sheet discharge was uniform over most of the length.

Since the problem of shock production by current sheet drivers was not understood, and is complicated enough in its own right, no attempt was made to study the problem of MHD shocks with an axial field present. The behavior of the inverse pinch in the presence of axial magnetic fields is discussed briefly in subsection 4.3. The use of pre-

ionization, which is discussed in subsection 4.2, was distinguished only by its ineffectiveness, the reasons for which will be discussed later. However, the preionization bank was put to an originally unforeseen use in conjunction with the theory developed in the last section. Thus, the main emphasis of the experiments is a detailed analysis of the factors influencing the formation of the driven shock, and the shock's interaction with the driving current sheet. This process must be well understood before any more complicated cases can be studied.

Many techniques are available for probing the structure of the current sheet. The two most useful by far, however, are the use of insulated induction loops for measuring \dot{B}_0 and hence inferring the current distribution, and the use of fast risetime piezoelectric pressure probes for defining the shock position. These probes are described in detail in reference 8. The only differences between the probes described in reference 8 and those used in this investigation are that a stainless steel backing bar was used instead of a brass one in the pressure probe to reduce the radial ringing (Ref. 9), and that a small diameter (1 mm) loop was employed for measuring \dot{B}_0 to investigate the detailed current sheet structure. The close relationship between \dot{B}_0 and the current density J can be seen from the numerical solution in figure 8. In fact, in some calculations \dot{B}_0 is a more useful experimental measurement

than J , as will become evident in subsection 4.4. Electric field probes, originally developed by Loveberg (Ref. 10), give information about the composition of the plasma, as discussed in subsection 3.1, rather than about the structure of the current sheet, and were not used in this study. However, the results obtained by Sorrell (Ref. 6) in this laboratory will be referred to as a check on the methods developed here to obtain the same information.

4.2 Preionization Survey

In normal operation, MHD shock tubes are run in a cold gas with the driving current sheet itself ionizing the gas and creating the plasma. Ideally, if a shock were to separate from the current sheet, it would be a so-called ionizing shock, which has been successfully studied only theoretically, although experimental attempts have been made (Ref. 11). The ionizing shock would create the high temperature plasma in which the current sheet is supported. At high Mach numbers electron temperatures may be produced which are high enough to limit the current sheet diffusion to a minimum. However, in actuality, no truly separated shocks have been produced, and at the high Mach numbers necessary to produce high temperatures, the shocks tend to be located in the rear of the current sheet where they are ineffective in heating the gas.

In an attempt to obtain high electron temperatures by other means, the technique of preionization has been employed. The motivation behind preionization is to create a plasma of such high temperature and high conductivity as to limit the current sheet thickness to a size so thin as to force the shock to separate. The fallacy here is the pre-supposition that higher electron temperatures can be achieved than those due to the driving current sheet itself. A more likely effect to be noticed is that due to the reduction of the current sheet Mach number because of the

heating of the heavy particles.

Klein (Ref. 12) has made a detailed study of the effects of preionization by running his inverse pinch in the region behind the incident and reflected shock waves in conventional shock tubes. However, for reasons he discusses, the test conditions are less than ideal, and additional complications arise. He observed no influence on the current sheet diffusion and did not conduct any experiments under conditions where the theory developed in section III would predict much influence on the shock position. Thus, he noticed only a small effect.

The method of preionization used here was to discharge a smaller capacitor bank at a higher voltage into the device, and then fire the main bank after the first discharge had died down. The lack of knowledge about, and the non-uniformity of the resultant preionized plasma were the factors that led Klein to conduct his studies in the ordinary shock tube. In hydrogen, the effect of these non-ideal conditions was to prevent the formation of the thin current sheets shown in figures 26 - 33, and the result was the structure shown in figure 9. This is a similar structure to that observed when the electrodes become worn or extreme care is not taken to insure purity of the original gas. In figure 9 and the following similar figures, the shock trajectory and the distinguishing features of the current sheet are plotted. An actual oscilloscope trace is reproduced

with time running from right to left. This profile can also be thought of as a current sheet at a given time propagating from left to right. Only the shapes of these profiles have significance since they are made at different radial positions and at different voltage sensitivities. Once the depicted shape was achieved, it retained the same form, although of course it diffused with time. The actual widths and diffusion rates can be found from the plots of the trajectories.

No particular care was needed to produce uniform, well defined, and reproducible current sheets in argon. This is evident by the lack of scatter in figures 10 and 12 where each set of points was made with the probes at a different radial position. The reproducibility is probably due to the lack of influence of the initial breakdown on the shock position, which influences the current sheet structure. In figure 9 the double humped structure results from the non-uniformity produced by the shock located between the humps. In figures 10 through 13, no pressure probe was used and the indicated shock position is the location of the first discontinuity in the current sheet structure. Pressure probe measurements indicate that this first discontinuity in argon leads the shock by about 2 mm, but this is within the experimental accuracy in positioning the probes and deducing the delay time in the pressure probe. However, the discontinuity is expected to be in front of the shock

so the calibration appears correct. In all other figures the shock trajectory is obtained from the pressure probes. The definition of position 3 as the rear of the current sheet is arbitrary. However, the finite amplitude of the \dot{B}_θ trace after this point is misleading since the linearly rising drive current will produce a significant voltage on the \dot{B}_θ probe after the current sheet has passed. This is especially noticeable in argon where the current sheets are thicker and slower.

The effect of non-linearity of the sinusoidal drive current is evident near the quarter cycle time of 6μ sec. It is evident, however, from figures 10 and 12 that the current sheet growth appears linear. The speed of the peak of the \dot{B}_θ trace has been used as a reference to determine the effectiveness of the current sheet in sweeping up the initial gas, and also the influence of impurities that are burned off the electrodes by the arc. Referring to figure 5, it is seen that most of the mass is accelerated in front of the shock and the use of the \dot{B}_θ peak in a comparison with the snowplow speed is justified for argon. The importance of determining exactly where the swept mass is located will become evident for the shots in hydrogen.

In figures 11 and 13 the main bank was fired 80μ sec after the preionization bank. The effect of the preionization on both current sheet structure and shock position is negligible. The higher velocities are due to some of the

initial gas being driven to the outer walls and maybe out of the device through the vacuum port. The current sheet in figure 11 may be thinner due to this higher speed. The actual conductivities in all four cases are estimated in subsection 4.5. The additional scatter in the data due to preionization is especially evident in figure 11. The rapid diffusion of the current sheet near the outer portion of the device may be due to the non-uniformities introduced by the preionizing process, such as a dense cold layer on the outer walls. This tendency was also noticed in some cases by Klein, but may have been due to the shock tube wall boundary layers which were present in his experiment.

4.3 Axial Magnetic Fields

The simplest type of MHD shock involves only a magnetic field perpendicular to the flow direction. Jump conditions are derived analagous to the ordinary Rankine-Hugoniot relations for the limit of thin shocks. The actual structure of the shock now depends not only on the viscosity and thermal conductivity, but on the resistivity of the gas. Marshall (Ref. 1) discusses the various limiting cases where one of the three dissipative mechanisms is larger, and he finds shocks within a shock, the thicker shock structure being determined by the larger dissipative mechanism.

In most cases of interest in the inverse pinch the ordinary gas dynamic shock is thin while the structure of the axial magnetic field compression is thick (on the order of a centimeter). This axial field structure is still of interest, but it would require a larger flow field than is available to observe it. Since the ordinary shock is contained in the driving current sheet and the dimensions of the current sheet are also determined by the resistivity of the gas, the current sheet and the axial magnetic field structure will be of the same dimensions and occupy the same region. Thus, the structure of the axial field compression will be determined by the flow field of the current sheet, rather than the flow induced by the shock alone. This can easily be seen by the trajectories of the

current sheet, represented by solid lines, and those of the axial field compression, indicated by the broken lines in figure 14. In the ideal case the axial magnetic field would be expected to jump across the shock. Here, the compression takes place ahead of the shock and is of the same dimensions as the current sheet. The axial field is coupled to the current sheet only through the induced velocities, and since the flow field in argon has a very steep compression region ahead of the shock, which itself resembles a shock (figure 5), the axial field compression is not much different than it would be for a shock acting alone. The fact that it leads the current sheet is due solely to its diffusion rate, and is no sign of any flow acceleration ahead of the current sheet.

Greifinger and Cole have computed similarity solutions for the infinite conductivity case that show that the effect of an axial magnetic field is to increase the shock velocity and decrease the current sheet velocity. This is due to the effective pressure of the axial field compression. Originally, it was hoped that this effect would enhance separation. However, in the actual case with the axial field compression ahead of, rather than behind the shock, no such effect on separation can be assumed. In fact, from figure 14, it appears that exactly the opposite effect is true. The mass is compressed near the shock, and its velocity must be lowered due to the effect of the axial

magnetic pressure. The current sheet appears to be propagating at a higher velocity than in figure 12 due to the fact that it was initially thinner and is diffusing at a faster rate. This points out one advantage of axial magnetic fields, in that thinner current sheets can be produced initially, enhancing forward shock formation. However, the end results do not seem to be improved. The current sheet expands to its normal width, and the shock assumes its normal position in the rear of the current sheet. One should also notice that the current sheet spreading is very linear even though it broke down fairly thin. This, in part, confirms the assumptions made in deriving the previous conical solutions.

One disadvantage of using an electromagnet to produce the axial magnetic field is the close proximity of the high μ pole pieces to the experiment. The magnetic field lines are tied to the pole pieces and must be stretched as well as be compressed by the current sheet, producing an additional retarding force on the sheet. For large values of axial magnetic field the current sheet can not propagate against this force, and it is confined to the center of the device except for diffusion and instabilities. The instabilities introduced can even be seen at low values of axial field as shown in the oscilloscope trace reproduced in figure 14. They are due to the gas in the rear of the

sheet being pushed backward by the decreasing portion of the axial field, which is an unstable configuration.

4.4 Numerical Techniques - Estimation of Conductivity and Degree of Ionization

In order to treat the experimental data intelligently, it is absolutely essential to have some means of estimating the conductivity of the gas, and to a lesser extent, its degree of ionization. Unfortunately, the calculations most commonly referred to, Falk and Turcotte's (Ref. 13), are not applicable to the phenomenon observed in the inverse pinch. They assume a shock well separated from the current sheet and propagating at a speed proportional to \sqrt{t} so that similarity solutions can be found for $\sigma = \text{const.}$ However, the most serious defect of their method is that inertia terms are ignored, which is correct in their limit but is totally wrong for the case when the shock is not separated from the current sheet. In the case of no separation, the gas velocities go from zero up to the current sheet speed. Since the current sheet diffusion takes place with respect to the plasma, the speed of the plasma at each point in the current sheet greatly influences the apparent diffusion and the current sheet structure. Their estimate of the current sheet size as approximately equal to $\sqrt{t/\mu_0 \sigma}$ may lead to estimates of conductivity that are off by an order of magnitude.

Aside from the difficulty of accounting for the plasma velocity theoretically, it is necessary to find some characteristic quantity that may be measured experimentally.

For a constant speed current sheet, a uniform conductivity would give rise to parabolic diffusion. However, even if this were the case, it would be impossible to evaluate this parabolic spreading to any degree of accuracy, since the data presented show the current sheet spreading linearly after the initial few centimeters.

The previous similarity solutions can prove extremely useful now, but the initial width at $r = 0$, due either to a finite breakdown width or initial parabolic diffusion, must be accounted for. This can be done by assuming an imaginary origin at $-R_0$, and a conductivity of the form

$$\sigma = \frac{\sigma_0 (r_0 + R_0)}{r + R_0} = \frac{\sigma_0 r_0'}{r'}$$

For large R_0 this yields an approximately constant conductivity and the results can be expected to be very accurate. However, for cylindrical geometry similarity is not strictly observed in the primed coordinates as it would be for linear geometry. In order to separate the effects due to violation of similarity from the true theoretical behavior under the given assumptions, the following analysis will be carried out for both linear and cylindrical geometries.

For linear geometry the conductivity is assumed to be of the form $\sigma = \sigma_0 (x_0 + X_0) / (x + X_0) = \sigma_0 x_0' / x'$. Then the respective induction equations become:

$$\frac{\partial}{\partial x'} \left(\frac{x'}{\mu_o \sigma_o x_o'} \frac{\partial B}{\partial x'} \right) = \frac{\partial B}{\partial t} + \frac{\partial}{\partial x'} (uB) \quad (28)$$

$$\frac{\partial}{\partial r'} \left(\frac{1}{\mu_o \sigma_o r_o'} \frac{r'}{r} \frac{\partial}{\partial r'} (rB) \right) = \frac{\partial B}{\partial t} + \frac{\partial}{\partial r'} (uB) \quad (29)$$

To arrive at analytic answers, these equations will only be used in regions where u is constant. From the numerical solutions of section III, this is seen to be the case in the front of the current sheet for heavy gases where $u \approx 0$, since all the compression takes place at the very rear. For light gases the conditions behind the shock are not very accurate since real gas effects have been ignored, but a good approximation is that u is constant and equal to the speed of the rear of the current sheet. Under this assumption of constant u , and using the notation of section III where η is either x'/Ut or r'/Ut and R_m equals $\sigma_o \mu_o x_o' U$ or $\sigma_o \mu_o r_o' U$, equations (28) and (29) become:

$$\text{Linear: } \frac{\partial}{\partial \eta} \left(\eta \frac{\partial B}{\partial \eta} \right) = R_m (\bar{u} - \eta) \frac{\partial B}{\partial \eta} \quad (30)$$

$$\text{Conical: } \frac{\partial}{\partial \eta} \left(\eta^2 \frac{\partial B}{\partial \eta} \right) = R_m (\bar{u} - \eta) \frac{\partial B}{\partial \eta} + \frac{R_o \eta}{r' - R_o} \left\{ \frac{\partial B}{\partial \eta} + \frac{r'}{r' - R_o} B \right\} \quad (31)$$

Equation (31) is similar only for $R_o = 0$. However, it can be seen from the solution that $\partial B / \partial \eta \approx -r'B / (r' - R_o)$. The last term is small so that equation (31) is approximately

similar. Obviously this is not true for small $r = r' - R_0$, but the approximation should be good elsewhere. Equation (30) will be solved to see the exact effects when similarity is strictly obeyed. Ignoring the non-similar term, equations (30) and (31) have the solutions:

$$\text{Linear: } \frac{\partial B}{\partial \eta} = - A\eta \left(R_m \bar{u} - 1 \right) e^{-R_m \eta} \quad (32)$$

$$\text{Conical: } \frac{\partial B}{\partial \eta} = - A\eta \left(R_m \bar{u} - 2 \right) e^{-R_m \eta} \quad (33)$$

where A is some constant. What is measured experimentally at a given r' is:

$$\dot{B} = - \frac{U}{r'} \eta^2 \frac{\partial B}{\partial \eta} = \frac{UA}{r'} \eta \left(R_m \bar{u} - 1 \right) e^{-R_m \eta} \quad (34)$$

for cylindrical geometry.

Equation (34) gives the theoretical profile for a portion of the current sheet where u is constant. R_m can be found from measuring \dot{B} at any two points in a region of constant u or from the slope $\frac{\partial}{\partial t} (\dot{B})$ at any point in such a region. Choosing two points 1 and 2, and calling

$$\eta = \frac{1}{2}(\eta_1 + \eta_2), \quad \Delta\eta_{12} = \eta_1 - \eta_2:$$

$$R_m \approx \frac{\log(\dot{B}_2/\dot{B}_1)}{\Delta\eta_{12} (1 - \bar{u}/\eta)} \quad (35)$$

or

$$R_m \approx \frac{(r'/UB) \frac{\partial \dot{B}}{\partial t}}{\eta^2 (1-\bar{u}/\eta)} \quad (36)$$

Now $\sigma_o = R_m / \mu_o r_o' U$, and calling the point of measurement $r' = r_o'$, $\Delta r_{12} = \Delta r'_{12} = r_o' \Delta \eta_{12}$, equations (35) and (36) become:

$$\sigma_o \approx \frac{\log (\dot{B}_2 / \dot{B}_1)}{\mu_o U \Delta r_{12} (1-\bar{u}/\eta)} \quad (37)$$

$$\sigma_o \approx \frac{\frac{1}{\dot{B}} \frac{\partial \dot{B}}{\partial U t}}{\mu_o U \eta^2 (1-\bar{u}/\eta)} \quad (38)$$

For $\bar{u} = 0$ equation (37) states that σ_o is only dependent on the width of the \dot{B} profile at r_o' and not on the initial breakdown width. This means that a wide breakdown with R_o large ($r' \approx r_o'$) and $\sigma = \sigma_o r_o' / r' \approx \sigma_o$ will spread to the same width at r_o as will an initially thin current sheet, with R_o small, propagating into a more highly conducting region, $\sigma = \sigma_o r_o' / r' > \sigma_o$ ($r_o' = r_o + R_o > r' = r + R_o$). Looking at some fixed time instead of a fixed radial position, the \dot{B} profile would be wider for the initially wider current sheet propagating into the lower conductivity plasma, as would be expected, but this effect is only slight. This strange behavior is not due to the lack of strict similarity since equation (32) for the

linear geometry yields the same result as equation (37) for

measurements at fixed t ($\frac{\partial B}{\partial t} = -\frac{\eta}{t} \frac{\partial B}{\partial \eta} = \frac{A}{t} \eta^{\overline{u}} e^{-R_m \eta}$). In

fact, for corresponding measurements at fixed x ,

$$B \propto \eta^{(R_m \overline{u} + 1) - R_m \eta} \text{ and,}$$

$$\sigma_o = \frac{\log(\dot{B}_2/\dot{B}_1) + \Delta x_{12}/x_o' \eta}{\mu_o U \Delta x_{12}} \quad (39)$$

Thus, at $x = x_o$ an initially wide current sheet (x_o' large) spreading to the same Δx_{12} as an initially thin one, will correspond to a smaller σ_o .

For \overline{u} not equal to zero, the term $(1 - \overline{u}/\eta)$ is important since \overline{u} may be nearly equal to η . Now, for an initially wide current sheet, $\Delta \eta_{12}$ is small for a given $r_{12} = r_o' \Delta \eta_{12}$ and $(1 - \overline{u}/\eta)$ is small, requiring a much larger σ_o to keep the initially wider current sheet from spreading to a larger width than the initially thin one.

The unusual solutions to equations (30) and (31) for $\overline{u} = 0$ are due to the counteracting effect of the current sheet trying to diffuse against a relative incoming plasma velocity. The intuitive idea, that an initially thin current sheet, propagating into a gas of high conductivity must be narrower than an initially thick current sheet, propagating the same distance into a lower conductivity gas, is incorrect. For $r \gg r_o$ the initially thin current sheet must be thicker since the conductivity decreases faster

than it does for the initially wide (large R_0) case. However, the fact that the cross-over point is at r_0 is not obvious, since up to that point the initially thinner current sheet was propagating into a gas of higher conductivity. This behavior is the reason why all the current sheets in argon at a given velocity seem to achieve the same characteristic width irregardless of their initial breakdown width (figures 11 and 14). Of course, the above argument breaks down and similarity no longer holds if the initial breakdown width is larger than the theoretically allowed width at $r = r_0$. This does not seem to be the case in the experiments.

For flows where the shock is not separated from the driving current sheet piston, the effect of the inertia term $(1 - \bar{u}/\eta)$ is large. If a shock were to form in front, the conductivity would have to increase by $1/(1 - \bar{u}/\eta)$ behind the shock to maintain even the same spreading rate as before the shock was formed. In the case where the shock forms in the rear, the spreading of the current sheet is not increased. The current sheet remains thin only because of the oppositely directed plasma flow. When the shock forms in front, the current sheet is in effect dragged with it, thus, greatly increasing the difficulty in achieving true separation. All this will become clearer in the actual applications of equations (37) and (38) to the experimental data. Both equations will be used since it is sometimes

more convenient to measure one quantity than the other.

Once the resistivity of the plasma has been found, the degree of ionization can be estimated in a very simple manner by equating the power loss due to ohmic heating to the energy per second needed to ionize the neutral atoms or molecules. This yields a maximum possible degree of ionization since there are radiation losses and thermal energy accumulation by the electron swarm. However, shock induced ionization is not accounted for, but this can be estimated in the standard manner for cases when a shock is produced in the front of the current sheet.

These factors will be discussed for each gas studied and additional estimates of the electron temperature will be made. The following calculations, based solely on the conductivity measurements, will be compared with, and used to check, the direct spectroscopic measurements of electron temperature and number density. Gross energy balance must be satisfied, and the direct measurements cannot violate this balance if they are correct.

Equating the power loss $J^2/2\sigma_0$ in the total current sheet width Δr to the energy gained per second by the incoming neutrals $n_{oi}(eu_{ei})U$, where u_{ei} is the ionization energy in electron volts, and n_{oi} is the number of ions formed,

$$J^2/2\sigma_0 = n_{oi}eu_{ei}U \quad . \quad (40)$$

This has a very simple interpretation in microscopic terms if J is written as $n_e e \bar{v}_{ed}$, where \bar{v}_{ed} is the average directed electron velocity in the axial direction, and if σ_0 is expressed as $n_e e^2 / m_e \nu_T$, where ν_T is the total electron collision frequency with ions and neutrals. Then $J^2 / 2\sigma_0 = n_e (\frac{1}{2} m_e \bar{v}_{ed}^2) \nu_T$, which is the total energy lost by the electrons assuming they lose all their directed energy in each collision. It is more consistent to keep the gross equations, and since $n_{oi} = \alpha n_0$, where α is the degree of ionization, and n_0 is the initial number density, it is found from equation (40) that

$$\alpha = \frac{J^2 \Delta r}{2 n_0 e u_{ei} U \sigma_0} \quad (41)$$

This α gives as an upper limit on the degree of arc ionization. The fact that it can be achieved was verified by calculating the appropriate excitation rates for the calculated values of electron temperature (Ref. 22).

4.5 Argon

Figure 15 shows a typical set of pressure and \dot{B}_0 measurements in argon at different radial positions, with r being measured from the edge of the center insulator, which itself has a radius of $\frac{1}{4}$ inch. The compression of the gas due to the current sheet is noticeable down to $r = \frac{1}{4}$ inch, but the shock itself is not fully formed until it reaches a distance of about $r = 1$ inch. Once the shock is formed, its thickness cannot be distinguished from the rise time of the probe, which is about $.1 \mu$ sec. The small response in the pressure trace before the shock arrives is due to electrostatic effects, and the oscillations after the shock has passed are due to the internal "ringing" of the piezoelectric crystal. It is evident from the theoretical profiles that the shock cannot really be completely distinguished from the rapid compression region in front of it, which yields a large dynamic pressure when stopped by the probe, but the two occur so close together that it is not necessary to make such a distinction. The similarity solution assumes that the current sheet forms at zero thickness and the shock forms immediately, but it is evident from the characteristics argument that for a finite formation width this is not the case. For argon it takes approximately 2μ sec for the characteristics to fully intersect and form the shock. The large width of the \dot{B}_0 trace in the first picture at $r = \frac{1}{4}$ inch is deceiving since

it is a time rather than space profile. The true breakdown width can be seen to be very thin from the trajectory plots in figures 18 - 22.

It is evident that the shock causes a small discontinuity in the \dot{B}_θ trace. This effect, due to the shock, is too far back to have any real influence on the current sheet structure, but it can be, and has been, used as an indication of the shock position (which is actually slightly behind it). This has the advantage of giving current sheet traces and shock positions at the exact same location in the device. In argon the current sheet is always perfectly symmetrical so either method of defining the shock position is equally good, but in light gases uneven electrode wear may cause some asymmetries. However, in those cases, the discontinuity has more structure and interpretation is more difficult; hence, care was taken to produce a symmetrical breakdown, and additional checking probes were used to insure that this was always the case.

A second discontinuity in the \dot{B}_θ trace is evident in the oscilloscope traces for argon, and its trajectory is plotted (position 4) in figures 19 - 22. It is located well behind the current sheet in the region where the \dot{B}_θ probe measures mainly the changing magnetic field due to the sinusoidal capacitor discharge. Based on the continuum intensity measurements made by Sorrell (Ref. 6) behind the current sheet in argon, this discontinuity is assumed

to measure the end of an expansion region behind the current sheet. This expansion region is predicted by the characteristics argument and is discussed in appendix A. The expansion implies that the total force is less than the maximum allowed value for the given current sheet speed. This must be due in part to the high pressures created in the narrow region behind the shock, causing the plasma to expand backward against the magnetic pressure. The same expansion region would be expected if the gas were not fully ionized and the neutral-ion collision mean free path were long, which would not allow the neutrals to be fully swept up. Neutrals, however, would not affect the magnetic field and distort the B_0 profile. No distortion was noticed in figures 16 and 18 at lower pressures, so it must be assumed that both neutrals and ions may be present.

Figures 16 - 22 show current sheet and shock trajectories under various conditions to illustrate the lack of influence of the exact experimental conditions on the gross behavior. The initial breakdown region is hard to define, but the current sheet does seem to be thin enough initially so that the initial diffusion is parabolic. However, from a distance of $r = 1$ inch up to the point where the non-linearity of the driving current becomes important, the current sheet appears to spread strictly linearly. This linear growth is used to define the speeds of various portions of the current sheet, which are indicated in

cm/ μ sec in the figures. These speeds are, in turn, used to define an apparent origin at $-R_0$. This origin is used in $r' = r + R_0$ to define $\eta = r'/Ut$, which is used in the calculations to determine conductivities. The theoretical conductivity distribution, of course, also depends on R_0 , since $\sigma = \sigma_0 r_0'/r'$, and for large R_0 , σ will be more nearly uniform.

The position of the shock, indicated by a heavy line in the figures, relative to the position of the rear of the current sheet, cannot be taken too literally. This uncertainty is due to the rear of the current sheet being arbitrarily defined as the position where a line tangent to the maximum slope of the B_θ trace intersects the time axis. Obviously there must be some force region behind the shock, so that figures 17 and 21 are misleading. However, as predicted theoretically, this region is exceedingly narrow. The speed of the various portions of the current sheet can be taken as an indication of where the swept up mass is accumulated, since the swept mass must move at approximately the snowplow speed u_0 . Leakage through the current sheet will cause the current sheet to propagate at a faster velocity, since the effective initial density is lowered. However, since u_0 is only proportional to $(\rho_0)^{-1/4}$, this effect is not large unless the leakage is great. There will also be a small counteracting effect tending to produce slower current sheets due to the breakdown occurring at the

outer edge of the insulator rather than at the center of the device. For all the runs in argon, except those at 14 KV, the B_{θ} peak (position 2) seems to move at more nearly the snowplow speed than the shock does. This is just an indication that the mass is swept up ahead of the shock, and is not to be taken as some magical property of the device. For other gases this will not be the case. At 14 KV the shock velocity seems to correspond more closely to the snowplow speed. This may be due to leakage, or to the shock forming initially in front of its similarity equilibrium position, as it appears to for the 400 μ Hg run. However, it may also be partially due to experimental inaccuracies, since the differences in velocities are only about 5%, which is of the order of the experimental error.

The conductivity in the front of the current sheet in argon is easy to calculate from either equation (37) or (38) since $\bar{u} = 0$ there. It is difficult to measure $\frac{1}{B} \frac{\partial B}{\partial t}$ accurately, so that equation (37) was used, with equation (38) being used as a check. σ_0 in all runs was calculated at $r = r_0 = 2\frac{1}{2}$ inches, and the results are presented in table 2. Also presented is the value of R_0 , the maximum possible degree of arc ionization α (as calculated from equation (41)), and the electron temperature u_e in electron volts. u_e is calculated from the conductivity by a method shown in section V. Since the current sheet has an effective finite width when the shock forms, it is difficult to

choose a magnetic Reynolds number R_m to correspond with the theoretical R_m used in the similarity solution. However, the shock tends to start forming at about $r = 1$ cm, and the experimental R_m , to be compared with the theory, must reflect the thickness of the current sheet at this point. Thus, in table 2, R_m is set equal to $.01 \mu_0 \sigma_0 U$, where U is the velocity of the B_θ peak. This definition is fairly arbitrary, but it does reflect an effective current sheet thickness to determine the shock position, and it is consistently applied for all the runs.

For the values of R_m and M_0 presented in table 2, it is evident, on comparison with table 1, that forward shock formation will never occur. The linear growth of the current sheet is sufficient to insure that the shock will not move forward relative to the sheet. Even if much larger devices were built, and the conductivity of the plasma were constant, no practical length would be sufficient to achieve separation. This inability to produce separation is due to the mass accumulation ahead of, rather than behind the shock. The mass accumulation and resultant plasma velocity would tend to spread the current sheet to even greater widths. The shock might even appear to move rearward due to slight leakages of the plasma, from the small amount of plasma accumulated behind it. This may account for the shock trajectories in figures 17 and 22.

The measured conductivity displays a tendency to increase with voltage and decrease with increasing initial density, as might be expected. The only exception is the 14 KV, 170 μ Hg experiment, which displays an abnormally low conductivity. This may be due to some double ionization taking place, since α is a good deal greater than 1, but it is not obvious why this should affect the conductivity. More likely, the small value of R_0 (initially thin breakdown) leads to an under-estimation of the conductivity, since the higher conductivities near the center, needed for the similarity solution to hold, are not present. Thus, the current sheet will spread more than is theoretically accounted for, and the inferred conductivity at r_0 will be too low. This effect is opposite to what would be intuitively expected, but the previous discussion in subsection 4.4 should make it clear why it occurs.

The values of α , reduced by about 20% to account for heating of the electrons, agree with Sorrell's measurements at 500 μ Hg, but not at lower pressures, where he finds $\alpha \approx .5$. Radiation losses may account for this discrepancy since the degrees of ionization measured here are too high. The values of electron temperature of approximately 2.7 ev seem to be characteristic of these devices, and agree with spectroscopic data. It is seen that this temperature, rather than a predicted temperature due to shock heating, must be used to evaluate current sheet thicknesses. Also,

the effect of the shock of increasing the plasma velocity and the current sheet spreading must be accounted for, even for non-similar flows. The similarity arguments, however, can be extended, as they were above, to predict the behavior. For argon, there is no hope of achieving separation unless the conductivity can be doubled through preionization. This explains the failure of previous attempts, where the required electron temperatures of above 5 ev were not even approached. To achieve such temperatures in equilibrium (through shock heating or otherwise), enormous amounts of energy would have to be expended, due to the losses to multiple ionization. Preionizing shock speeds of the order of those achievable only in MHD shock tubes would be necessary to produce the desired conductivities in the test gas behind the shock. This would make obsolete the MHD shock tubes, if such high speed separated shocks could be obtained by other means. For this reason, the following experiments were run in lighter gases, yielding higher current sheet speeds and lower Mach numbers.

4.6 Helium

Helium is the simplest light gas to analyze, and hence the least interesting since it exhibits no real gas effects. However, it does serve to illustrate the ideal behavior and it is useful in explaining the more complicated effects in diatomic hydrogen. Two runs are shown in figures 23 and 24 to demonstrate the effect of the shock on the current sheet. For the run made at 80 μ Hg initial pressure, the mean free paths, which will be discussed in section V, are too long to allow a thin shock to form. The shock structure itself is of the same length scale as the current sheet structure, and thus the inviscid, adiabatic fluid equations used in the theoretical models do not apply. However, the basic current sheet structure remains unchanged and appears to spread linearly. Its shape is basically like those of the argon runs, but of course no discontinuity is noticed at the rear due to a shock. There is, however, a small discontinuity at the B_0 peak, as illustrated in the trace in figure 24, which may be due to ionization induced by both the isentropic and non-isentropic compression within the wide structure. This structure is revealed as a region of increasing pressure by the piezoelectric probe, with no sharp front indicated.

For the run made at 250 μ Hg, the mean free path is approximately 1/3 the length of the 80 μ Hg mean free path, and a shock is formed, although it is somewhat thicker than

the shocks in argon. The shock's influence on the current sheet, mainly the tendency to drag it along in the accelerated gas behind the shock, is apparent. Before investigating the full significance of figure 23, however, the same basic calculations as were made for argon must be made here. Equation (38) is used, since there are not enough samples to choose the correct value of \dot{B}_2/\dot{B}_1 . For the 250 μ Hg run the term $(1 - \bar{u}/\eta)$ becomes important; $(1 - \bar{u}/\eta) = .225$ if \bar{u} is taken as the speed of the rear of the current sheet. σ_o is found to be 1.4×10^4 mhos/m behind the shock. The 80 μ Hg run is much more difficult to analyze, but if the slope $\frac{\partial B}{\partial t}$ is measured at the very front of the sheet, and \bar{u} is assumed equal to zero, the same value of conductivity, 1.4×10^4 mhos/m is found. The effective R_o for the 80 μ Hg shot is 1.5 inches, meaning that the initial breakdown is fairly thin. Due to the structure of the 250 μ Hg trajectories, it is impossible to find an effective R_o for the front of the current sheet, but it is small. The table below contains the same information as table 2 for argon.

Helium Data

Volts KV	Pressure μ Hg	U cm/ μ sec	M_o —	R_o in	σ_o mhos/m	R_m —	u_e ev	α —
9	80	2.9	34	1.5	1.4×10^4	5.2	2.7	.13
9	250	2.45	26	-	1.4×10^4	4.4	2.7	.07

These values of α agree fairly well with independent electric field measurements (Sorrell finds $\alpha = .068$ at $400 \mu \text{ Hg}$ and $u_0 = 2.45 \text{ cm}/\mu\text{sec.}$) The low degrees of ionization were surprising when first discovered by those other measurements, but from an energy balance point of view, it is obvious that higher degrees cannot be supported.

The shock itself may increase the degree of ionization, since for the $250 \mu \text{ Hg}$ shot, it is located in the front of the current sheet. The equilibrium conditions behind a Mach 24 shock ($2.45 \text{ cm}/\mu\text{sec}$) in helium are a temperature of 1.66 ev and a degree of ionization of .28. For the degrees of arc induced ionization in helium the electron collisions with neutrals contribute negligibly to the resistivity (Eq. 44) and only an increase in electron temperature will increase the conductivity. Depending on the relaxation time behind the shock, and the rate of energy transfer from the heavy particles to the electrons, the shock may have no effect whatsoever on the electron temperature. For the present case, with an initial degree of ionization ahead of the shock, the relaxation time is short, but the additional electrons created by shock ionization may tend to decrease the total electron temperature rather than raise it. This would have the effect of lowering the conductivity. Therefore, even at this high Mach number, the shock would be expected to have very little influence in increasing the gas conductivity behind it.

This is verified by figure 23. The degree of ionization, however, will be increased in the rear of the current sheet.

It is easy to interpret qualitatively what is happening in the current sheet and why the sheet diffuses faster behind the shock, but it is more difficult to relate these effects to the conical similarity solutions. Those solutions were useful in giving the exact behavior of a shock in argon and in explaining the effect of the plasma velocity on the current sheet spreading. However, they cannot be rigorously applied to determine the full current sheet profile and shock position when the current sheet is initiated at a finite width and the shock is not formed in the rear. The conical theory will accurately predict where the shock will form, e.g., for this value of R_m and M_0 , near the B_0 peak, but it cannot give the subsequent behavior because the current sheet is not conical with respect to the true origin. In calculating the conductivity, this could be accounted for by assuming an imaginary origin at $-R_0$, but the gas accumulation behind the shock must be based on the true origin. This is also true for linear geometries. Based on the true origin, the rear portion of the current sheet remains at a practically constant width. The shock speed, relative to the maximum force region (approximately at the B_0 peak), will be determined by the compression ratio across the shock. For a solid piston moving at a speed v_2 ,

and a shock moving at $v_2 + \Delta v$, and calling $\epsilon = \Delta v/v_2$, the effective density compression ratio is defined as,

$$C = 1 + 1/(2\epsilon + \epsilon^2) \quad . \quad (42)$$

Thus, in figure 23, with $\epsilon = .2$, equation (42) gives a C equal to 3.3. Since the shock and \dot{B}_θ peak are approximately conical (their trajectories intersect near the center of the device), and the ideal density compression ratio for helium at $M = 24$ is 4 (real gas effects increase this value), the expansion region must begin before the \dot{B}_θ peak. There must also be some gas in the very rearmost portion of the current sheet, so the effective compression ratio of 3.3 between the shock and \dot{B}_θ peak is a maximum. The net result shown by the above discussion is that the shock is separating from the \dot{B}_θ peak faster than it would from an ideal solid piston. It is seen once again that it is not leakage, but rather current sheet diffusion in the accelerated gas region that prevents full separation between the shock and the current sheet.

The two runs made in helium, and illustrated in figures 23 and 24, demonstrate the great usefulness of the theoretical models in explaining the observed phenomena, even in regions where the theoretical assumptions do not apply. Not only can the main characteristics of the current sheet and shock wave be easily explained in terms of simple fluid behavior, but the conductivity can be

estimated fairly accurately by a method exactly tailored to the experimental measurements. Also, now that a simple gas is understood, more complicated analysis can be attempted for gases where real gas effects may be important. This is done in the following subsection.

4.7 Hydrogen

Hydrogen is a difficult gas to analyze because of a combination of effects that add up to produce a plasma of rapidly varying conductivity. As will be seen in the next section, the electron-neutral elastic collision cross section for molecular hydrogen is so large that, for the low levels of ionization produced by the small current densities necessary to drive hydrogen, the electron-neutral collision frequency contributes significantly to the resistivity of the gas. This contribution disappears behind the shock due to both shock ionization and dissociation, the latter process being effective due to the much smaller electron-neutral elastic cross section for atomic, as opposed to, molecular hydrogen.

In order to observe the expected, shock produced effects in hydrogen, experiments were run at low voltages so as to produce lower Mach numbers, thereby enhancing forward shock formation. Runs at various Mach numbers and snowplow speeds were made to investigate the counteracting effects of increasing both the Mach number and the magnetic Reynolds number and, also, to attempt to observe the discontinuous type of behavior predicted by the conical similarity solutions. The now very critical influence of the shock on the current sheet should enhance the possibilities of observing any such effects.

Figure 25 shows the actual oscilloscope traces of a

run made at 6 KV and 700 μ Hg initial pressure in hydrogen. The position of the shock as shown by the pressure probe trace, and its influence on the current sheet, as represented by the B_0 trace, are clearly evident. The shock forms at about $r = 1$ inch, near the center of the current sheet as predicted. With time, it then moves forward relative to the current sheet, as the shock did in helium. However, in this case, the conductivity behind the shock is increased, and the main portion of the current sheet does not diffuse as rapidly as it would otherwise. The change in conductivity effectively divides the current sheet into two regions. The first region contains the portion of the current sheet in the low conductivity region ahead of the shock. This portion which is pushed forward by the shock, resembles the initial part of the helium current sheet. Behind this region there is initially an area of low current density which extends back to the main current sheet in region 2.

The different conductivities, and hence different diffusion rates, are the factors which give rise to the discontinuous behavior. For longer times, however, it is evident from equations (37) and (38) that the spreading rate will be proportional to $1/\sigma(1 - \bar{u}/\eta)$, so that although the conductivity is higher in region 2, the effect of the plasma velocity behind the shock will be to cause the main current sheet to expand to fill the total area behind the shock and prevent true separation. Since the initial

current in region 1 will decay rapidly, separation could be achieved if the ratio of conductivities after and before the shock would be greater than $(1 - \bar{u}/\eta)^{-1}$. Section V will show that this isn't the case and the measurements made at larger radial distances ($r = 3.5$ inches in this device plus subsequent measurements in larger devices (Ref. 14)) show the main current region expands to reach the shock and the initial low current density area disappears.

The behavior described above will be called normal, or ideal for hydrogen. The time intervals of interest here are the initial shock formation time, and the time interval during which the current sheet is divided by the shock into two regions. The third time interval, during which the main current sheet expands rapidly, is not of immediate interest in these experiments. Once the configuration of time interval 2 is achieved, it is easy to predict if full separation will be achieved. Thus, attention must be directed to the factors governing the initial shock separation from the main body of the current sheet.

Figures 26 - 32 show the current sheet and shock trajectories for runs made under various experimental conditions. One of the traces of figure 25 is shown in figure 26 with the time scale inverted, to show the positions plotted. Position 4, in the low conductivity region, moves at the same speed as the shock since it is the shock that divides the current sheet into two regions.

As the voltage was raised from 6 to $7\frac{1}{2}$ KV, the behavior became very erratic and was not reproducible. However, it was found that this was due to two separate solutions being possible; the one exhibited in figure 27, and another of the type shown in figure 28 at 9 KV. They were distinguished by keeping a third probe at a fixed position and grouping all runs together for which this third probe gave the same readings. At 9 KV the more rearward shock solution became dominant, altering the current sheet profile as shown in figure 28. The low conductivity region continued to diffuse at a rapid rate, which appeared to be the same rate the current sheet would diffuse if the shock were not present. Eventually for this case too, the shock began to separate from the main current carrying region.

The runs at $10\frac{1}{2}$ and 12 KV in figures 29 and 30 show further the complicated interactions introduced by increasing both the Mach number and magnetic Reynolds number simultaneously. It is impossible to predict accurately exactly what form the solution will take for these densities and voltages, but the details, while interesting, are not as important as the observation of the general tendencies. At 12 KV and 700 μ Hg it was so difficult to achieve the desired breakdown that only two shock positions are indicated. The other runs, like the runs made at higher voltages, resulted in current sheets of

the form shown in figure 9. In order to observe higher speed shocks in hydrogen with the desired characteristics, experiments were run at lower initial pressures, resulting in greater current sheet velocities. The complementary effects of higher speeds and delayed shock formation, due to the lower densities and longer mean free paths, resulted in effective magnetic Reynolds numbers great enough to offset the effect of the increased Mach numbers. High Mach numbers prevent forward shock formation in low R_m flows.

Figure 31 shows the trajectory of a $M_0 = 22.7$ current sheet run into 290 μ Hg of initial pressure. The behavior resembles that of the lower Mach number runs at higher initial pressures, except that the shock is formed later, at about $r = 1\frac{1}{4}$ inches. Reducing the pressure still further to 120 μ Hg results in the trajectories shown in figure 32. As was the case for the low pressure helium run, the mean free paths are too long to allow a thin shock to form. The forward current sheet structure, which was due to the shock in the higher density runs, is absent here.

Table 3 contains the important characteristics for the hydrogen runs. The velocity U is that of the \dot{B}_0 peak trajectory. For most cases, where the shock is out front, U is less than the snowplow speed u_0 , which in turn, is less than the shock speed. This is to be expected, since the main portion of the accumulated mass is contained between the shock and the \dot{B}_0 peak. It is difficult to

calculate the conductivity σ_o behind the shock, since the shock's influence on the conductivity destroys the original similarity. However, a minimum conductivity can be calculated ignoring the factor $(1 - \bar{u}/\eta)$ in equation (37). The true conductivity is somewhat larger than this fictitious conductivity, which is denoted by the symbol σ_o' . However, to divide σ_o' by $(1 - \bar{u}/\eta)$ gives a larger conductivity than is physically possible, as will be seen in the next section, and indeed, the spreading rate increases rapidly at larger distances, where the similarity solutions once again become applicable.

The values corresponding to σ_o' are listed and also denoted by primes. R_m' and u_e' are too small, while α' is too large. Better estimates will be made in section V. The tendency of σ_o' to decrease with increasing voltage is partially due to the omission of the $(1 - \bar{u}/\eta)$ term. This term is smaller for the $7\frac{1}{2}$ and 9 KV runs, since R_o increases and \bar{u}/η approaches unity. However, the decrease in σ_o' is also a real effect for the cases when a shock has not yet moved out front at $r = 2\frac{1}{2}$ inches. The conductivity is measured between positions 1 and 2 in the current sheet trace, and it is increased by the shock only when the shock is in front of position 1. This is not the case for the 9, $10\frac{1}{2}$, and 12 KV, 700 μ Hg runs. For the 290 μ Hg run, $(1 - \bar{u}/\eta)$ is very small, and thus σ_o' is small. An estimate of the conductivity ahead of the shock is given by the

120 μ Hg run, where no shock is present. This σ_0' must also be considered a minimum value, since there will be some effect due to the plasma compression. The α 's cannot be considered too accurate as a result of both inaccuracies in determining the conductivities and the non-uniformity of the conductivity throughout the current sheet.

The R_m used to determine the position of shock formation should be based on the conductivity before the shock is formed, which is lower than the σ_0' value used to compute R_m' . However, for hydrogen, the r_0 used in computing R_m should be greater than .01 m. These unknown factors make quantitative theoretical predictions impossible. This is the reason that the detailed experimental program was initiated. One main value of the preceding theory and the simple experiments in argon and helium is that they provide a base on which the hydrogen experiments may be interpreted. Without this base it would be impossible to make any sense whatsoever out of the complicated experimental results.

V. INTERPRETATION AND ATOMIC QUANTITIES

5.1 Electron Collisions and Electron Temperature

The resistivity of a plasma arises from the collisions made by the current carrying electrons. It can be defined as $\eta_T = m_e \nu_T / n_e e^2$, where m_e is the electron mass, n_e the electron number density, e the electronic charge, and ν_T is the total electron collision frequency with other particles. The collision frequency can, in turn, be divided into two parts; the first, ν_{ei} , due to Coulomb interactions with ions, and the second, ν_{en} , due to collisions with neutrals. ν_{en} is equal to $n_n \overline{v_e \sigma_{en}}$, where n_n is the neutral number density, v_e is the electron velocity, and σ_{en} is the electron-neutral elastic collision cross section, since the elastic cross section is by far the largest. The electrons will actually be in a Boltzmann distribution, with an average directed velocity in the axial direction, and the average value $\overline{v_e \sigma_{en}}$ should be used, but for the accuracies desired here it is sufficient to consider v_e as the mean square velocity. This will be much larger than the directed, current carrying velocity. Spitzer's formula (Ref. 15) can be used for $\nu_{ei} = n_i \overline{v_e \sigma_{ei}}$, and defining $\eta_T = \eta_c + \eta_n$, the Coulomb contribution is given by,

$$\eta_c = 5.23 \times 10^{-5} \ln \Lambda / u_e^{3/2} = 3.14 \times 10^{-4} / u_e^{3/2} \text{ ohm-m,} \quad (43)$$

where $\ln \Lambda$ is taken as 6, and u_e is given in electron volts. Calling $n = n_i + n_n$, with $\alpha = n_i/n$ (α is the degree of ionization for a monatomic gas assuming that it is singly ionized), the neutral contribution to the resistivity can be written as

$$\eta_n = \left(\frac{1-\alpha}{\alpha}\right) 2.1 \times 10^{-7} \sqrt{u_e \overline{\sigma_{en}}} \text{ ohm-m} \quad (44)$$

$\overline{\sigma_{en}} = \sigma_{en}/10^{-20}$ and σ_{en} is expressed in m^2 . $\overline{\sigma_{en}}$ is plotted in figure 34 for electron collisions with H, H₂, He, and A (Ref. 17). For electron temperatures of about 3 ev, it is obvious that η_n will be significant only for very low degrees of ionization.

For the degrees of ionization attained in argon and helium, and for reasonable values of electron temperature, it is evident that η_n gives a negligible contribution to the total resistivity. Thus, equation (43) can be used alone, with $\eta_T = \eta_c$, to estimate the electron temperature. As seen in the previous tables, this gives reasonable values for u_e of approximately 3 electron volts. Hydrogen, however, since it is diatomic, has a large electron-neutral collision cross section at low energies. For the initially low degrees of ionization and dissociation before the shock, η_n may be as large or larger than η_c . In table 3 α' was calculated as an average degree of ionization, and in all cases is larger than the true value of α .

A good estimate of the value of α in front of the shock can be made from the measured resistivity of the hydrogen plasma for the case in which no shock was formed. For this case η_T is equal to 1.6×10^{-4} ohm/m. For u_e between 0 and 4 ev, $\overline{\sigma_{en}}$ is relatively constant, as seen in figure 34, and equations (43) and (44) can be combined to yield:

$$1.6 \times 10^{-4} = 3.4 \times 10^{-4}/u_e^{3/2} + 2.88 \times 10^{-6} \sqrt{u_e}/\alpha.$$

For $u_e = 2.5$ ev, $\alpha = .056$, and for $u_e = 4$ ev, $\alpha = .048$, so that α must be approximately equal to .05. When electron heating is accounted for, this value agrees with Sorrell's electric field measurements of $\alpha = .044$. If u_e were much less than 2.5 ev the Coulomb collisions would account for the total resistivity and the shock would have no effect on the plasma conductivity. This is contrary to the experimental observations. Values of u_e much above 4 ev are likewise unrealistic; thus, the range chosen above is reasonable.

The equilibrium conditions behind a conventional shock traveling at a velocity u_s are shown in table 4 (Ref. 16). For most cases ionization does not occur, but the degree of dissociation, which at these Mach numbers has a short relaxation time, is high. In fact, since the upstream gas has its enthalpy increased by the arc, it is reasonable to assume that in all cases the gas behind the shock is fully

dissociated. If u_e remains the same, η_c will also be unchanged, but η_n will decrease since $\overline{\sigma_{en}}$ is so much smaller for atomic hydrogen, even though there will be twice as many hydrogen atoms as there were hydrogen molecules. No accurate measurements of the cross sections for elastic electron collisions with hydrogen atoms could be found for low electron energies, but an interpolation of the existing data implies that they are very small. Thus, behind the shock η_n will be ignored in calculating the resistivity. For $u_e = 2.5$ and 4 ev, the corresponding values of η_c are $.88 \times 10^{-4}$ and $.51 \times 10^{-4}$ ohm/m. Since the 6 KV run has a minimum u_e of 3.6 ev, and since the observed effect of the shock on the current sheet shape is large, the larger value of u_e is most likely more accurate. It gives an approximate threefold increase of conductivity across the shock, which, while not large enough to overcome the $(1 - \bar{u}/\eta)$ term and allow separation, is large enough to produce a noticeable effect. The values of σ_o' , R_m' , u_e' , and α' are not good approximations in this complicated case, but along with the estimations used above, better approximations can be made.

In order to ensure separation, the conductivity behind the shock would have to be increased to so large a value that, even accounting for the $(1 - \bar{u}/\eta)$ term, the rate of current sheet spreading would be much less than the ideal shock separating velocity. When real gas effects become important, the density compression ratio across the shock

will increase to much greater values than the ideal 6 (about 12 for u_s between 3 and 7 cm/ μ sec), unless very high shock speeds are achieved. For shock speeds in the range of these experiments, the compression ratio may be as high as 17. Using equation (42), however, C is only about 4 for the 6 and 7½ KV shots where the shock is well in front of the main current sheet; thus, the expansion through the front of the current sheet offers some assistance toward achieving separation. Still, much higher current sheet velocities and electron temperatures than have been attainable in these experiments are necessary. A method of overcoming the tendency of the shock to form in the rear at higher Mach numbers will be discussed in section VI.

5.2 Ion and Neutral Collision Cross Sections

All the analysis in this paper is based on a single-fluid model for an inviscid gas. For these approximations to hold, the mean free paths of the heavy species must be small compared to the widths of the current sheets, which are the order of centimeters thick. In order to determine these mean free paths, and establish the validity of the approximations, a brief investigation of the relevant cross sections is presented in this subsection.

The mean free path for collisions of species a with species b can be approximated:

$$\lambda_{a,b} = 1/n_b \sigma_{ab} = 3/\bar{\sigma}_{ab} \bar{n}_b \text{ cm} \quad (45)$$

where $\bar{n}_b = n_b/3.5 \times 10^{15}$ is the reduced number of particles per cubic centimeter of species b, and σ_{ab} is the appropriate cross section. 3.5×10^{15} particles/cm³ is the number of particles in a gas at room temperature and a pressure of 100 μ Hg. $\lambda_{a,b}$ must be less than 1 mm to be considered small. The important mean free paths to be considered are those involving collisions of neutrals with ions and also those involving self-collisions between the dominant heavy particles. The first type of collision allows the neutrals to be accelerated and the second type enables thin shocks to form and inviscid equations to be used.

For the single-fluid assumptions to hold, the ion-neutral collision cross section must be large enough to prevent ion slip. The lower the degree of ionization, the larger this cross section must be. At high energies (above about 25 ev) the charge exchange mechanism is dominant, and at low energies elastic collisions dominate. The appropriate cross sections are given in table 5 for ions moving at the snowplow velocity with energies u_i .

For argon, the mean free path for a neutral undergoing charge exchange with an ion, $\lambda_{n,i}$, is $.1/\alpha C \bar{n}_0$ cm, where α is the degree of ionization, n_0 is the initial number density, and C is the compressibility factor. Even for the lowest densities where $\bar{n}_0 = 1$, $\lambda_{n,i}$ is of the order of 1 mm. In the front of the current sheet where $C = 1$ and α may be low, the relative velocities are lower and $\overline{\sigma_{ni}}$ is much larger. (Both the elastic and charge exchange cross sections are larger for lower relative energies or velocities.) Thus, $\lambda_{n,i}$ remains small.

The mean free path $\lambda_{n,i}$ for helium and hydrogen is larger than the respective mean free path for argon since the degree of ionization is lower, although $\lambda_{i,n}$ (mean free path for an ion) is shorter. For the higher density runs $\lambda_{n,i}$ is still small, especially behind the shock where C is large. However, for the low density runs (120 μ Hg in hydrogen and 80 μ Hg in helium) where no shock is formed, $\lambda_{n,i}$ is approximately $.15/\alpha C$ cm and for about 15% ioniza-

tion ($\alpha = .15$) there could be considerable ion slip. Even in these limiting cases the low relative velocities in the front of the current sheet, and the compression in the rear, make $\lambda_{n,i}$ considerably smaller. The neutral-neutral mean free path, which governs the shock formation, is the largest important mean free path and its effect is the most serious.

In order to treat the plasma as an ideal fluid, the dominant heavy particle must have a small mean free path for collisions with itself. The ion-ion collision cross sections are calculated in table 5 assuming pure Coulomb collisions, but they will be better approximated by the neutral-neutral cross sections at high energies. The neutral-neutral cross sections in table 5 were calculated from viscosity measurements (Refs. 18 and 19) and have the slight temperature dependence noted.

Argon ions, due to their high energies, have far too small a Coulomb cross section to allow shocks to form, however, the neutral-neutral cross section is reasonable for the 30,000-40,000^oK temperatures expected behind any shocks. For a temperature of 40,000^oK, $\lambda_{n,n} = .25/C\bar{n}_0$ cm, which is less than 1 mm for $C\bar{n}_0 > 2.5$, as it is for all cases in argon. As long as the degree of ionization is not too high, the ions are coupled through the charge exchange collisions, and shocks can form. Even if the degree of ionization is high, the ions will undergo inelastic and other non-Coulomb

type collisions, so that the total cross section will be large enough to allow for shock waves. The experimental results verify the fact that the heavy particle mean free path is small.

In helium the ion-ion and neutral-neutral cross sections are of the same order, but the degree of ionization is low, and neutral-neutral collisions are dominant. For a temperature of $20,000^{\circ}\text{K}$ behind the shock for the $250\ \mu\ \text{Hg}$ run, $\lambda_{n,n} = .25/C\ \text{cm}$, which is less than $1\ \text{mm}$ for $C > 2.5$, verifying the experimental evidence of thin shocks. For the $80\ \mu\ \text{Hg}$ run, however, $\lambda_{n,n}$ is approximately $.8/C\ \text{cm}$, which is too large to form a thin shock in the current sheet. In hydrogen, the degree of ionization is also low, and for the $120\ \mu\ \text{Hg}$ shot $\lambda_{n,n}$ for H_2 is approximately equal to $.2/C\ \text{cm}$. This is small, but is probably not the relevant cross section, since H_2 will be dissociated, and H has a much smaller cross section than H_2 . This accounts for the experimental observation that a thin shock is not present.

More accurate estimations cannot be made as to the validity of the single-fluid assumptions because neither the state of the gas nor the exact relevant cross sections are well known. However, it can be seen that in most cases the assumptions do hold, and when they do not the experimental results show the breakdown quite clearly.

VI. SUMMARY AND CONCLUSIONS

By successive approximations, a model has been developed which successfully accounts for the observed behavior in MHD shock tubes. Considering the driving current sheet as an arbitrary non-diffusive force field qualitatively explained the phenomenon of shock formation within the current sheet and also revealed the Mach number as the important parameter governing the position of the shock. Proceeding from this point, a similarity solution was developed for the cylindrical geometry used in the experiments performed. A second parameter, the magnetic Reynolds number, governing the current sheet thickness and diffusion, was shown to be important. Numerical solutions for different values of the two parameters were shown to be applicable even to experiments where similarity was not strictly observed. Accurate results were obtained for heavy gases where the shock formed in the rear of the current sheet and similarity was not disturbed by the shock. For light gases the similarity solutions correctly predicted where the shocks would form, and other considerations could be used to predict the behavior from that point.

Numerical techniques based on the similarity solutions were developed to estimate the conductivity of the plasma. They were found to be applicable even when the shock destroyed the flow similarity (for finite breakdown widths),

as long as the shock did not affect the plasma conductivity. By considering the simple monatomic gases argon and helium where this was so, and examining the collision cross sections for all gases treated, the more complicated behavior of diatomic hydrogen could be accounted for. The insensitivity of the shock position to the exact current distribution in the similarity solutions enabled one to extend the similarity solutions to predict the behavior of flows where the finite initial breakdown width of the current sheet (or the rapid diffusion in the central portion of the inverse pinch where the conductivity is not proportional to $1/r$) destroyed similarity.

Shocks have the possibility of separating from the current sheet only when they are formed near the front, so that the gas swept up is accumulated behind the shock. It is then necessary to increase the conductivity behind the shock to such a degree that the shock will separate faster than the current sheet can diffuse. Increasing the current sheet speed, or using a heavier gas to increase the shock strength has the adverse effect of causing the shock to form further to the rear in the current sheet. This results in the gas being accelerated and compressed isentropically in front of the shock.

At lower current sheet speeds, the temperatures needed to achieve the desired conductivities are so high that

preionization has no appreciable effect. Preheating the gas tends to cause the shock to form in front, but then the shock is weaker and the final temperature lower than it would be behind a shock propagating at the same velocity into a cold gas.

One method that has been proposed to achieve separation is to initiate a current sheet in the hot gas behind a shock wave in a conventional shock tube, thus increasing the original shock's speed. However, the temperatures behind conventional shocks are not high enough to prevent a rapid spreading of the current sheet, and, if the current sheet were not built up slowly, a second shock would form within it and prevent the desired acceleration of the conventional shock. A better method would be to tailor the initial discharge in an inverse pinch type device so that the current sheet would start at a low velocity and, once a shock was formed in front, the current could be greatly increased to achieve the desired high velocities and Mach numbers without causing the shock to form in the rear. These kinds of tailored current profiles could be achieved by transmission line distributions of capacitors and inductors.

The possibilities of this type of tailored acceleration were investigated in the inverse pinch used in this experiment by first firing the preionization bank at a low voltage and then firing the main bank a short time later,

at a higher voltage, after a shock had formed in front. If the voltages on the two banks differed by too much, a second shock formed, as it would in the experiment described above. However, a continuously increasing drive current would eliminate this effect. Figure 33 shows the trajectory of a current sheet produced by discharging the preionization bank at 6 KV into hydrogen at a pressure of $700 \mu \text{ Hg}$ with the main bank at $7\frac{1}{2}$ KV discharged $1.4 \mu \text{ sec}$ later. For all the shots comprising this run, no tendency whatsoever was noticed for a shock to form further to the rear than is shown, as was the case when the main bank was fired alone at $7\frac{1}{2}$ KV.

This idea was not pursued further because the small size of the inverse pinch does not allow observations to be carried out for times which are long enough for separation to be observed. This is due to the large compression behind high speed shocks, which decreases the ideal separation distance between the shock and a solid piston. A tailored current sheet can be used in MAST type devices where the necessary lengths of the order of several meters have been achieved (Ref. 20), but instabilities due to the lack of hydromagnetic stability may then defeat one's purpose. The best solution may be some inverse pinch type configuration which channels all the energy into a wedge shaped section.

Using the knowledge developed here about the workings

of MHD accelerators, and about the structure of the current sheet and resultant flow, some possible experiments may be attempted even for the incompletely separated shocks produced in hydrogen and helium. One such experiment planned for the future will be performed at the low densities where the mean free paths are such as to prevent ordinary shocks from forming. The addition of an axial magnetic field, while not producing a thin MHD structure, will yield a small Larmor radius for the ions. Deviations from the expected structure will be sought in an attempt to observe the theoretically predicted collision free shocks. Pressure probes can be used to measure any shock structure that appears due to the addition of the axial field. For higher density cases, when an ordinary shock is present, the arc heating of the heavy particles is negligible and real gas effects behind the shock can be investigated under conditions of initially high electron concentrations. However, the expansion region due to the non-solid piston will make such observations difficult. Any further effort in such devices should first be devoted to producing truly separated shocks with uniform regions of reasonable length between the shock and the front of the current sheet.

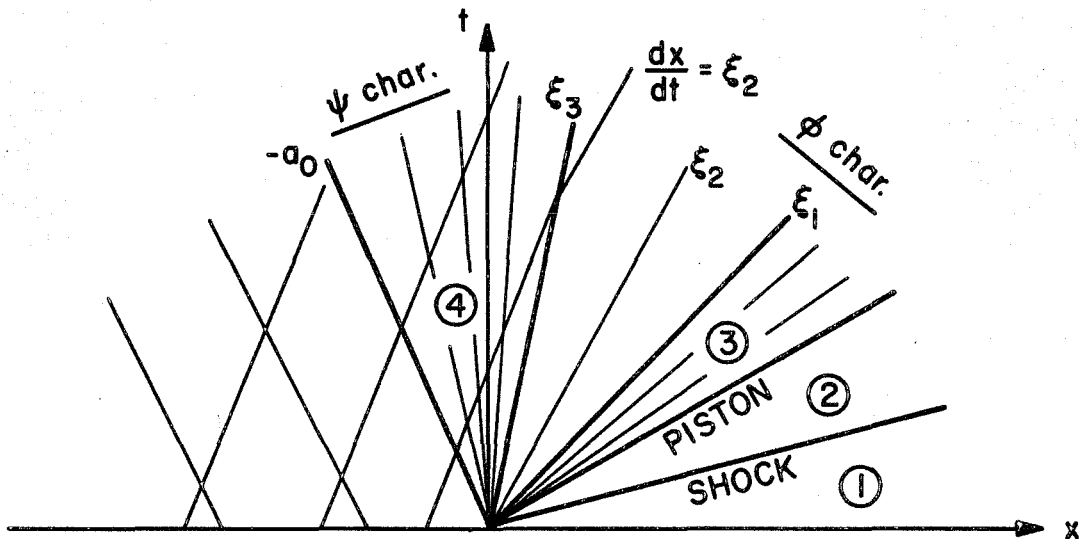
The main value of the work presented here is the revelation of the correct procedure to be followed to achieve separation. Light gases offer the best possibility for success due to the lower resultant Mach numbers at the

high magnetic Reynolds numbers necessary to keep the current sheet thin. The experiments performed in helium and hydrogen, plus the fluid mechanical arguments used in the analysis, should be useful in the design of future experiments. The success of a basically MHD approach to such a complicated plasma problem is especially notable, and future experimenters might do well to consider the use of a macroscopic description in cases where the more general equations of plasma physics are too difficult to solve.

APPENDIX A

FULL DELTA FUNCTION FORCE SOLUTION

The diagram below shows both the ψ and ϕ characteristics behind the concentrated piston in laboratory



coordinates. Besides the normal expansion region (4) in the ψ characteristics there is also an expansion region (3) in the ϕ characteristics. If the flow consists solely of simple wave regions as shown, these two expansion fans must not overlap. This condition will be shown to be related to the escape speed of the gas.

Calling $n = 2/(\gamma - 1)$ and $\xi = dx/dt = x/t$, the conditions in the expansion fan behind the piston in region (3) can be written:

$$u - na = Q = u_3 - na_3$$

$$u + na = \text{const. on } u + a = \xi$$

where Q is given by the solutions of subsection 2.3. Thus:

$$a = (\xi - Q)/(n + 1) \tag{1}$$

$$u = (n\xi + Q)/(n + 1) .$$

In the expansion fan of region (4):

$$u + na = na_0$$

$$u - na = \text{const. on } u - a = \xi$$

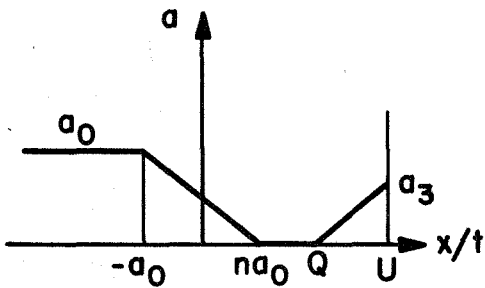
or,

$$a = (na_0 - \xi)/(n + 1) \tag{2}$$

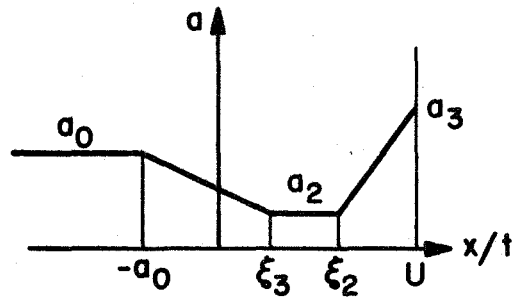
$$u = n(\xi + a_0)/(n + 1) .$$

There are two possible cases, governed by whether a does or does not go to zero between regions (3) and (4). Since the cases being considered have pistons moving faster than the escape speed, a solid piston produces a vacuum and a is zero. The amount of leakage through a non-solid piston determines whether the gas that has leaked through completely fills the vacuum region. The two possible cases are shown on the next page.

For case 1, a equals zero before ξ reaches ξ_2 and Q must be greater than ξ_2 as shown by equations (1), (ξ decreases as the characteristics become more vertical). The expansion fan in region (4) extends forward to $\xi = \xi_3$



Case 1



Case 2

where $a = 0$. Using equations (2), $\xi_3 = na_0$ and $u = na_0$.

$$\xi_2 = (u + a) \text{ at } \xi_3 = na_0$$

$$\xi_1 = Q \text{ for } a = 0$$

Thus, for case 1 Q must be greater than na_0 .

If Q is less than na_0 , a never goes to zero. Then:

$$\begin{aligned} \xi_2 = \xi_1 &= (u + a) \text{ at } \xi_3 \\ &= (2na_0 + (n - 1)\xi_3)/(n + 1) \end{aligned} \quad (3)$$

Equating a from equations (2) at ξ_3 to a from equations

(1) at ξ_2 :

$$(na_0 - \xi_3)/(n + 1) = (\xi_2 - Q)/(n + 1) \quad (4)$$

Equations (3) and (4) can be used to solve for ξ_2 and ξ_3 .

$$\xi_3 = (n + 1)Q/n + (n - 1)a_0/2 \quad (5)$$

$$\xi_2 = (n - 1)Q/2n + (n + 1)a_0/2$$

The condition $Q < na_0$ insures that $\xi_2 > \xi_3$ as shown. The other condition that must be satisfied is that $\xi_2 < U$.

When ξ_2 is greater than U the above simple wave argument breaks down, so the criteria governing this occurrence must be found. The maximum possible value of Q occurs for the case of no leakage, and $a_3 = 0$, $u_3 = U$, and $Q = U$. Thus, the maximum value of ξ_2 is,

$$\xi_{2\max} = (n - 1)U/2n + (n + 1)a_0/2 \quad .$$

The condition $\xi_{2\max} > U$ can be expressed:

$$(n + 1)a_0/2 > (n + 1)U/2n$$

$$U < na_0 = 2a_0/(\gamma - 1) \quad .$$

$2a_0/(\gamma - 1)$ is the escape speed of the gas and, if the piston moves at a velocity less than this escape velocity, the simple wave solutions may not hold. However, this is a maximum stipulation and for $Q < U$ it can be relaxed. Equation (5) determines the exact requirement for the simple wave solution to hold.

APPENDIX B CONCENTRATED FORCE PROGRAM

```

DIMENSION F(50)
1 READ (5,10) RMO, GAMMA, KK
10 FORMAT (2F10.5,15)
GAMMA1 = GAMMA - 1.
GAMMA2 = GAMMA + 1.
GAMMA3 = GAMMA1/GAMMA2
GG = GAMMA2/4.
UMAX = GG + SQRT(GG**2 + (1./RMO**2))
UMAXO = GG + SQRT(GG**2 + 1.)
FMAX = (2./GAMMA2)*UMAX**2 - GAMMA3/(GAMMA*RMO**2)
FMAXO = UMAXO + (1./GAMMA)
WRITE (6,11) RMO, GAMMA, UMAX, FMAX
11 FORMAT (1H1,5X,4HMO =,F10.5,5X,7HGAMMA =,F10.5,5X,6HUMAX =,F10.5,
1 5X,6HFMAX =,F10.5)
WRITE (6,12)
12 FORMAT (//// 10X,2HSU,9X,1HF,8X,2HP1,8X,2HU1,8X,2HA1,8X,2HP2,
1 8X,2HU2,8X,2HA2,9X,1HX //)
DELTA = (UMAX - 1.)/25.
DO 2 I = 1,25
RI = I
SU = 1. + DELTA*(RI - 1.)
RMS = (SU*RMO)**2
P = (GAMMA2*RMS)/(GAMMA1*RMS + 2.)
U = SU*(1. - (1./P))
A = SQRT(1. + (2.*GAMMA3/GAMMA2)*(GAMMA + (1./RMS))*(RMS-1.))/RMO
EE = 2./GAMMA2
UP = 1. - U
S = (A/UP)**EE
RK = (A/UP)**2/GAMMA
FP = RK*(1. - (1./S)**GAMMA) + 1. - S
F(I) = FP*P*UP**2
EF = GAMMA1/2.
U2 = 1. - S*UP
P2 = P/S
A2 = A/S**EF
X = 1. - A2/GAMMA3
IF (X .LT. 0.) X = (GAMMA1/2.)*X
2 WRITE (6,13) SU,F(I),P,U,A,P2,U2,A2,X
13 FORMAT (5X,9F10.5)
SU = UMAX
RMS = (SU*RMO)**2
P = (GAMMA2*RMS)/(GAMMA1*RMS + 2.)
U = SU*(1. - (1./P))
A = SQRT(1. + (2.*GAMMA3/GAMMA2)*(GAMMA + (1./RMS))*(RMS-1.))/RMO
P2 = 0.
U2 = 1.
A2 = 0.
X = 1.
WRITE (6,13) SU,FMAX,P,U,A,P2,U2,A2,X
JJ = 25.*(UMAXO/UMAX) + 1.
DO 3 I = 25,JJ
3 F(I) = FMAX
CALL CPlot (F,JJ,JJ,DD,FMAXO,0.,KK)
IF (KK .NE. 0) GO TO 4
GO TO 1
4 WRITE (6,14) UMAXO,FMAXO
14 FORMAT (// 5X,7HUMAXO =,F10.5,5X,7HFMAXO =,F10.5)
STOP
END

```

APPENDIX C CYLINDRICAL SIMILARITY SOLUTION PROGRAM

```

DIMENSION SETA(200), SUI(200), SP(200), SBE(200), SHEN(200),
1SCUR(200), SPHI(200), SEMASS(200), BPROBE(200), SCOOP(200) ,
2ETAM(25), UM(25), PM(25), BEM(25), BENM(25), EMASSM(25)
100 READ(5,11) RMOLD, RMNEW, GAMMA, IPIT
11 FORMAT (3F10.5, 15)
RM = RMOLD
IF (RM .LT. 0.) STOP
GAMMA1 = GAMMA - 1.
GAMMA2 = GAMMA + 1.
GAMMA3 = GAMMA2/GAMMA1
READ (5,10) RKAPPA, CO, ETA
10 FORMAT (2E10.4, F5.2)
BEN = (RKAPPA/(ETA)**2)/(EXP(ETA*RM))
BE = BEN/2.
U = 0.0
P = 1.0
READ (5,12) DELT, NUM
12 FORMAT (F10.5, 15)
DELT10 = 10.*DELT

```

```

C
C SET INITIAL VALUES TO ZERO

```

```

I = 1
IT = 1
EMASS = 0.
KUCHK = 0
KOOP = 0
ALPHA = 0.
CONST = CO*GAMMA
PMAX = 0.
MOCK = 0.
M = 0
ETAS = 0.
BPMAX = 0.
CURMAX = 0.
IMED = 0
MM = 0
LWRITE = 0
KDOPE = 0
MAX = 0
SPRE = 1000.

```

```

C
C START COMPUTATIONS

```

```

WRITE (6,13) RMOLD,RKAPPA, CO, BEN, ETA
13 FORMAT (1H1,1X,6HRMOLD=,F6.2,5X,6HKAPPA=,E12.4,5X,3HCO=,E12.4,
1 5X,4HBEN=,E12.4,8H AT ETA=,F5.2)
WRITE (6,18)
18 FORMAT ( / 3X,3HETA,9X,1HP,11X,1HU,10X,2HBE,10X,3HBEN,
1 9X,3HCUR,9X,3HPHI,8X,4HCOOP,9X,2HAB,7X,1HI //)
1 K = 0
2 TEMP1 = U/ETA
A = 1. - TEMP1
IF (A .GE. .001) GO TO 72
IF (MOCK .EQ. 0) GO TO 37
GO TO 30
72 PHI = P*A
CUR = (ETA*BEN) - BE
IF (CUR .LT. 0.) CUR = 0.
ETASQ = ETA**2
AB = (CONST*(P**GAMMA))/(ETASQ*PHI*A)

```

ABP = 1. - AB

C

C FIND POINT FROM WHERE ON UN IS NEGATIVE AFTER SHOCK

```

IF (KUCHK .NE. 0) GO TO 8
IF (K .NE. 0 .AND. KDOPE .NE. 1) GO TO 8
RKS = GAMMA2/(GAMMA2 - 2.*ABP)
RKPS = 1. - (1./RKS)
U2S = RKPS*ETA + (U/RKS)
ABS2 = (GAMMA2 + GAMMA1*ABP)/(GAMMA2 - 2.*ABP)
GOOP = ABS2*U2S - (BE*CUR)/(PHI*ETA)
IF (GOOP .GT. 0.) GO TO 8
KDOPE = KDOPE + 1
IF (KDOPE .EQ. 2) GO TO 50
IMED = I-2
ETA = SETA(IMED)
P = SP(IMED)
U = SU(IMED)
BE = SBE(IMED)
BEN = SBEN(IMED)
EMASS = SEMASS(IMED)
I = IMED
GO TO 5
50 KMED = K-1
KUCHK = 1
IK = NUM*IMED + KMED
WRITE (6,17)IMED, KMED
17 FORMAT (// 10X,5HIMED=,I4,5X,5HKMED=,I4 //)

```

C

C TEST FOR SHOCK AND PUT IN SHOCK VALUES AT K = KK

```

8 IF (KOOP.EQ.0) GO TO 36
IF (K .NE. KK) GO TO 36
RK = GAMMA2/(GAMMA2 - 2.*ABP)
RKP = 1. - (1./RK)
RMOCKN = 1./SQRT(AB)
PRESS = RKP*P*((ETA-U)**2) + CO*(P**GAMMA)
P = RK*P
U = RKP*ETA + (U/RK)
CONST = GAMMA*(PRESS/(P**GAMMA))
ALPHA = 1.5*GAMMA1
RMS = RMNEW/(P**ALPHA)
KOOP = 0
ETAS = ETA
GO TO 2

```

C

C TEST FOR SINGULARITY BEFORE AND AFTER SHOCK

```

36 IF (MOCK .EQ. 0 .OR. KOOP .EQ. 1) GO TO 35
IF (IABP .LT. -DEL10) GO TO 32
WRITE (6,16) CONST, PRESS
16 FORMAT (// 5X,6HCONST=,E11.4,5X,6HPRESS=,E11.6)
MOCK = 2
GO TO 30
35 IF (IABP .GT. DEL10) GO TO 32
37 LWRITE = 1
IF (MOCK .EQ. 0) GO TO 51
WRITE (6,19) MOCK
69 FORMAT (//// 5X,5HMOCK=,I5)
STOP
51 MOCK = 3
KABP = K - 2
IABP = I - 1
IKMAX = NUM*IABP + KABP

```

```

KSPACE = IKMAX - IK
NSAVE = (KSPACE/NUM) + 5
DO 57 N = 1, NSAVE
  IB = IABP + 1 - N
  ETAM(N) = SETA(IB)
  PM(N) = SP(IB)
  UM(N) = SU(IB)
  BEM(N) = SBE(IB)
  BENM(N) = SBEN(IB)
57 EMASSM(N) = SEMASS(IB)
RKSPAC = KSPACE + NUM
RKSP3 = (RKSPAC)**.333333
JJ2 = RKSP3
JJ1 = JJ2**2
MAX = JJ2 + 5
MAX1 = 2*(JJ2+1)
JJ = JJ1
I = I - 1
ETA = ETA + DELT
U = U - UN*DELT
P = P - PN*DELT
AB = (CONST*(P**GAMMA1))/((ETA**2)*((1.-(U/ETA))**2))
ABP = 1. - AB
WRITE (6,15) IABP, KABP, ABP
15 FORMAT (// 5X,5HIABP=,I4,5X,5HKABP=,I4,5X,4HABP=,E11.4 //)
IF (KUCHK .NE. 0) GO TO 30
WRITE (6,68) KUCHK
68 FORMAT (//// 5X, 6HKUCHK=,I5)
STOP
32 UN = ((BE*CUR)/(PHI*ETASQ) - AB*TEMP1)/ABP
PN = (P*(UN-TEMP1))/(A*ETA)
IF (MOCK .EQ. 0 .OR. KOOP .EQ. 1) GO TO 33
RM = RMS*(P**ALPHA)
33 CURN = ETA*RM*(A*BEN - ((BE*UN)/ETA)) + (ALPHA*PN*CUR)/(P*ETA)
BENN = (CURN + 2.*BEN)/ETA
ETA = ETA - DELT
U = U + DELT*UN
P = P + DELT*PN
PHI = P*(1.-(U/ETA))
BE = BE + DELT*BEN
BEN = BEN + DELT*BENN
CUR = CUR + CURN*DELT
EMASS = EMASS + 6.2828 *ETA*DELT*(P-1.)
K = K + 1
IF (K .LT. NUM) GO TO 2
IF (ETA .GT. 2.) GO TO 1
34 IF (LWRITE .NE. 0) GO TO 5
COOP = 1. - (EMASS/(3.1414 *ETASQ))
WRITE (6,14) ETA, P, U, BE, BEN, CUR, PHI, COOP, AB, I
14 FORMAT (F9.4, 8E12.4, I5)
SETA(I) = ETA
SP(I) = P
SU(I) = U
SBE(I) = BE
SBEN(I) = BEN
SCUR(I) = CUR
SPHI(I) = PHI
SEMASS(I) = EMASS
SCOOP(I) = COOP
5 I = I + 1
IF (I .GE. 200) GO TO 100

```

GO TO 1

C

C START OF PLOTTING AND CHANGING SHOCK POSITION

```

30 PRESS = (CONST/GAMMA)*(P**GAMMA)
VEL = SQRT((1.414 *ETA)/SQRT(BE**2 + 2.*PRESS))
WRITE (6,19) ETAS, ETA, PRESS, VEL, EMASS, RMOCKN
19 FORMAT (1 4X,5HETAS=,F7.4,4X,4HETA=,F6.3,4X,9HPRESSURE=,F7.4,4X,
1 9HVELOCITY=,F7.4,1X,8HSNOWPLOW,4X,6HEMASS=,F7.4,4X,
2 9HMOCK NO.=,F9.4)
COOP = 1. - (EMASS/(3.1414 *ETASQ))
WRITE (6,66) ETA, P, U, BE, BEN, CUR, PHI, COOP, AB, I, K
66 FORMAT (F9.4, 8E12.4, 2I5 ///)
CONST = CO*GAMMA
ALPHA = 0.
RM = RMOLD
IF (LWRITE .EQ. 0) GO TO 56
IF (MOCK .NE. 1) GO TO 90
IF (PRE .GE. SPRE) GO TO 91
SPRE = PRE
MM = 0
GO TO 90
91 MM = MM + 1
IF (MM .LT. 2) GO TO 90
IKMAX = IKMAX - JJ*(M-3)
M = 0
MAX = MAX1
IF (JJ .EQ. 1) LWRITE = 0
IF (JJ .EQ. JJ2) JJ = 1
IF (JJ .EQ. JJ1) JJ = JJ2
MM = 0
SPRE = 1000.
90 M = M+1
IF (M .LE. MAX) GO TO 92
WRITE (6,64) MAX
64 FORMAT (// 5X,4HMAX=,I4)
STOP
92 IKNEW = IKMAX - JJ*M
I = IKNEW/NUM
KK = IKNEW - NUM*I
IB = IABP + 1 - I
ETA = ETAM(IB)
P = PM(IB)
U = UM(IB)
BE = BEM(IB)
BEN = BENM(IB)
EMASS = EMASSM(IB)
KOOP = 1
MOCK = 1
GO TO 5

```

C

C PLOT CURVES IF IPIT GREATER THAN 0

```

56 I = I-1
PMAX = 0.
DO 40 L = IT, I
BPROBE(L) = ((SETA(L)**2)*SBEN(L))
BPMAX = AMAX1(BPMAX, BPROBE(L))
PMAX = AMAX1(PMAX, SP(L))
40 CURMAX = AMAX1(CURMAX, SCUR(L))
PROBE = ETASQ*BEN
BPMAX = AMAX1(BPMAX, PROBE)
BEFIN = SORT(BE**2 + 2.*PRESS)

```

```
II = I + 1
COOP = 1. - (EMASS/13.1414 * (ETA**2))
DO 41 L = II, 200
SP(L) = 0.
SBE(L) = BEFIN
SCUR(L) = CUR
BPROBE(L) = PROBE
41 SCOOP(L) = COOP
CURMAX = AMAX1(CURMAX, SCUR(200))
IF (IPIT .LE. 0) GO TO 100
CALL CPLOT (SP,200,200,DD,PMAX,0.,0)
CALL CPLOT (SBE,200,200,DD,BEFIN,0.,0)
CALL CPLOT (SCUR,200,200,DD,CURMAX,0.,0)
CALL CPLOT (BPROBE,200,200,DD,BPMAX,0.,0)
CALL CPLOT (SCOOP,200,200,DD,1.,0.,1)
GO TO 100
END
```

REFERENCES

1. W. Marshall, Proc. Roy. Soc. (London), Series A 233, 367 (1955).
2. R. Gross, Phys. Today 18, 20 (1965).
3. C. Greifinger and J. D. Cole, Phys. Fluids 4, 527 (1961).
4. H. W. Liepmann and G. C. Vlasses, Phys. Fluids 4, 927 (1961).
5. M. J. Lighthill (G. K. Batchelor and R. M. Davies, editors), Surveys in Mechanics (The University Press, Cambridge, 1956), p. 250.
6. F. Y. Sorrell, Ph.D. Thesis, Caltech (1966).
7. G. C. Vlasses, J. Fluid Mech. 16, 82 (1963).
8. G. C. Vlasses, Ph.D. Thesis, Caltech (1963).
9. R. G. Jahn (editor), "Princeton University Report No. 634g", (July, 1966).
10. R. Loveberg, Phys. Fluids (suppl) 7, S57 (1964).
11. B. Miller, Phys. Fluids 10, 9 (1967).
12. A. F. Klein, Ph.D. Thesis, Caltech (1966).
13. T. J. Falk and D. L. Turcotte, Phys. Fluids 5, 1288 (1962).
14. F. Y. Sorrell, Private communication (1966).
15. L. Spitzer, Physics of Fully Ionized Gases (Interscience, New York, 1956).
16. J. Artmann, "Untersuchung des Gleichgewichtszustandes hinter einer starken Stoßwelle in Wasserstoff", Physikalisches Institut der Rheinisch-Westfälischen Technischen Hochschule Aachen PPS 102 (April, 1963).
17. S. C. Brown, Basic Data of Plasma Physics (Press of the Mass. Inst. of Technology, Cambridge, Mass. 1959)
18. J. Jeans, An Introduction to the Kinetic Theory of Gases (The University Press, Cambridge, 1959).

REFERENCES (cont.)

19. I. Amdur and E. A. Mason, *Phys. Fluids* 1 377 (1958).
20. R. M. Patric and E. R. Pugh, *Phys. Fluids* 8, 636 (1965).
21. A. Schlüter (article from a symposium held at Cambridge, England, July 6-11, 1953), Gas Dynamics of Cosmic Clouds (North Holland Publishing Co., Amsterdam, 1955).
22. R. L. Burton, Ph.D. Thesis, Princeton (1966).

R_m	M_o	η_f	η_p	η_s	η_c	M_s	v_s/u_o	u_o/U
3	72.5	1.33	1.0	.88	.85	4.12	.935	.937
3	23.1	1.33	1.0	.90	.81	3.50	.956	.943
4	70.8	1.23	.97	.87	.83	4.50	.942	.914
4	22.4	1.23	.97	.89	.80	4.36	.986	.914
4	7.1	1.23	.97	.96	.74	3.89	1.036	.921
5	68.8	1.17	.96	.86	.82	5.17	.957	.888
5	21.8	1.17	.96	.91	.77	7.77	1.007	.892
5	7.0	1.17	.96	.96	.74	4.64	1.067	.906
6	69.5	1.11	.94	.94	.75	41.12	1.044	.897
6	22.0	1.11	.94	.94	.75	13.70	1.050	.897
6	7.0	1.11	.97	.97	.74	5.27	1.077	.900

Table 1. Summary of eleven computer runs for the conical solution to an inverse pinch under various operating conditions. Notation is shown in figure 5.

Volts (KV)	Pressure (μ Hg)	U (cm/ $\sqrt{\mu}$ sec)	$\frac{M_o}{-}$	$\frac{R_o}{(in)}$	$\frac{\sigma_o}{(mhos/m)}$	$\frac{R_m}{-}$	$\frac{u_e}{(ev)}$	α -
7	100	1.63	51	3.9	1.53×10^4	3.1	2.8	.9
$8\frac{1}{2}$	100	1.77	56	2.2	1.62	3.6	3.0	1.1
10	100	1.98	60	3.6	1.62	4.0	3.0	1.1
10	170	1.69	53	2.0	1.41	3.1	2.7	1.1
12	170	1.85	58	4.4	1.59	3.7	2.9	1.2
14	170	2.15	63	1.4	1.31	3.6	2.6	1.6
14	400	1.76	51	2.1	1.18	2.6	2.4	1.1
10	125	1.80	57	4.0	1.50	3.4	2.8	1.0
10*	125	1.96	57	4.7	1.50	3.7	2.8	1.1
10	500	1.27	40	1.5	1.06	1.7	2.2	.6
10*	500	1.56	40	3.9	1.33	2.6	2.6	.7

* Preionized

Table 2. Argon Experimental Data

Volts (KV)	Pressure (μ Hg)	U (cm/ $\sqrt{\mu}$ sec)	$\frac{M_o}{-}$	$\frac{R_o}{(in)}$	$\frac{\sigma_o'}{(mhos/m)}$	$\frac{R_m'}{-}$	$\frac{u_e'}{(ev)}$	$\frac{\alpha'}{-}$
6	700	1.72	15	3.8	2.18×10^4	4.8	3.6	.05
$7\frac{1}{2}$	700	1.89	17	8.1	1.57	3.8	2.9	.07
9	700	2.24	18	9.7	1.68	4.8	3.0	.08
$10\frac{1}{2}$	700	2.59	20	4.2	1.23	4.1	2.5	.13
12	700	2.62	21	1.0	1.02	3.4	2.2	.14
9	290	2.67	23	4.6	1.19	4.1	2.4	.15
9	120	3.38	28	7.4	0.63	2.7	1.6	.27
$6-7\frac{1}{2}$	700	1.72	-	6.6	1.82	4.0	3.2	.06

Table 3. Hydrogen Experimental Data

<u>Pressure</u> (μ Hg)	u_s (cm/ μ sec)	<u>Temp.</u> ($^{\circ}$ K)	M_s	β ($^{\circ}$ dissoc.)	α ($^{\circ}$ ioniz.)
700	2.09	3780	15.8	.71	0
700	2.45	4710	18.6	.96	0
700	2.32	4240	17.6	.92	0
700	2.43	4710	18.4	.95	0
700	2.70	7600	20.5	1	0
700	2.84	8760	21.5	1	0
700	2.13	3900	16.1	.73	0
290	3.26	10500	24.7	1	.08
120	(4)	12100	30.3	1	.24

Table 4. Equilibrium Conditions Behind a Shock in Hydrogen

Collision Cross Sections $\bar{\sigma}_{ab}$ ($\text{cm}^2 \times 10^{16}$)

u_0 ($\text{cm}/\mu\text{sec}$)	u_i (eV)	<u>Ion- Neutral</u>	<u>Ion- Ion</u>	<u>Neutral- Neutral</u>
1.6	54	31	.35	- .24
Argon		charge exchange		$17.1 \times \left(\frac{T}{10000^\circ\text{K}}\right)$
2.4	120	29	.08	
2.6	14	31	4.5	-3.4
Helium		total		$5.75 \times \left(\frac{T}{10000^\circ\text{K}}\right)$
3.5	25	24	1.5	
2.0	2	50	250^+	- .2
Hydrogen	H	H ⁺ -H elastic	H ⁺ -H ⁺	$14.6 \times \left(\frac{T}{3000^\circ\text{K}}\right)$
3.8	8	20	20	

Table 5. Ion and Neutral Collision Cross Sections

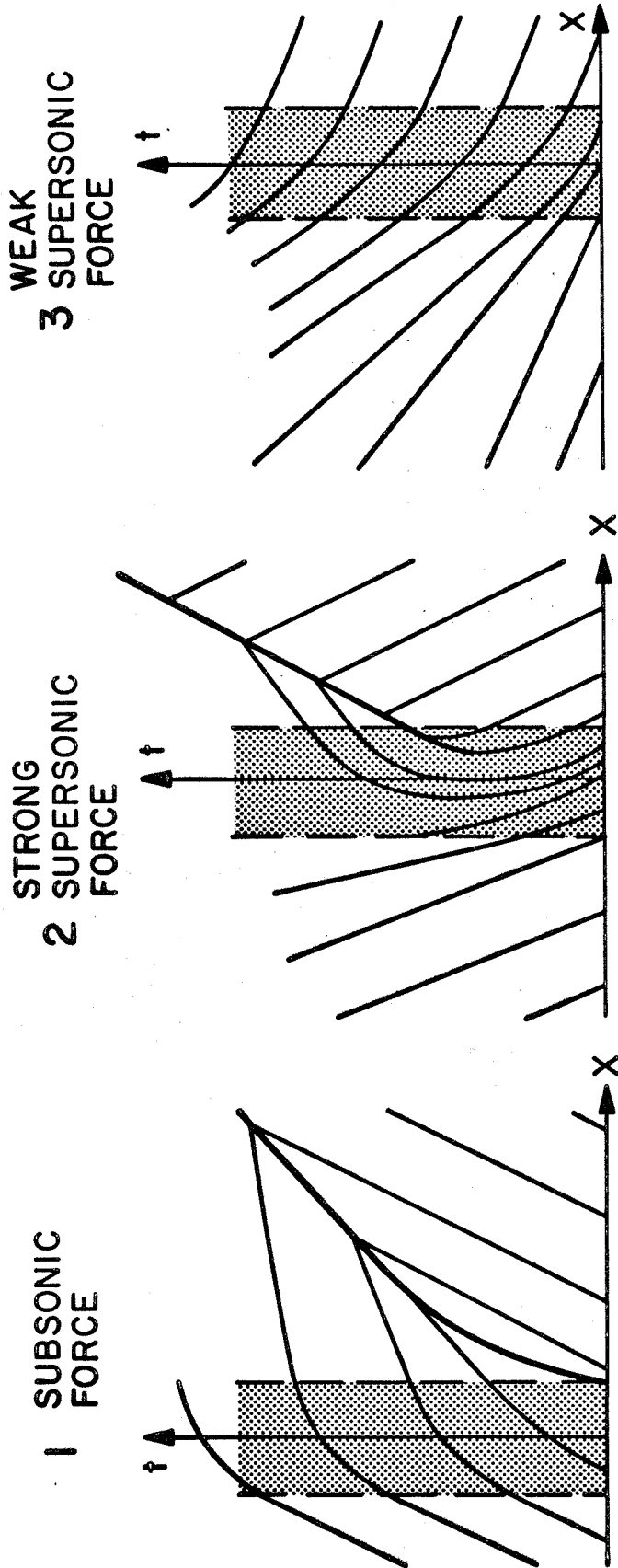


Figure 1. Characteristic diagrams for a fluid driven by a distributed force located in the shaded region. The resultant shocks are shown by a heavy line

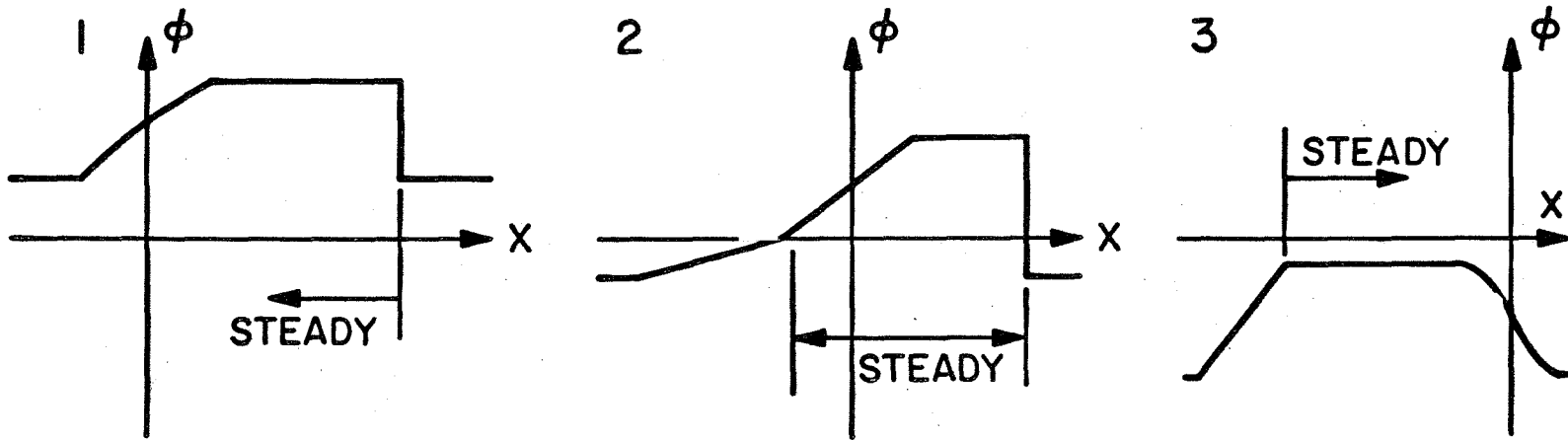


Figure 2. Disturbance profiles corresponding to the characteristic diagrams for large times. The steady flow regions are indicated.

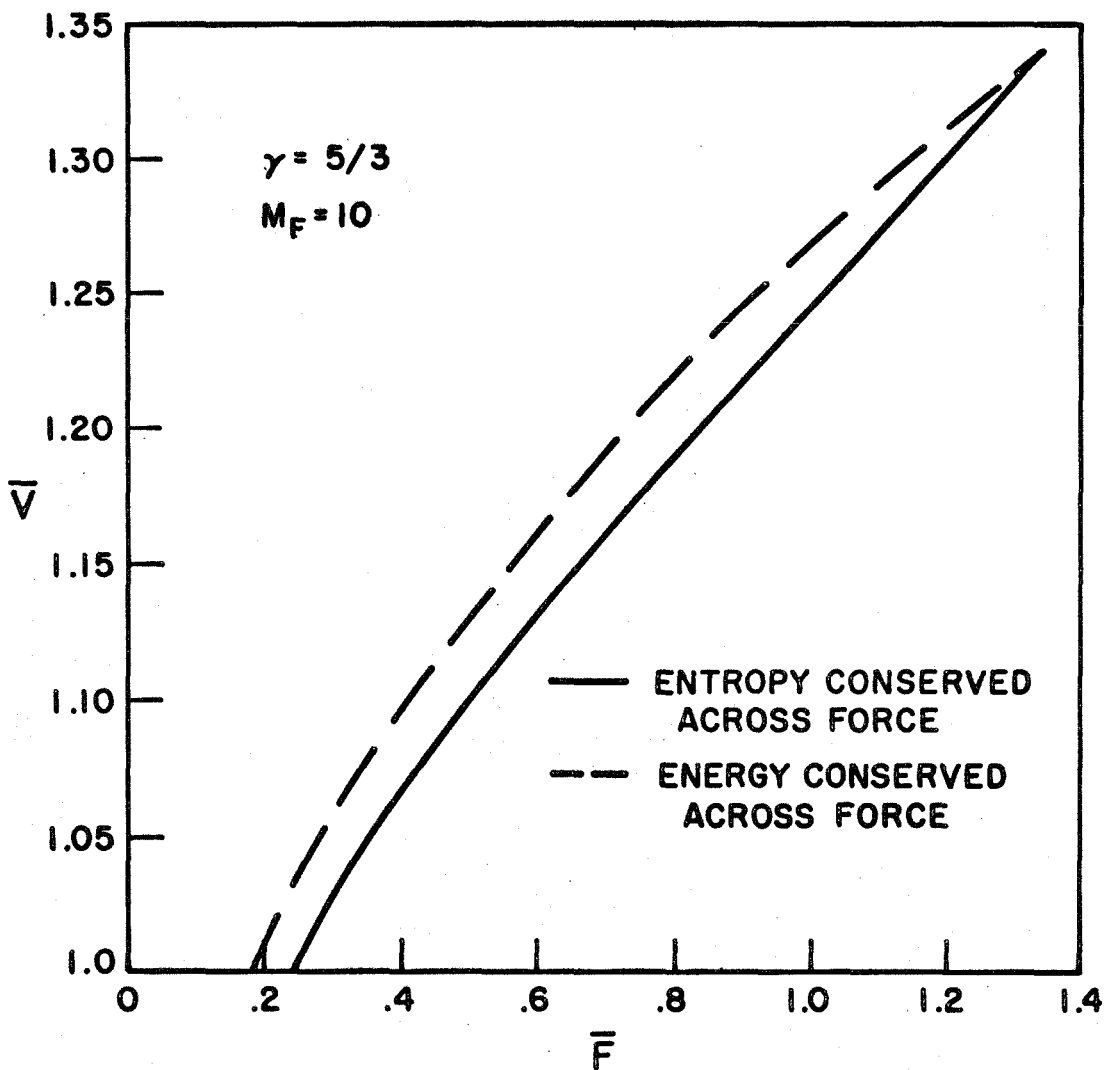


Figure 3. Force diagram for the normalized shock velocity as a function of the normalized piston force for a piston which is moving at Mach 10 with respect to the gas upstream of the shock.

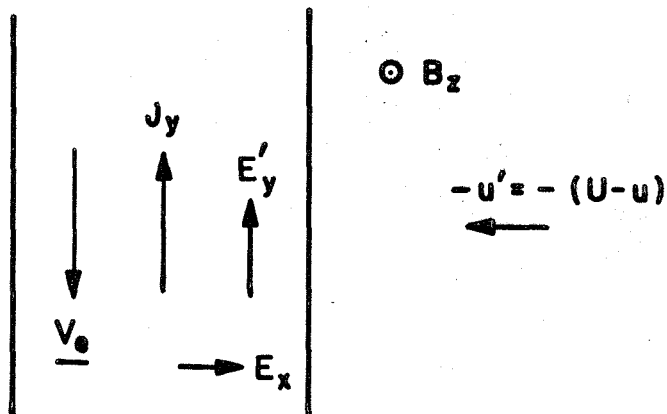
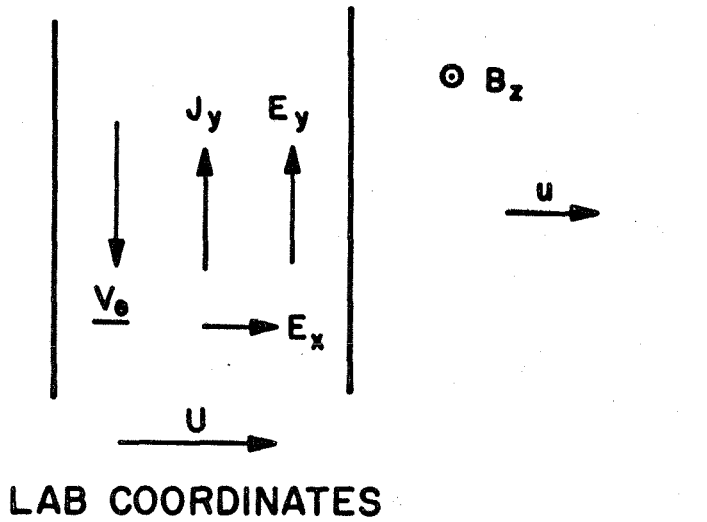


Figure 4. One dimensional simplified model of a current sheet with field and flow quantities indicated in both laboratory and current sheet coordinates.

$$E_y = E'_y + UB_z$$

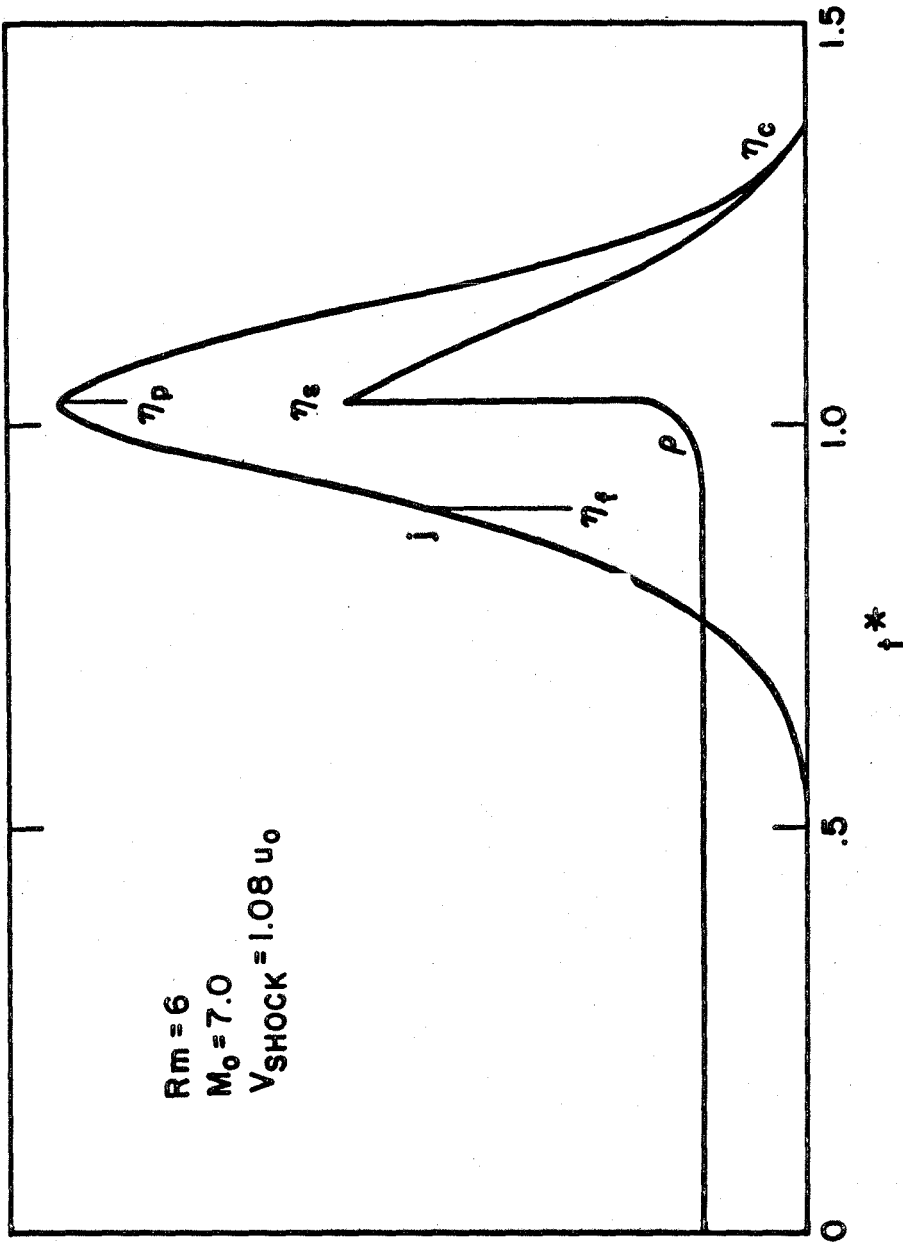


Figure 5. Current and density distributions in an inverse pinch as obtained from a conical solution, as a function of time $t^* = Ut/r = 1/\eta$. Small Mach number.

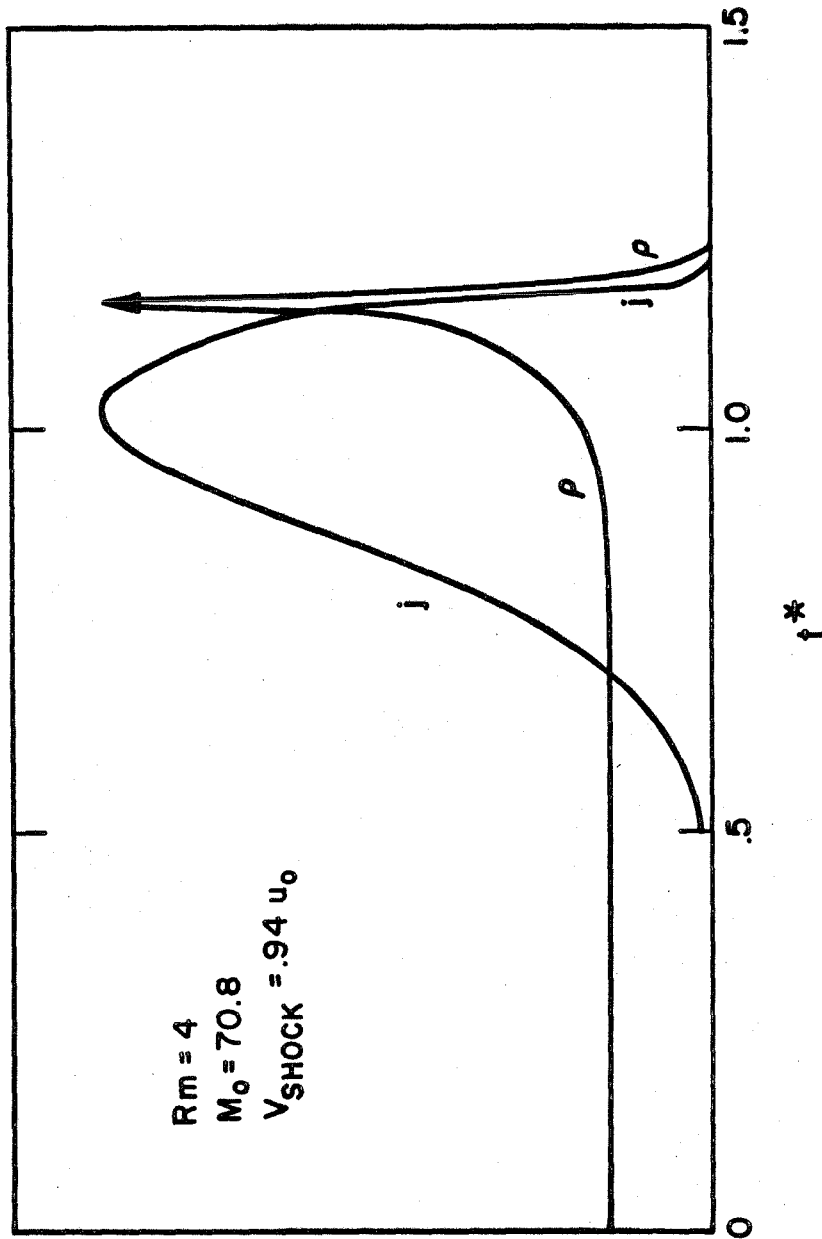
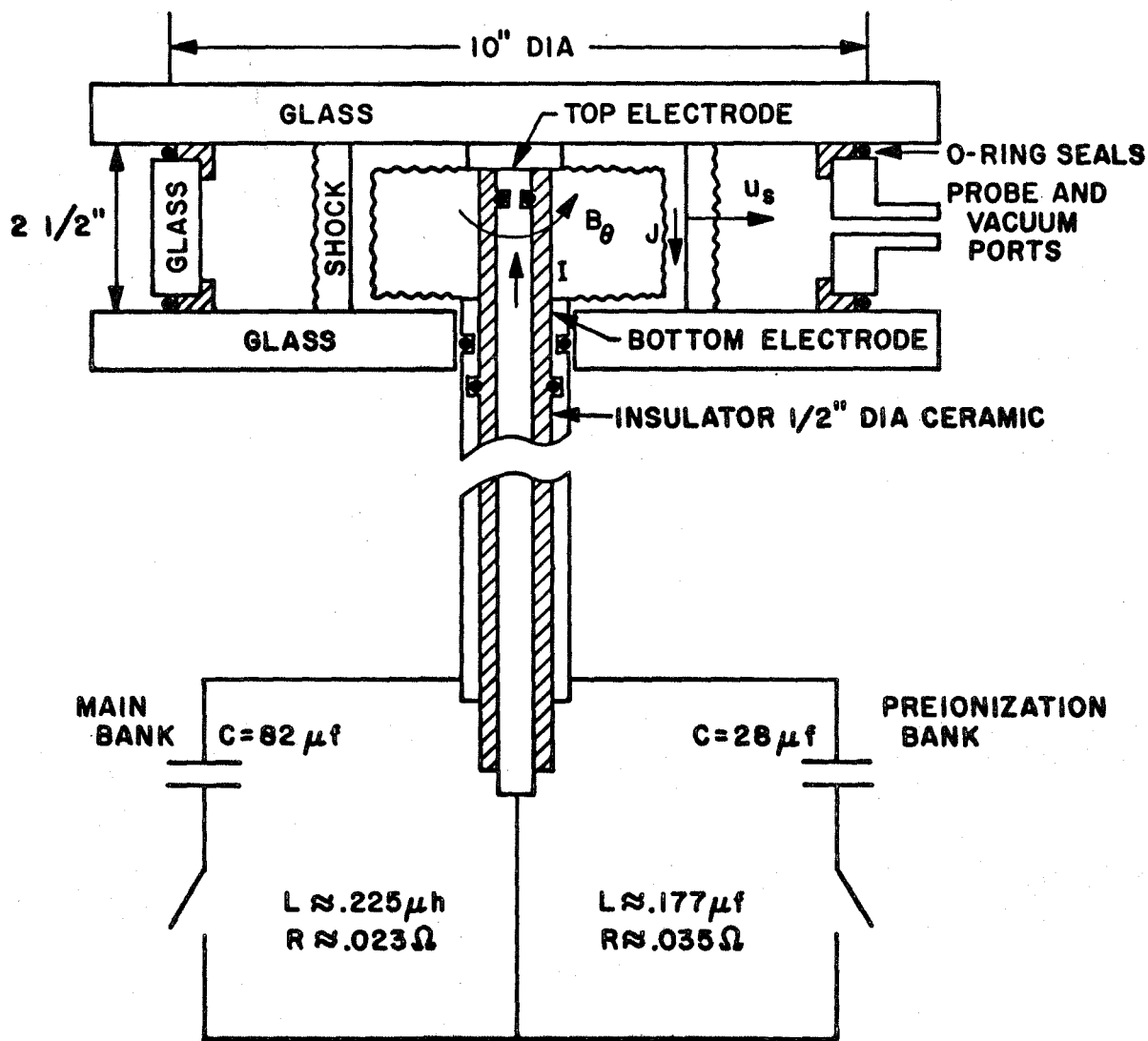


Figure 6. Current and density distributions in an inverse pinch as obtained from a conical solution, as a function of time $t^* = Ut/r = 1/\eta$. Large Mach number.



APPROX: 1/3 SCALE

Figure 7. Inverse pinch geometry including circuit parameters.

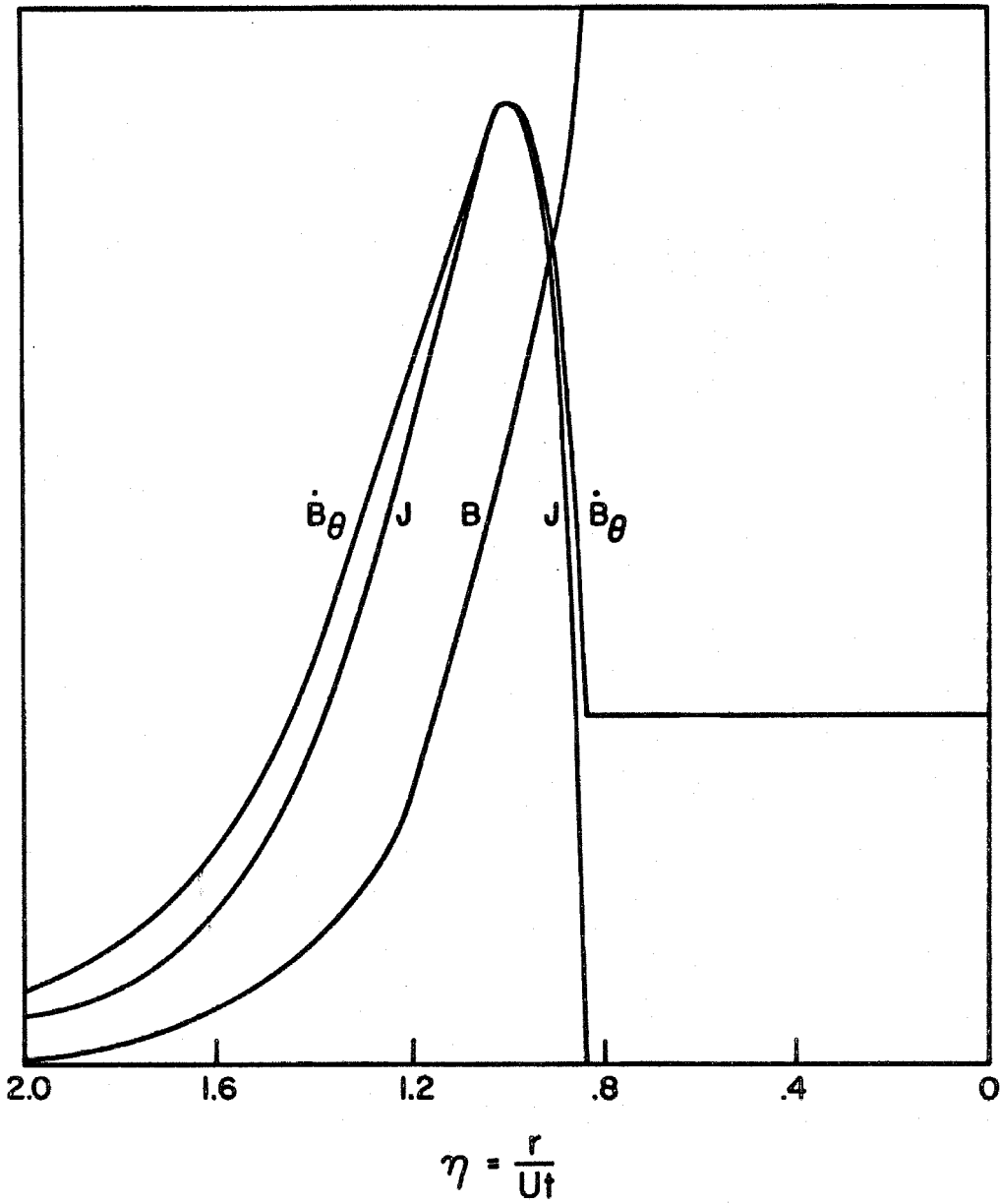


Figure 8. Similarity solution showing the relationships between J , B_θ , and B .

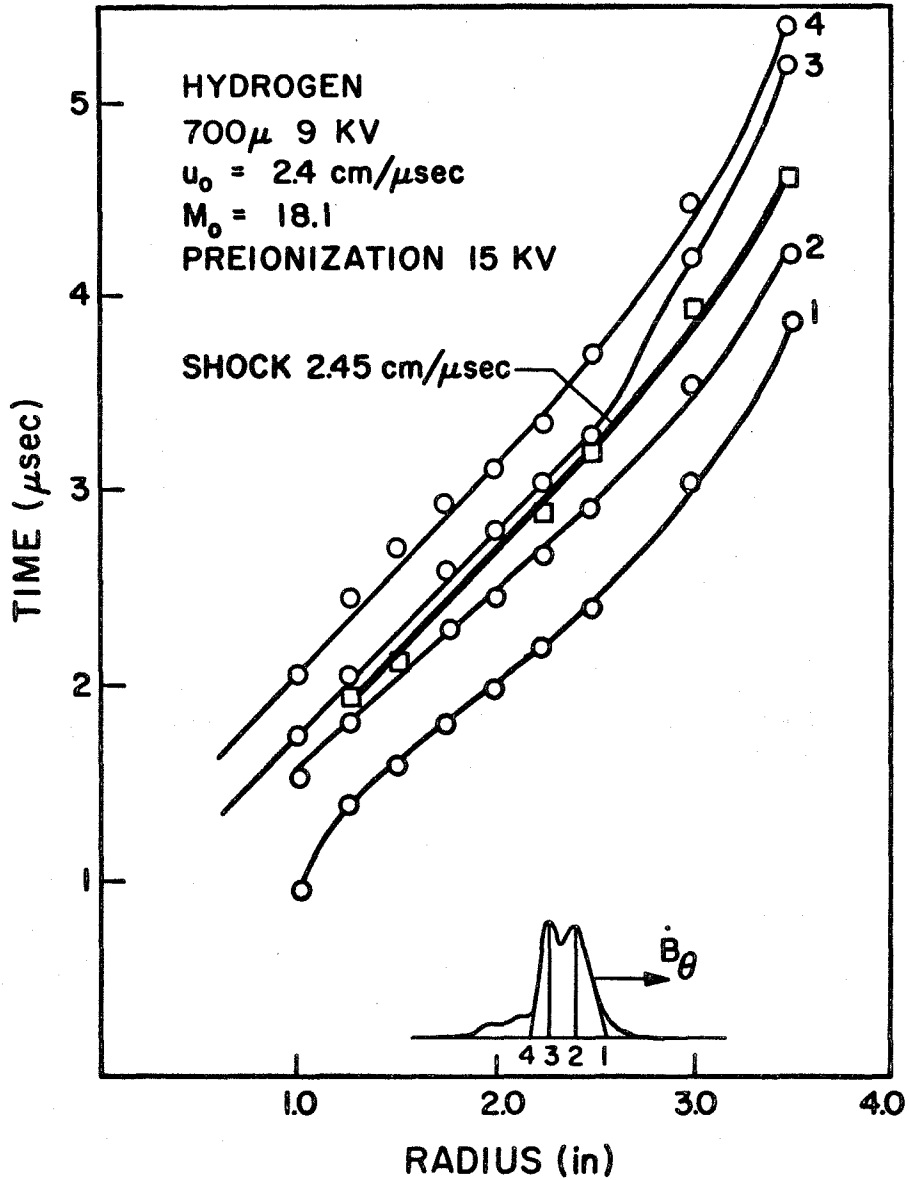


Figure 9. Shock and current sheet trajectories for pre-ionized hydrogen.

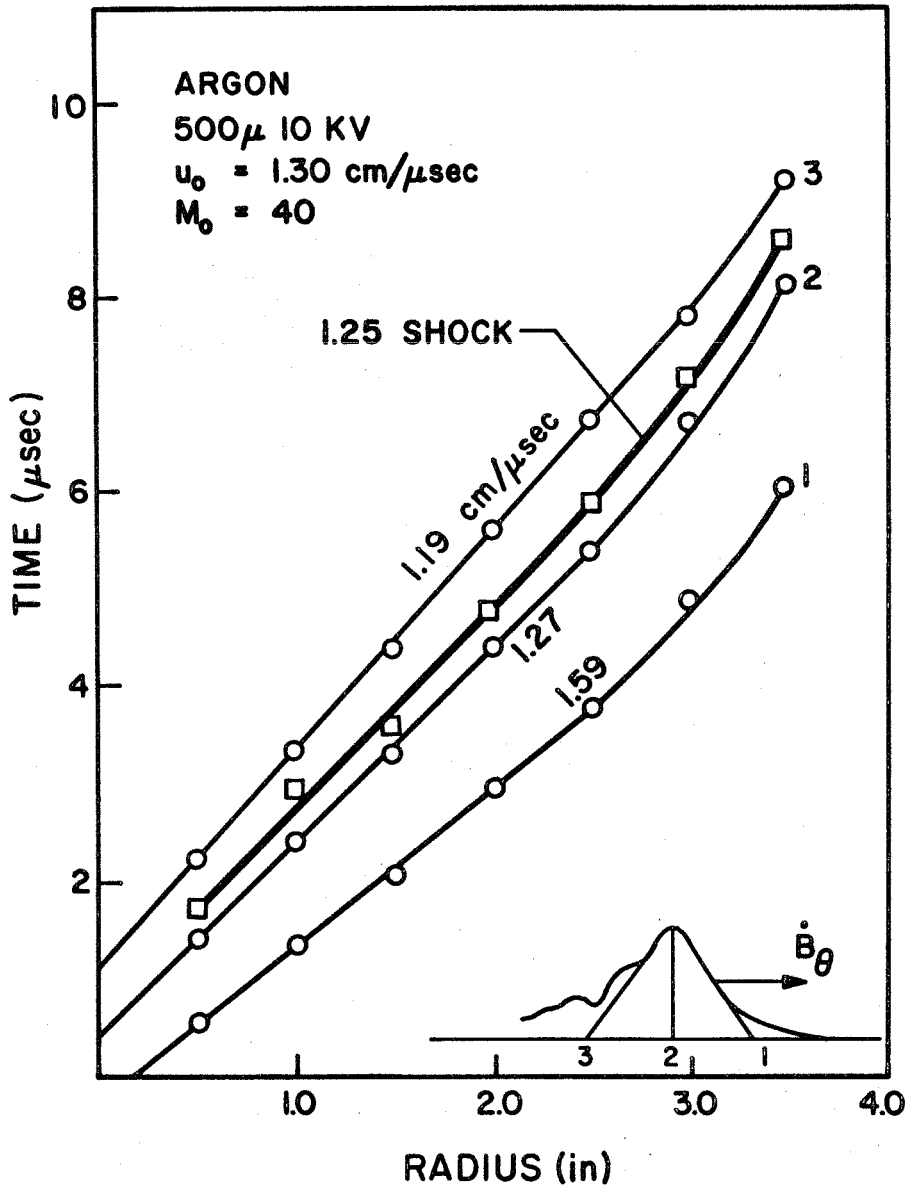


Figure 10. Shock and current sheet trajectories for argon. 500 μ Hg 10 KV.

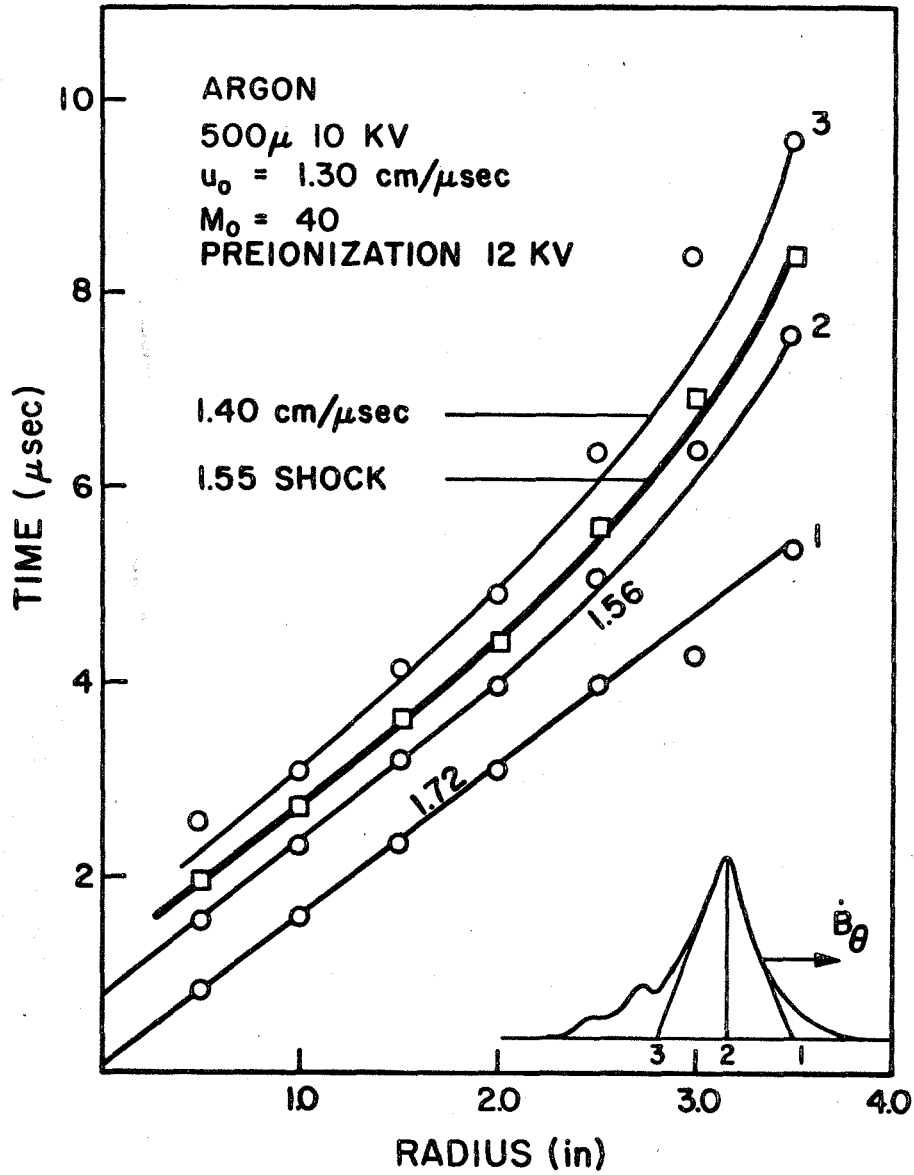


Figure 11. Shock and current sheet trajectories for pre-ionized argon. 500 μ Hg 10 KV.

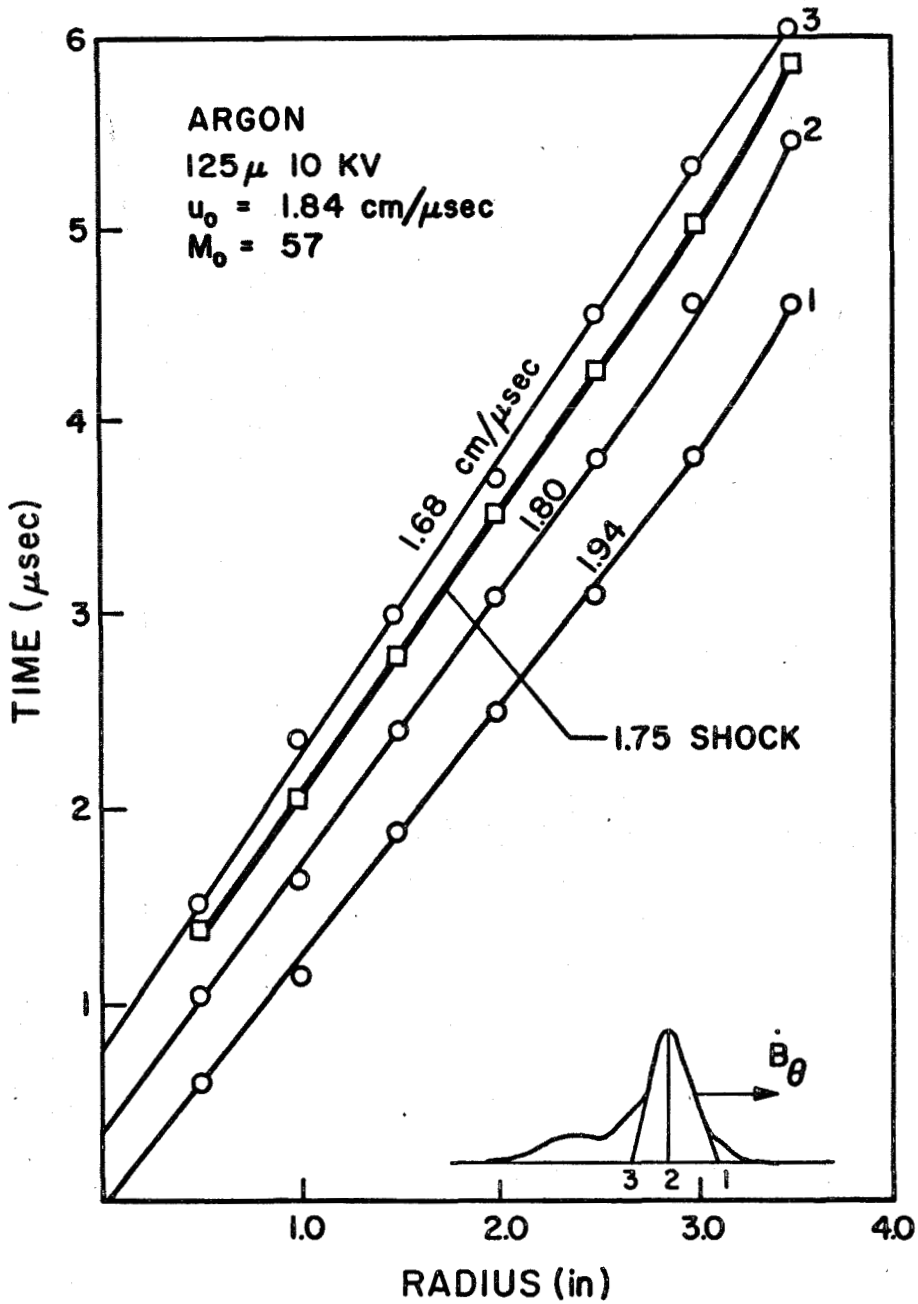


Figure 12. Shock and current sheet trajectories for argon. 125μ Hg 10 KV.

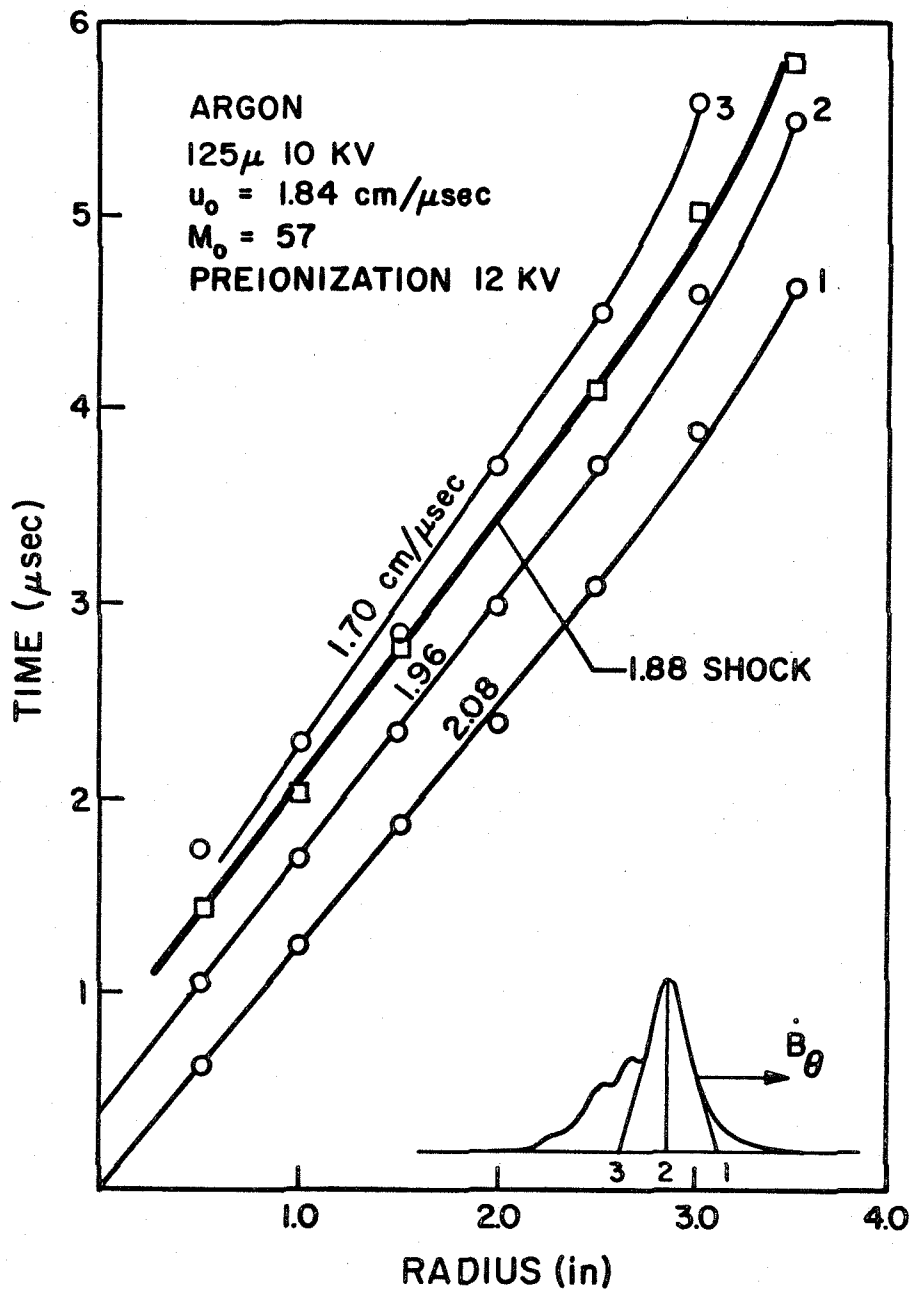


Figure 13. Shock and current sheet trajectories for pre-ionized argon. 125μ Hg 10 KV.

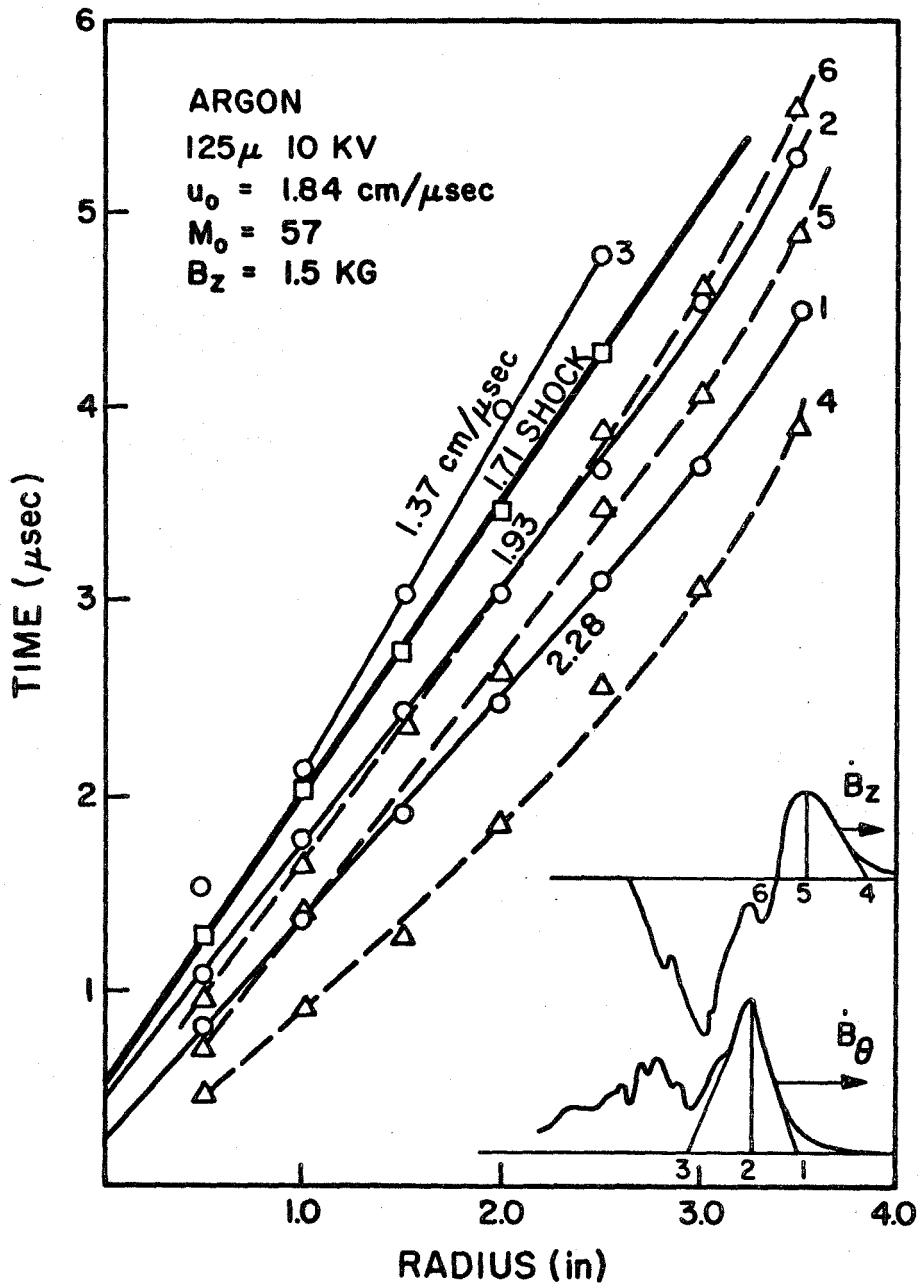
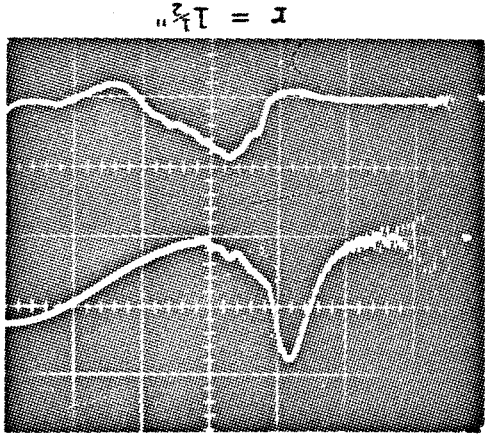
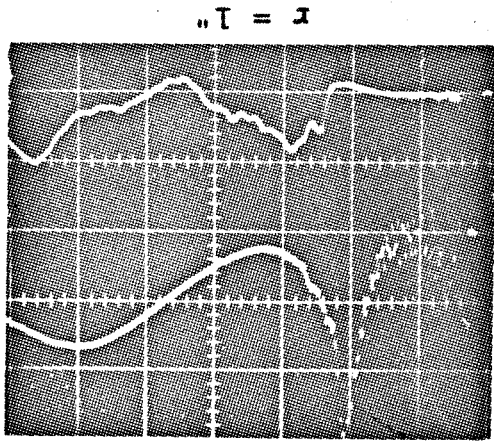


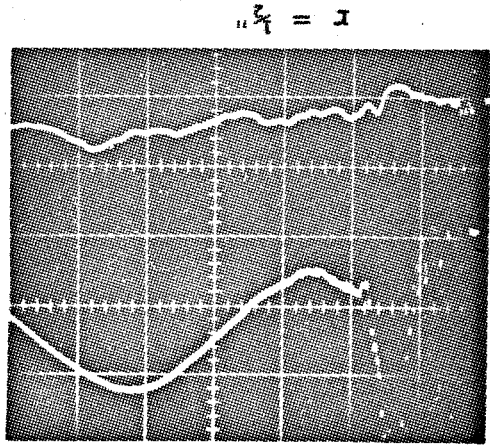
Figure 14. Shock, current sheet, and B_z profiles for argon.



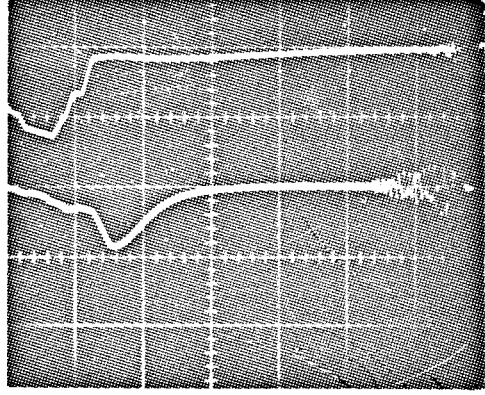
$r = 1\frac{1}{2}''$



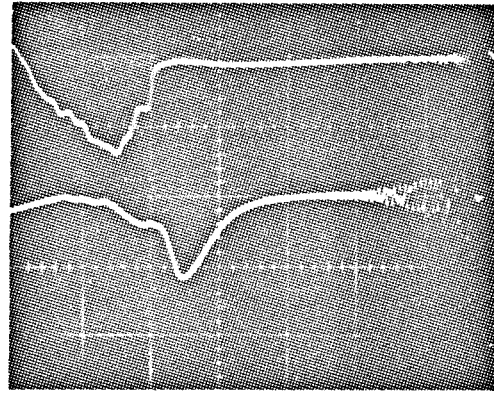
$r = 1''$



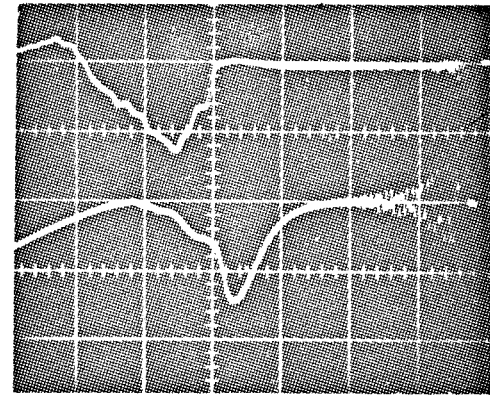
$r = \frac{3}{4}''$



$r = 3''$



$r = 2\frac{1}{2}''$



$r = 2''$

Figure 15. Actual oscilloscope traces for argon at 175 μ and 8 $\frac{1}{2}$ KV. Time scale, 1 μ sec/div. Upper trace B_z, 1 v/div. Lower trace pressure, .5 v/cm.

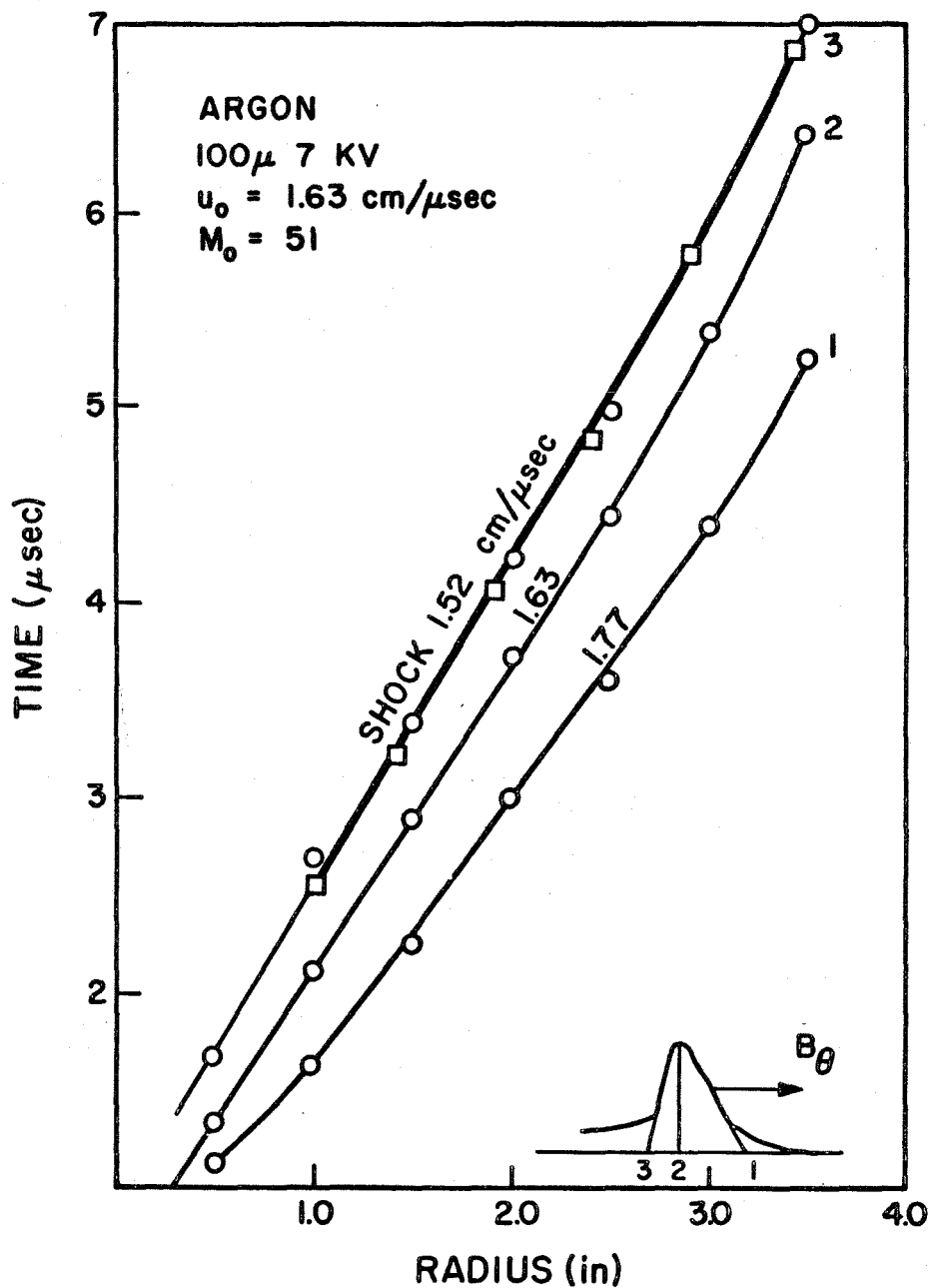


Figure 16. Shock and current sheet trajectories for argon. $100\ \mu$ Hg 7 KV.

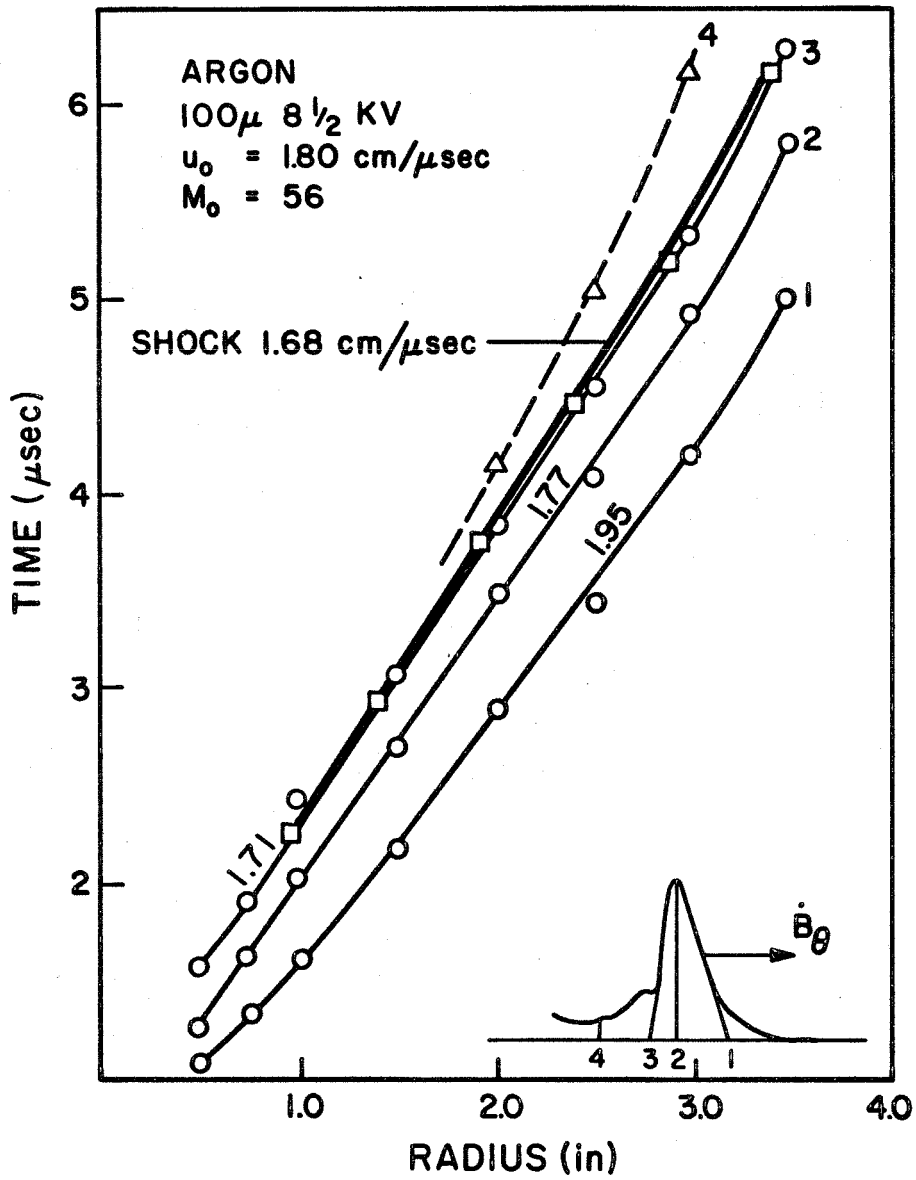


Figure 17. Shock and current sheet trajectories for argon. 100μ Hg $8\frac{1}{2}$ KV.

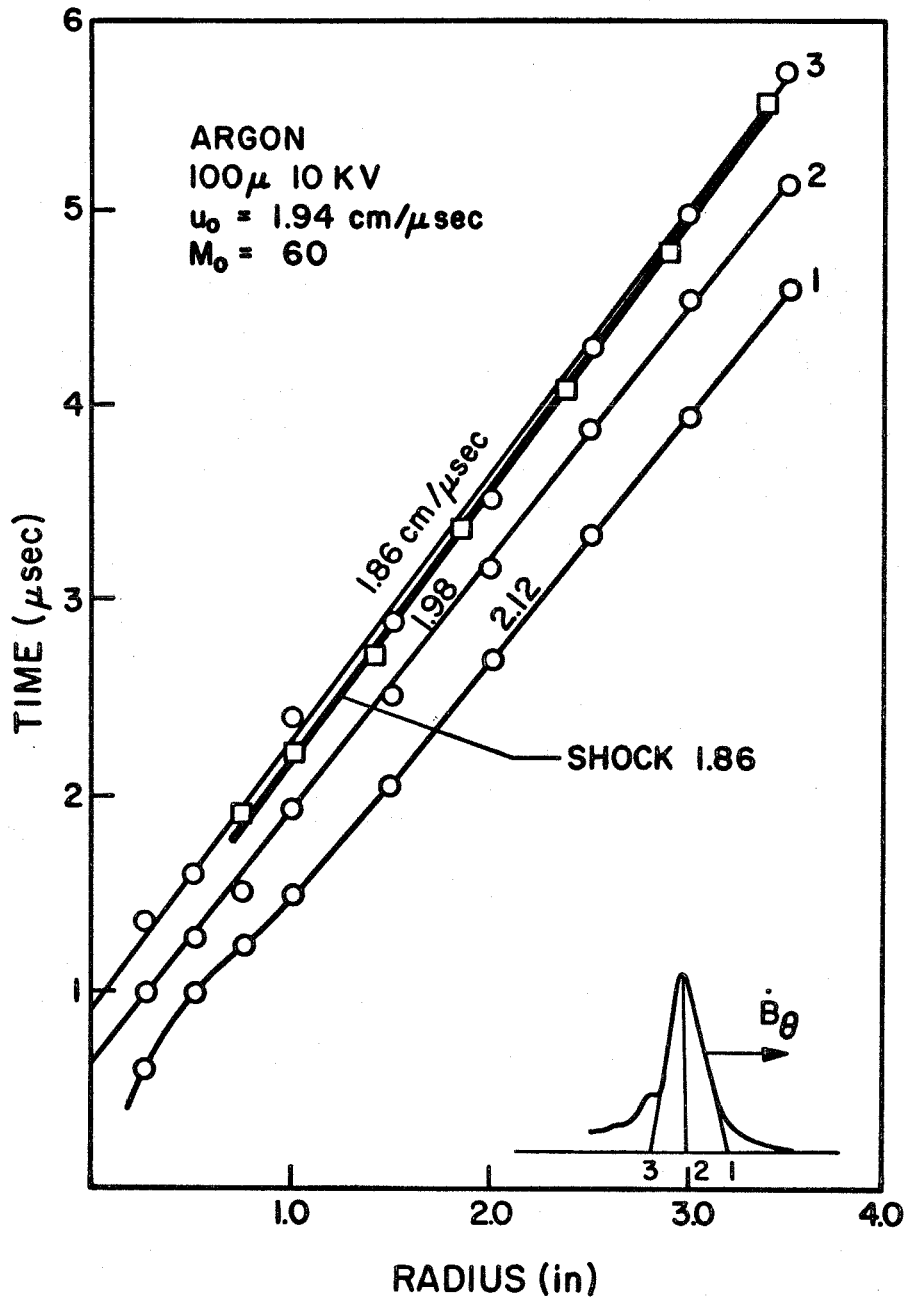


Figure 18. Shock and current sheet trajectories for argon. 100μ Hg 10 KV.

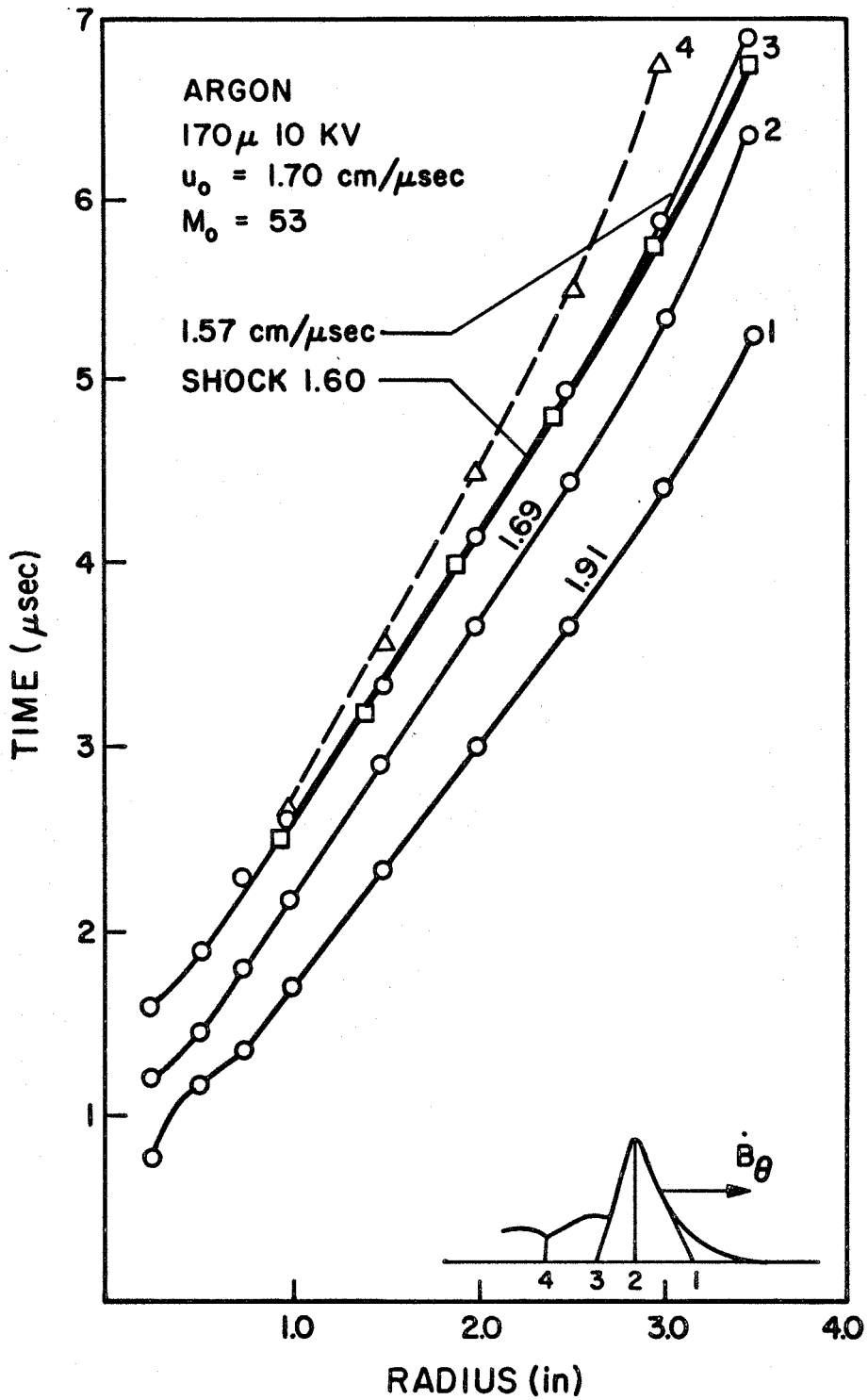


Figure 19. Shock and current sheet trajectories for argon. 170 μ Hg 10 KV.

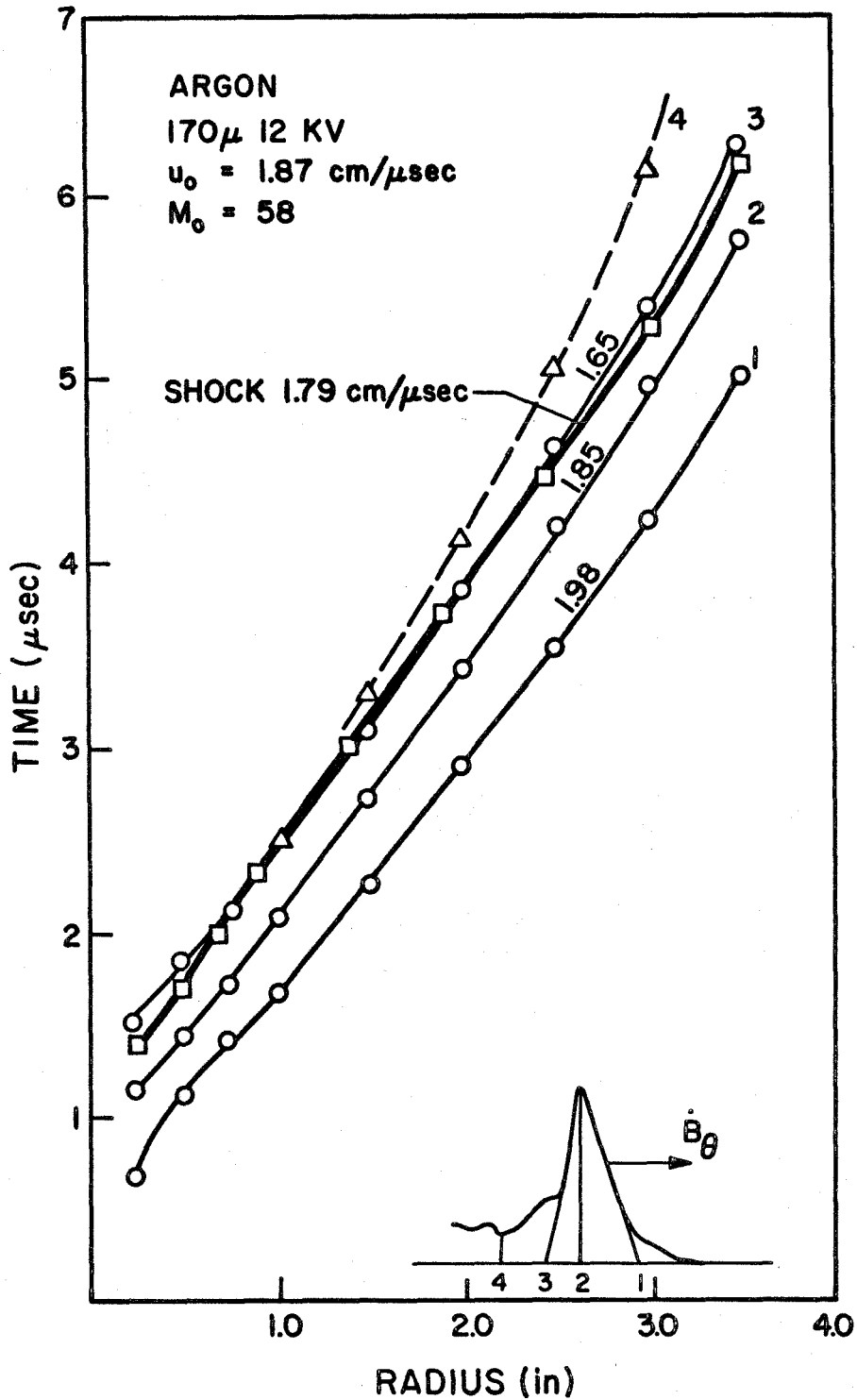


Figure 20. Shock and current sheet trajectories for argon. 170μ Hg 12 KV.

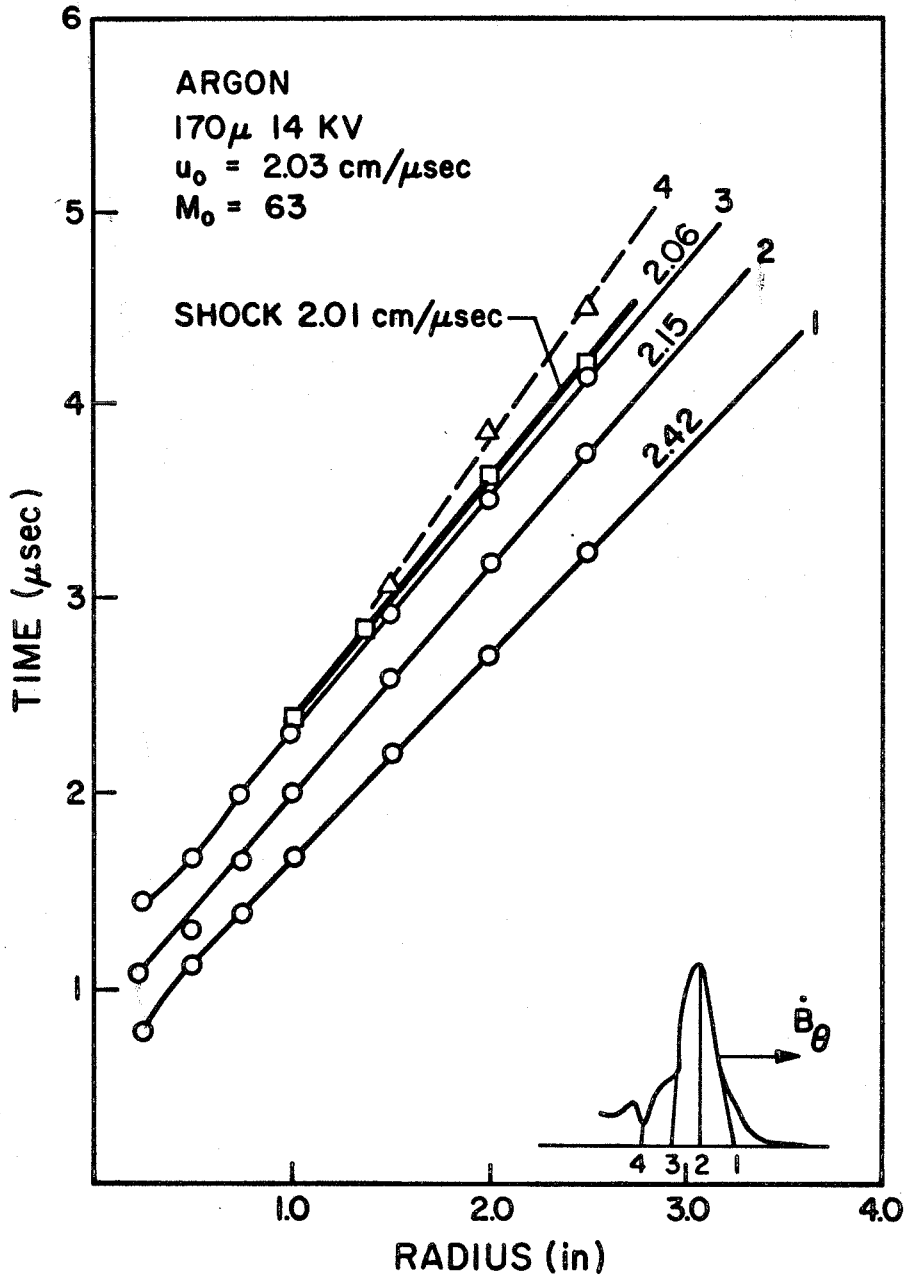


Figure 21. Shock and current sheet trajectories for argon. 170μ Hg 14 KV.

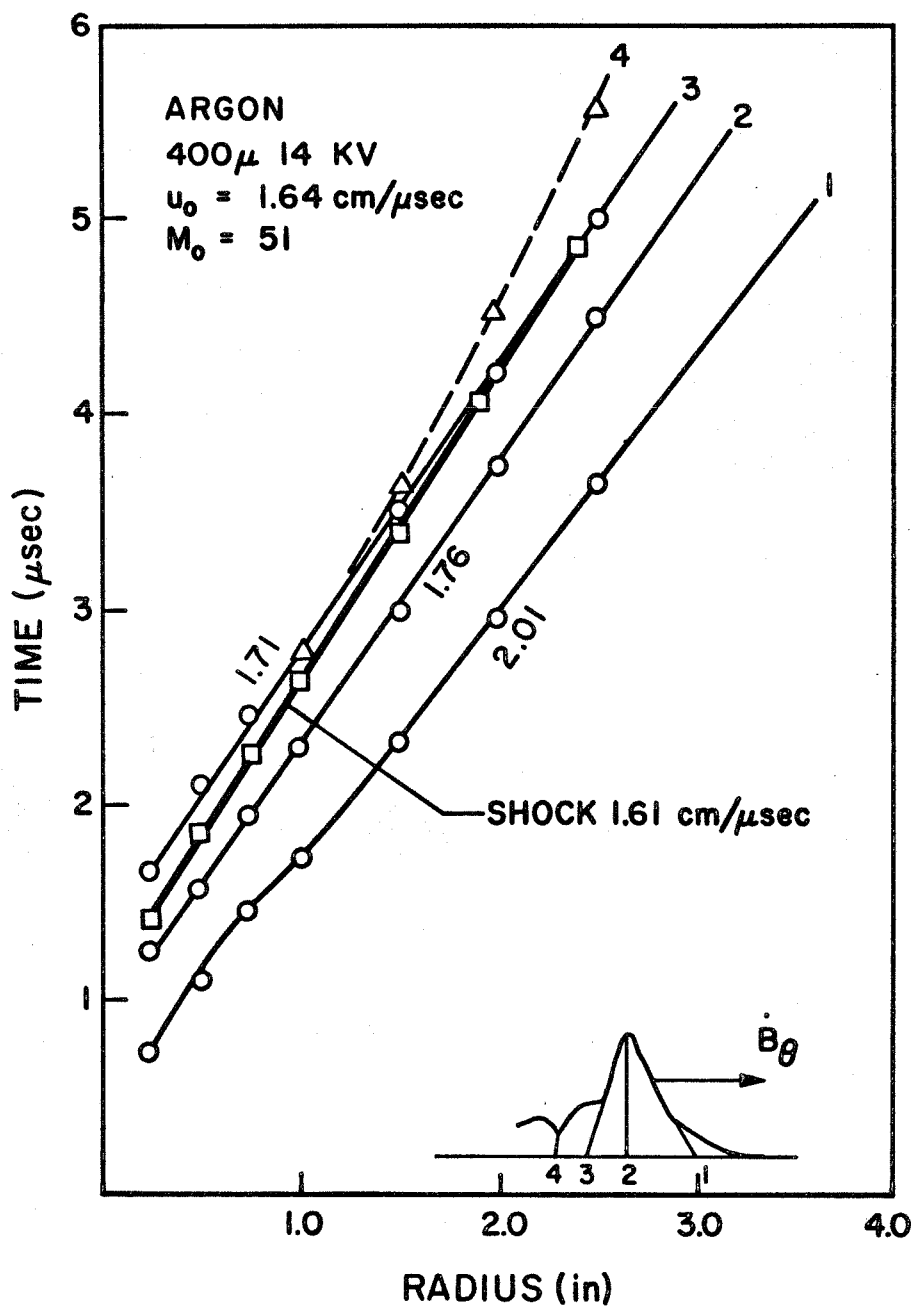


Figure 22. Shock and current sheet trajectories for argon. 400 μ Hg 14 KV.

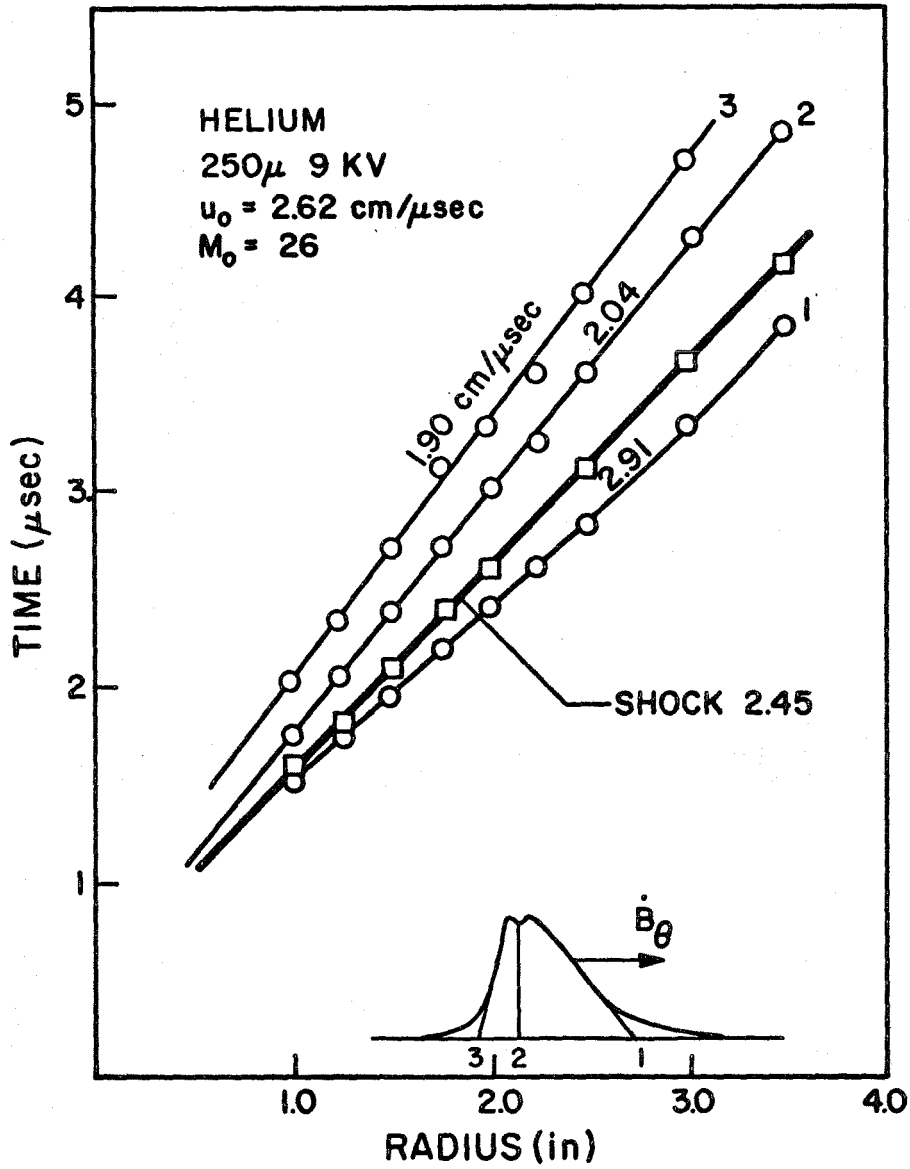


Figure 23. Shock and current sheet trajectories for helium.

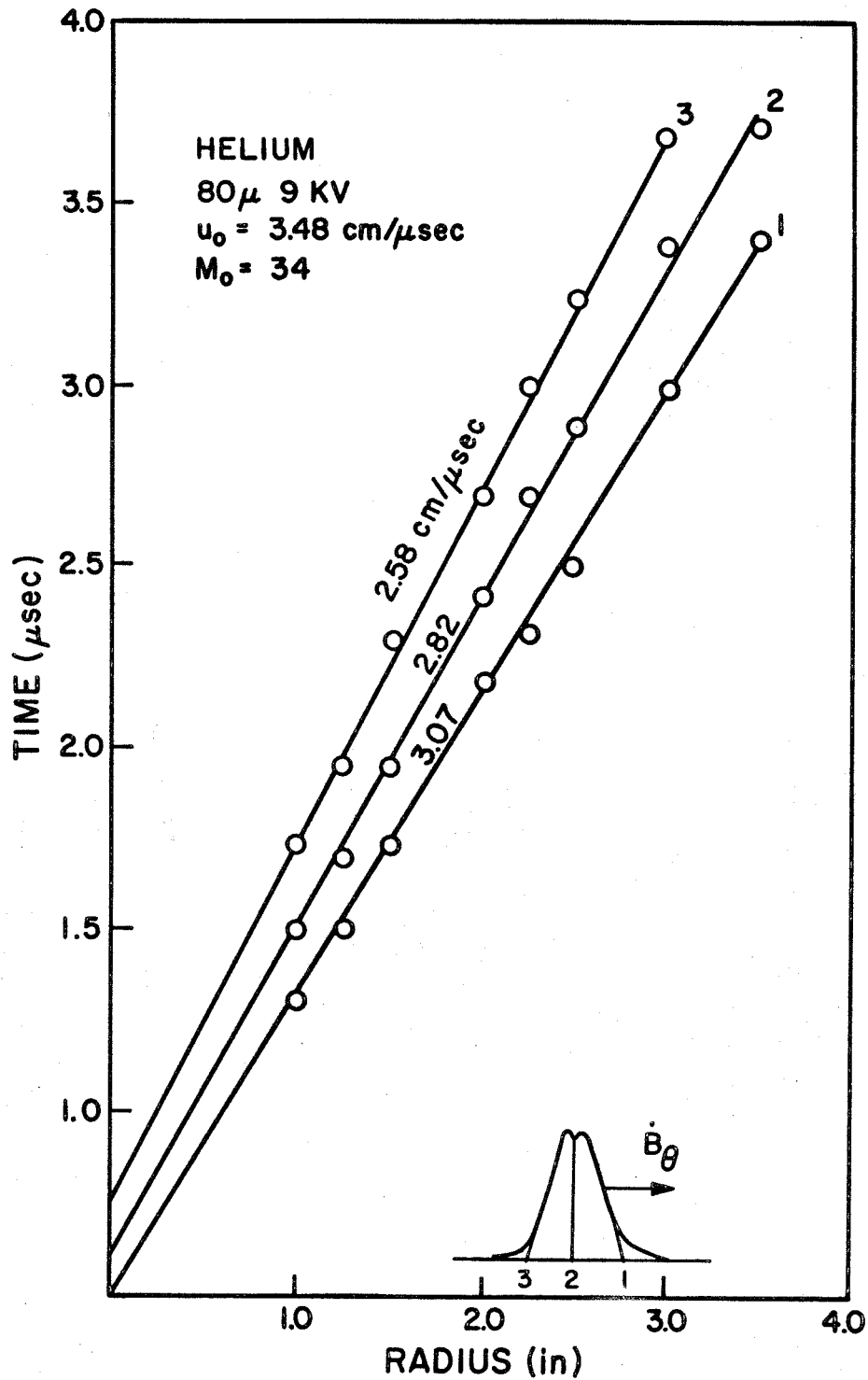
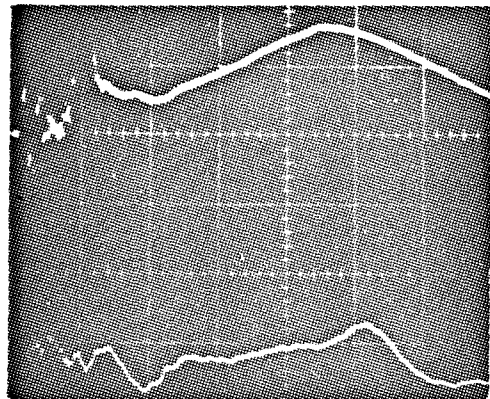
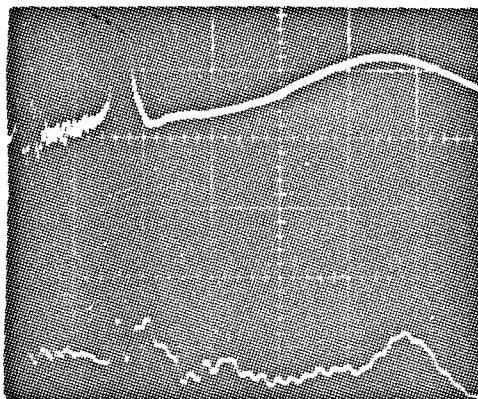


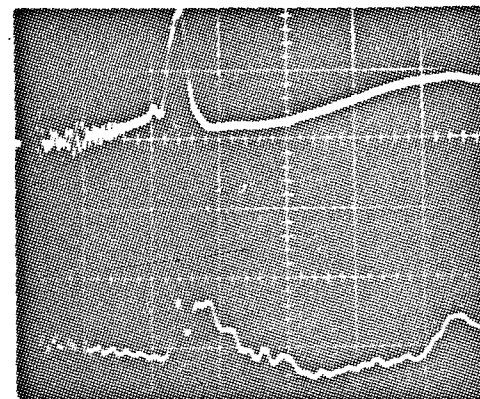
Figure 24. Current sheet trajectories for low density helium.



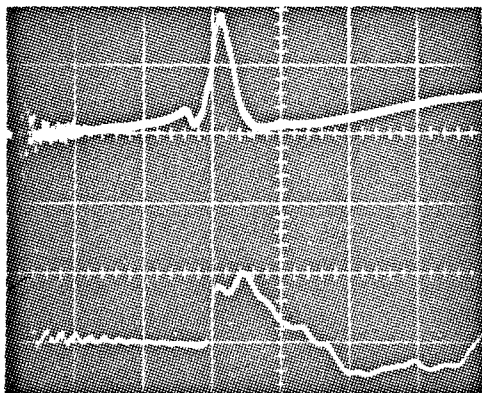
$r = \frac{1}{2}''$



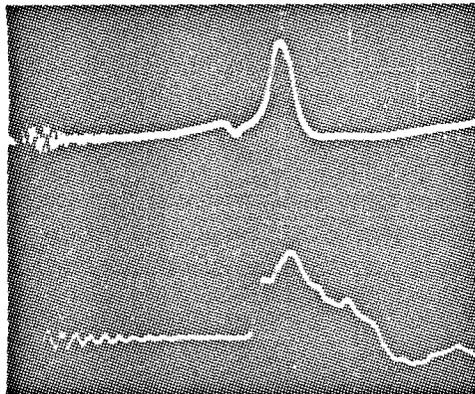
$r = 1''$



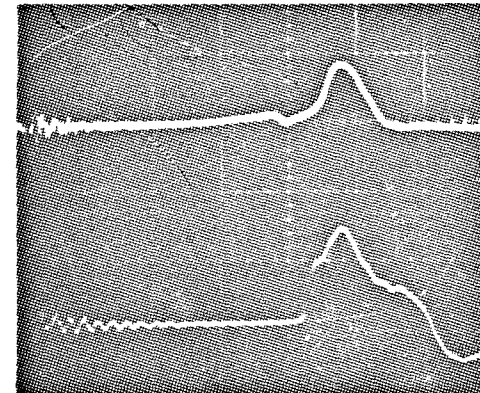
$r = 1\frac{1}{2}''$



$r = 2''$



$r = 2\frac{1}{2}''$



$r = 3''$

Figure 25. Actual oscilloscope traces for hydrogen at 700μ and 6 KV. Time scale, $1 \mu\text{sec}/\text{div}$. Upper trace B_{θ} , $1 \text{ v}/\text{div}$. Lower trace pressure, $.2 \text{ v}/\text{cm}$.

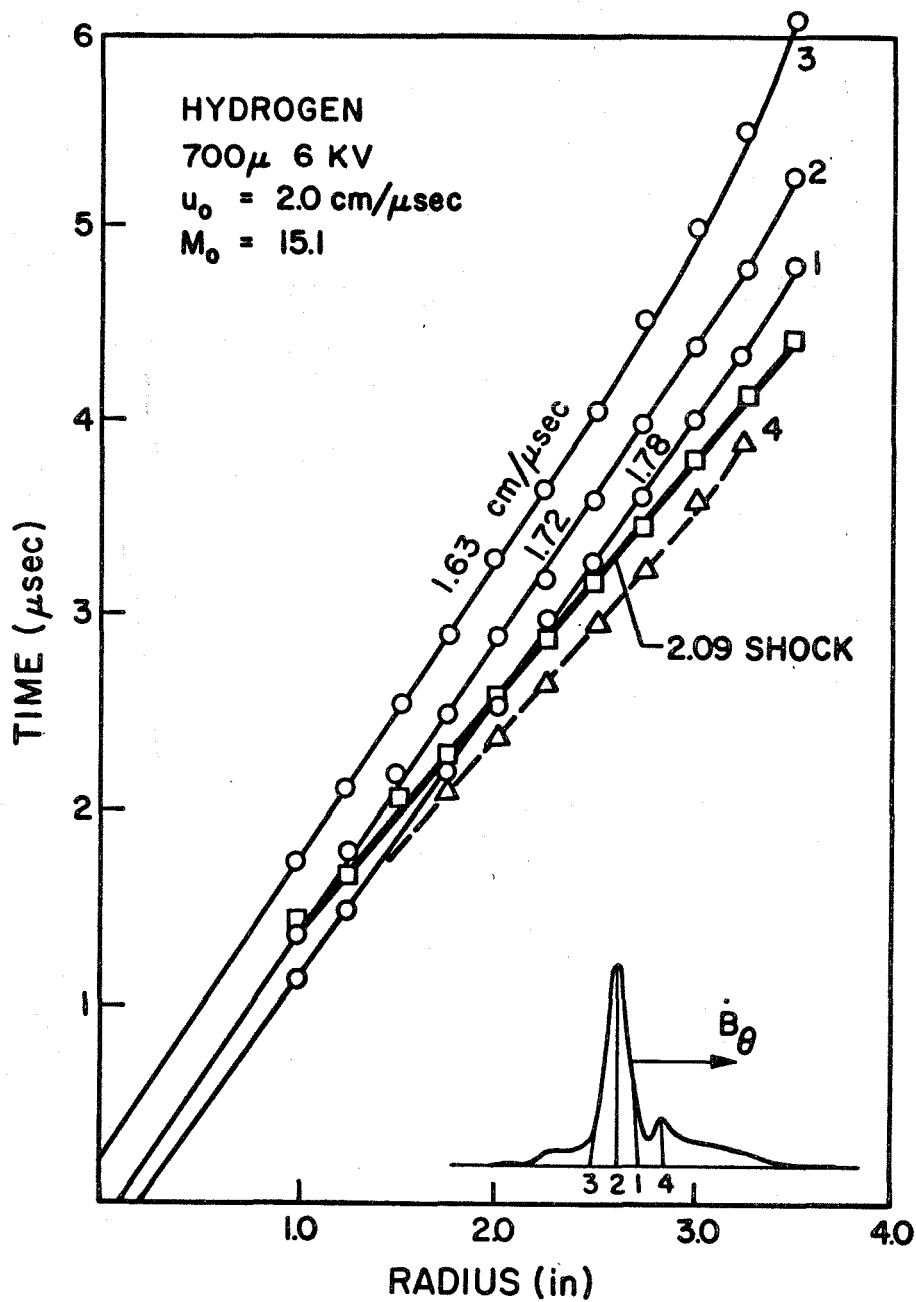


Figure 26. Shock and current sheet trajectories for hydrogen. 700μ Hg 6 KV.

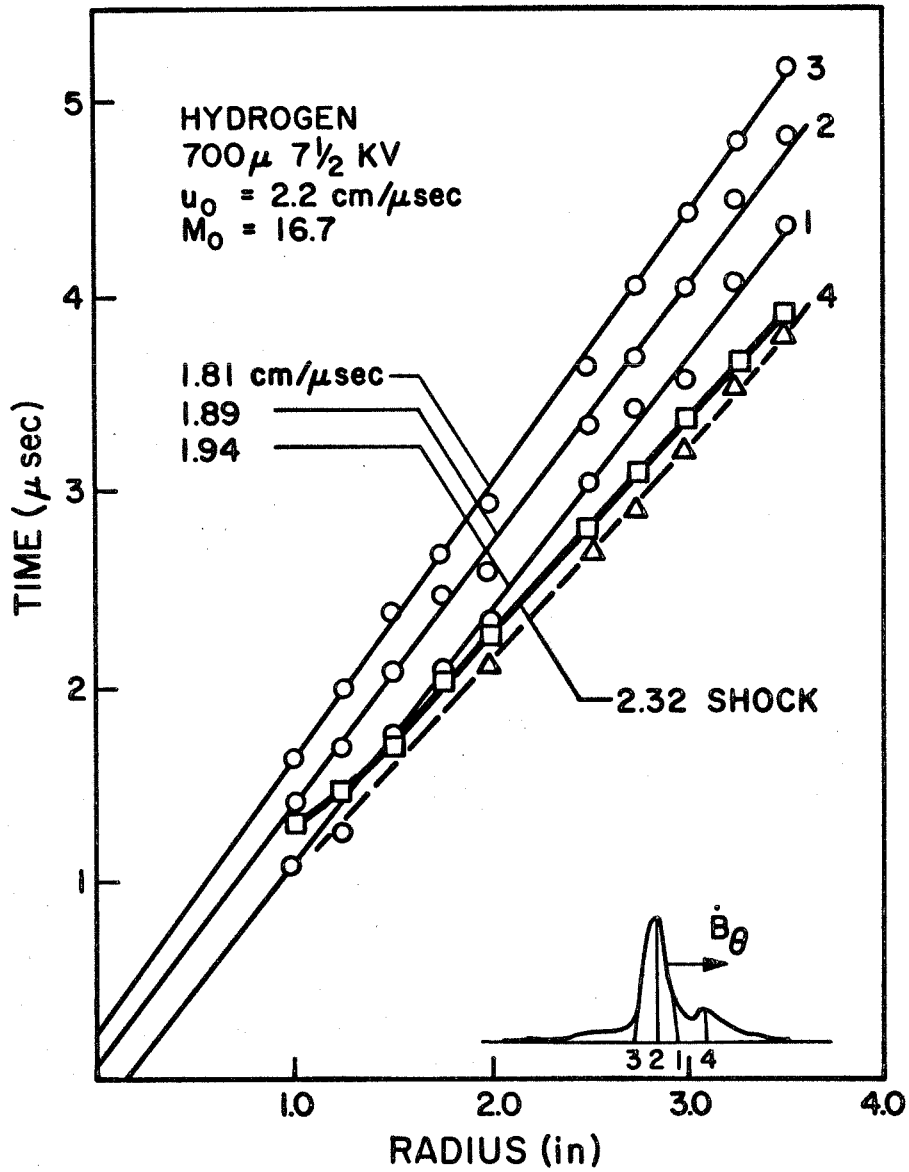


Figure 27. Shock and current sheet trajectories for hydrogen. 700μ Hg $7\frac{1}{2}$ KV.

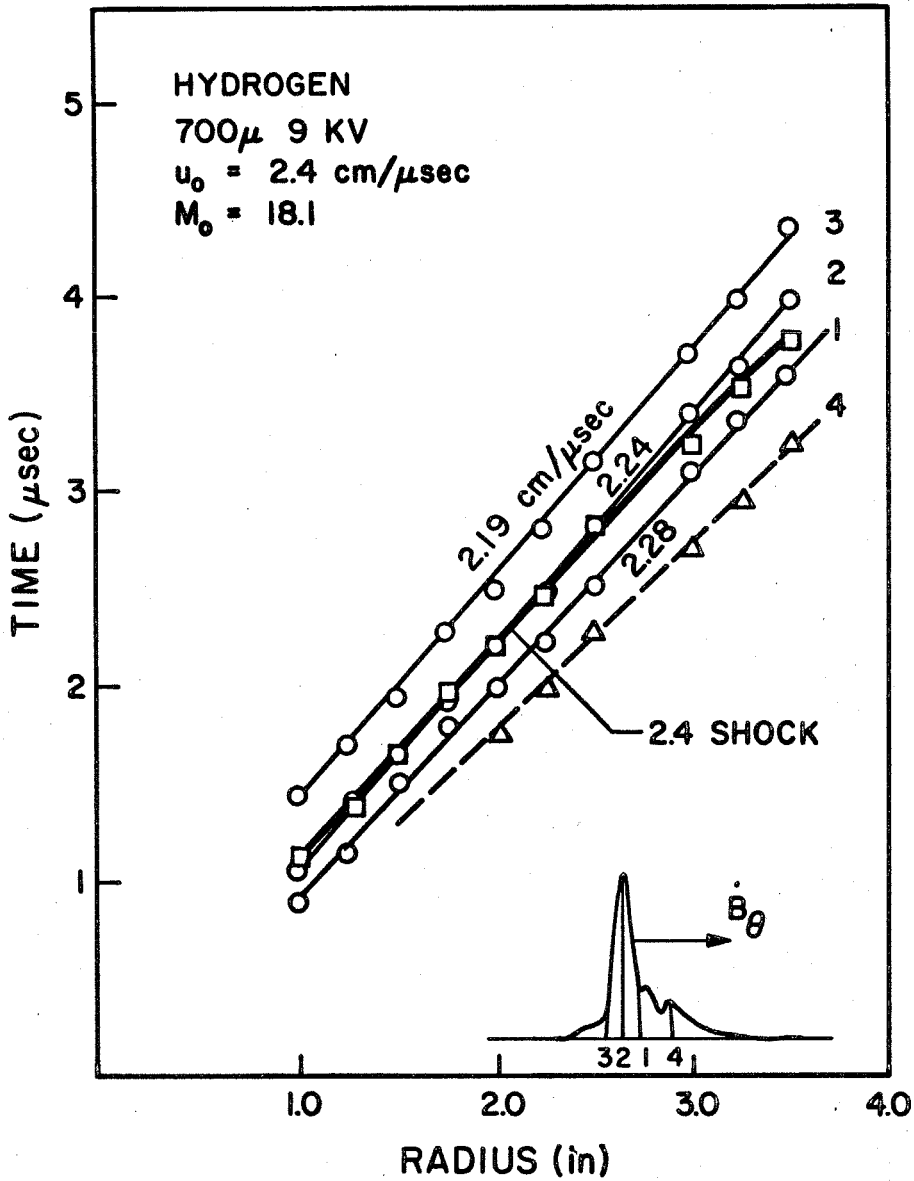


Figure 28. Shock and current sheet trajectories for hydrogen. 700 μ Hg 9 KV.

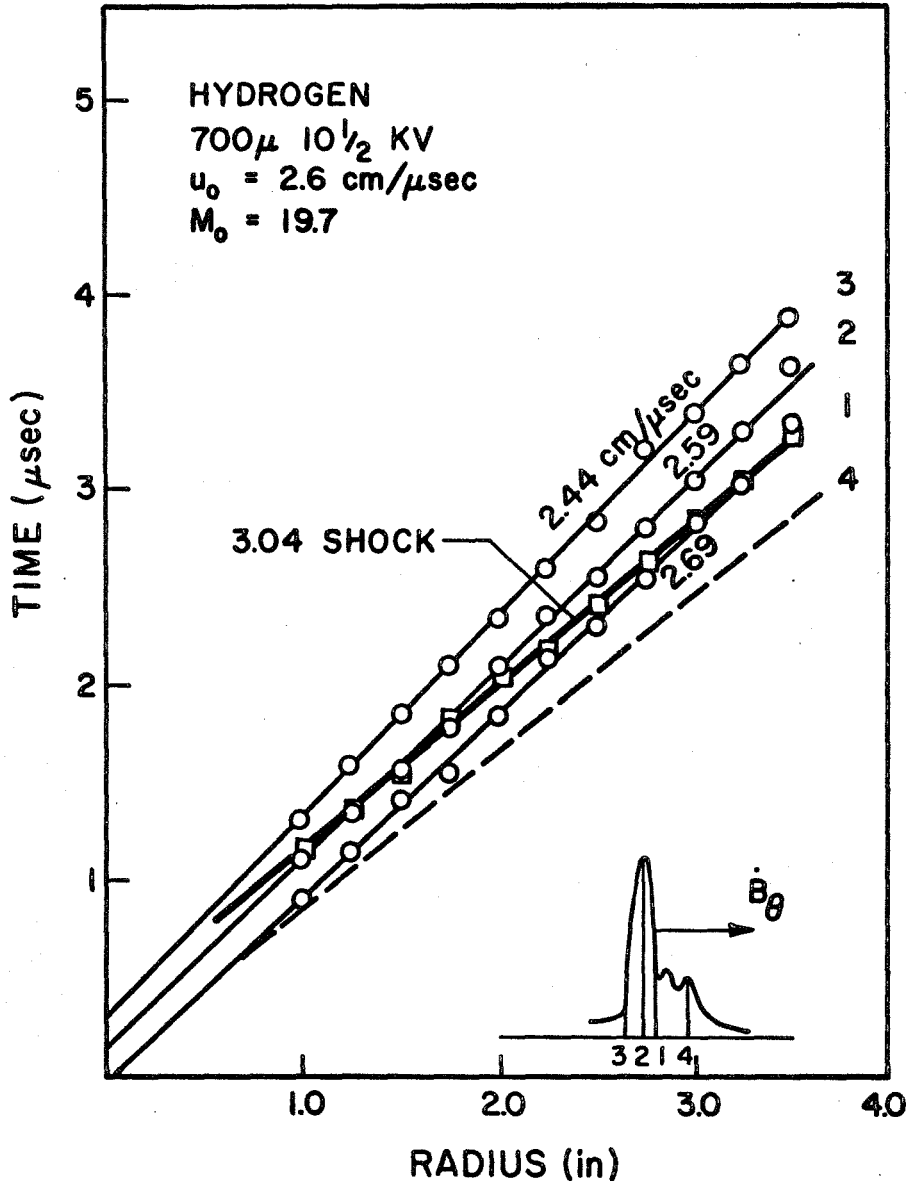


Figure 29. Shock and current sheet trajectories for hydrogen. 700μ Hg $10\frac{1}{2}$ KV.

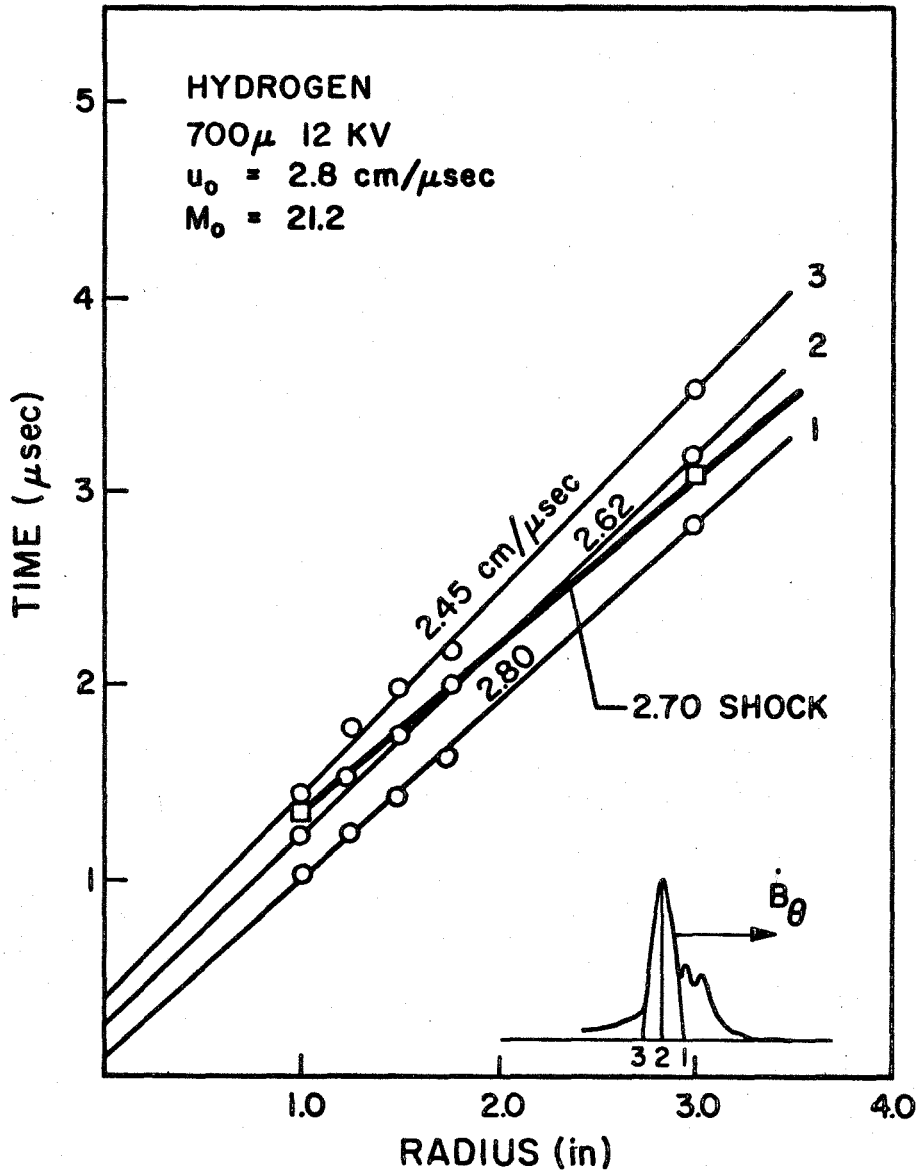


Figure 30. Shock and current sheet trajectories for hydrogen. 700 μ Hg 12 KV.

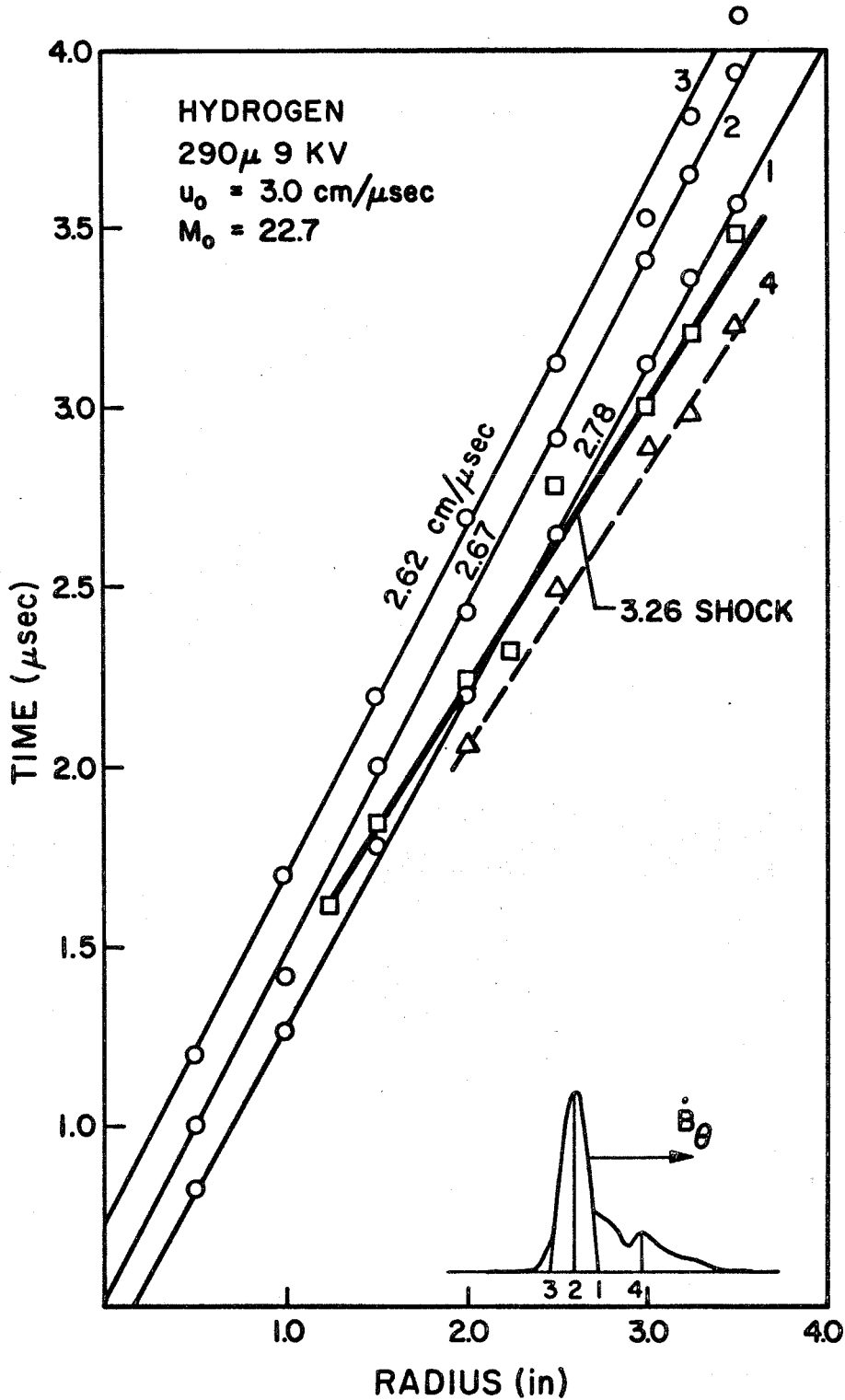


Figure 31. Shock and current sheet trajectories for hydrogen. 290μ Hg 9 KV.

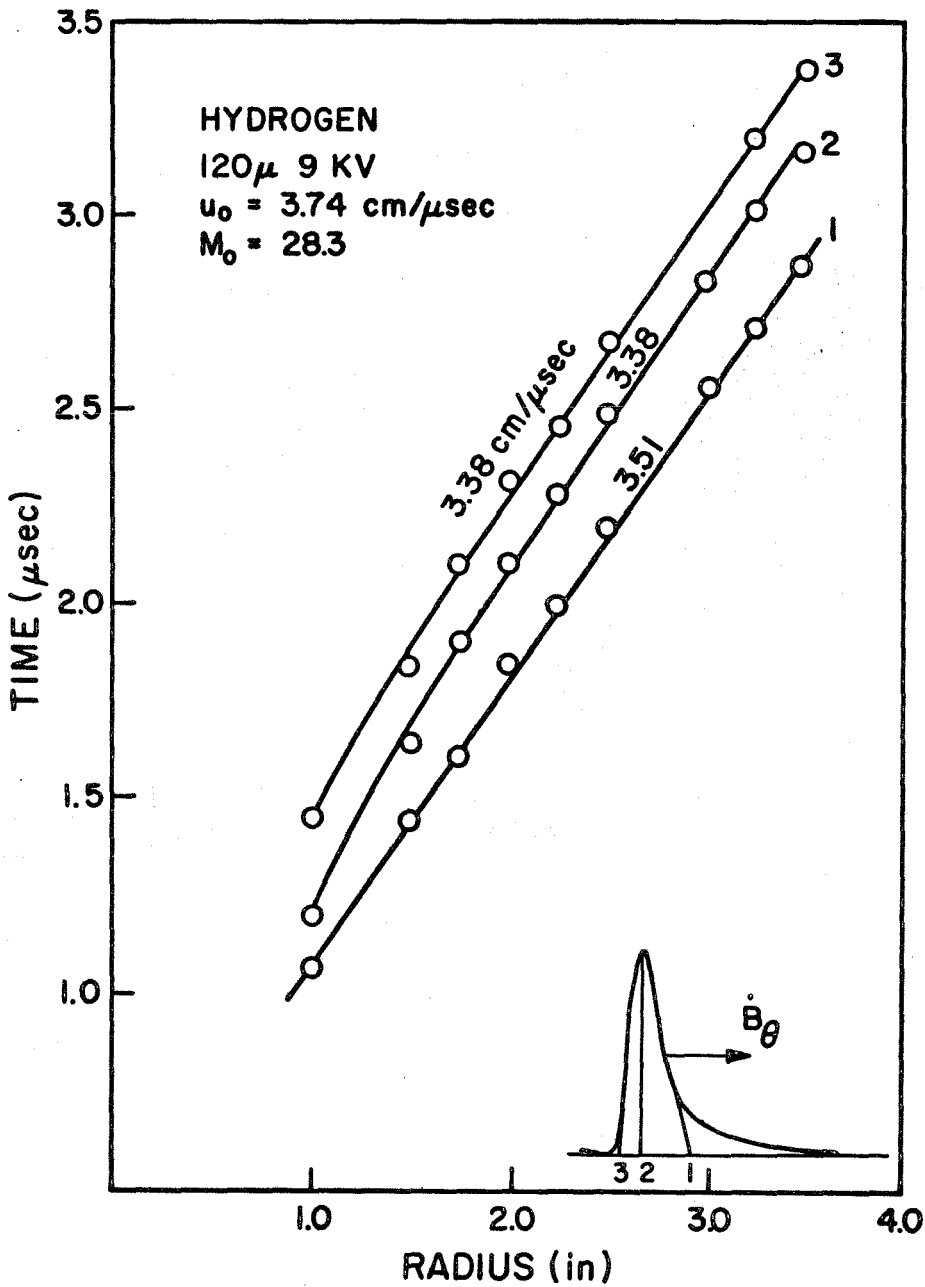


Figure 32. Current sheet trajectories for low density hydrogen.

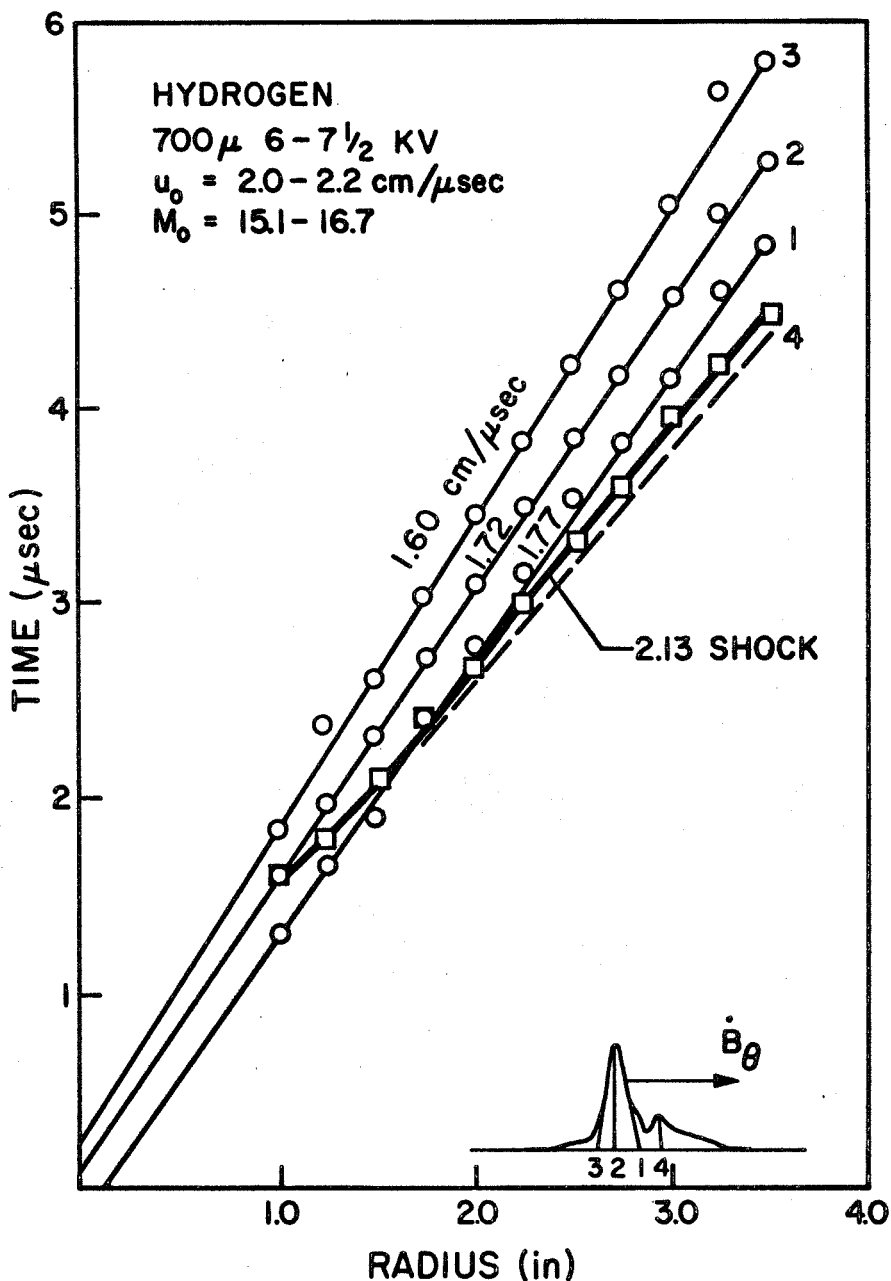


Figure 33. Shock and current sheet trajectories in hydrogen with the main capacitor bank charged to 7½ KV and fired 1.4 μ sec. after the preionization bank which is charged to 6 KV.

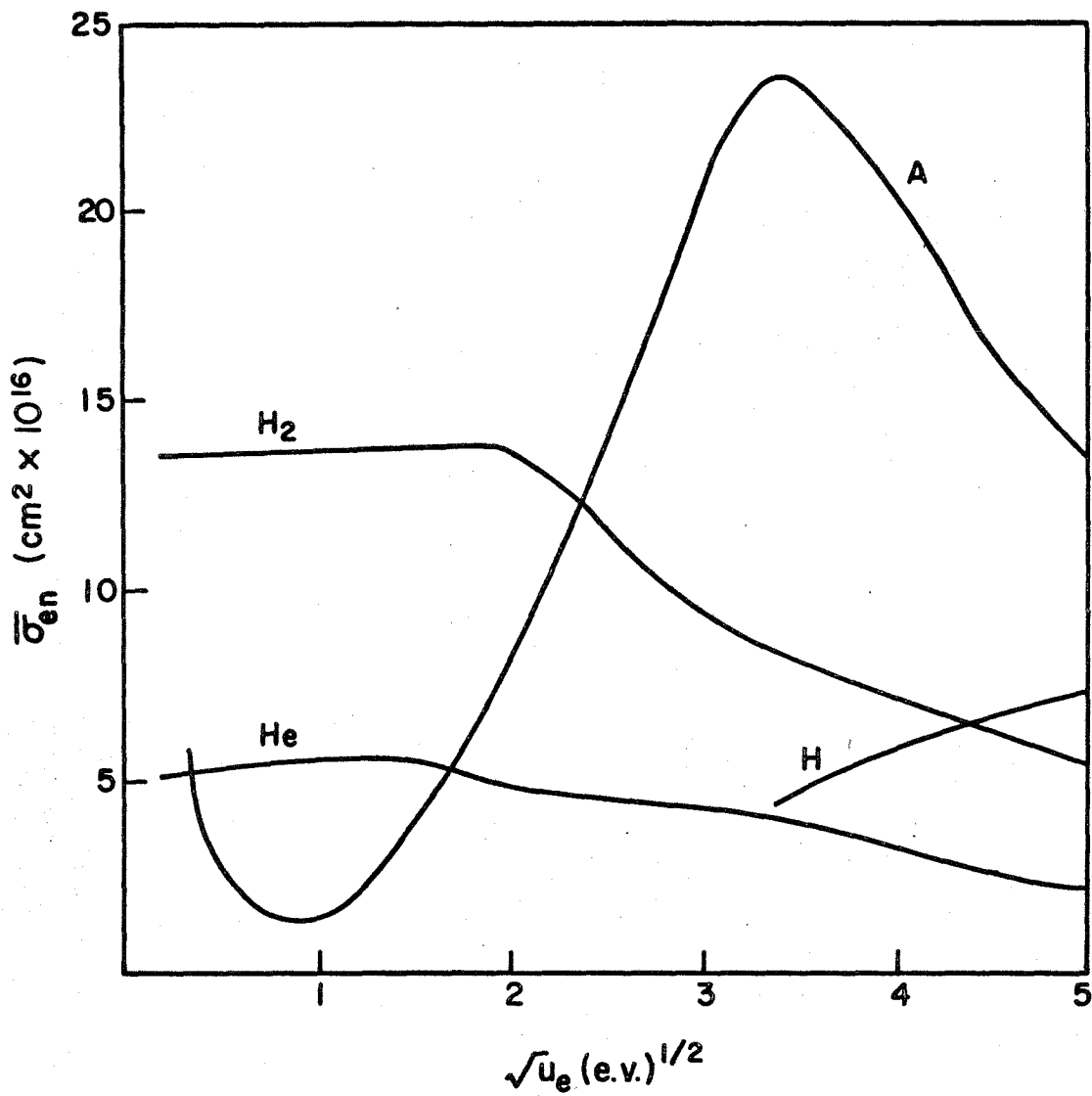


Figure 34. Electron neutral collision cross-sections as a function of electron energy.